# Condensate Retention and Shedding Effects on Air-Side Heat Exchanger Performance

C. M. Korte and A. M. Jacobi

ACRC TR-132

September 1997

*For additional information:*

Air Conditioning and Refrigeration Center
University of Illinois
Mechanical & Industrial Engineering Dept.
1206 West Green Street
Urbana, IL 61801

(217) 333-3115

*Prepared as part of ACRC Project 68*
*Water Retention and Shedding Effects*
*on Air-Side Heat Transfer Behavior*
*A. M. Jacobi, Principal Investigator*

*The Air Conditioning and Refrigeration Center was founded in 1988 with a grant from the estate of Richard W. Kritzer, the founder of Peerless of America Inc. A State of Illinois Technology Challenge Grant helped build the laboratory facilities. The ACRC receives continuing support from the Richard W. Kritzer Endowment and the National Science Foundation. The following organizations have also become sponsors of the Center.*

Amana Refrigeration, Inc.
Brazeway, Inc.
Carrier Corporation
Caterpillar, Inc.
Copeland Corporation
Dayton Thermal Products
Delphi Harrison Thermal Systems
Eaton Corporation
Ford Motor Company
Frigidaire Company
General Electric Company
Hydro Aluminum Adrian, Inc.
Indiana Tube Corporation
Lennox International, Inc.
Modine Manufacturing Co.
Peerless of America, Inc.
Redwood Microsystems, Inc.
The Trane Company
Whirlpool Corporation
York International, Inc.

*For additional information:*

*Air Conditioning & Refrigeration Center*
*Mechanical & Industrial Engineering Dept.*
*University of Illinois*
*1206 West Green Street*
*Urbana IL 61801*

*217 333 3115*

# Abstract

The effects of condensation on the air-side performance of plate-fin-tube heat exchangers have been experimentally investigated by conducting experiments under dry conditions and then repeating these experiments under condensing conditions. Sensible air-side heat transfer coefficients and friction factors are reported and compared for these cases. Real-time and steady-state measurements of condensate retention are reported for both coated and uncoated heat exchangers with fin spacings of 4, 8, 10 and 12 fpi (fins per inch). An initial model has been developed to predict the quantity of condensate retained on plate-fin-tube heat exchangers with wide fin spacings as a function of the heat exchanger geometry, advancing and receding contact angles, and air-side Reynolds number. This model demonstrates condensate retention modeling techniques and possible improvements to these techniques are discussed. Experiments were conducted in an optically accessible test section and photographs of retained condensate are provided. These photographs identify the modes of condensation and condensate geometries observed during the experiments. Advancing and receding contact angle were measured using a contact angle goniometer for typical heat transfer surfaces. These measurements indicated a significant increase in surface wettability during the first 100 hours of wet-dry cycling.

# Table of Contents

Section Page

# List of Tables

Table Page

# List of Figures

Figure Page

# Nomenclature

| | |
|---|---|
| $a$ | parameter defined by Equation C.17 |
| $a_i$ | parameter defined by Equation C.20 |
| $A$ | area ($m^2$) |
| $A_{c,f}$ | fin cross sectional area ($m^2$) |
| $A_{covered}$ | heat transfer surface area covered by droplets ($cm^2$) |
| $b$ | parameter defined by Equation C.19 |
| $b_i$ | parameter defined by Equation C.20 |
| $b_s$ | slope of the saturation curve, parameter defined by Equation C.17 |
| $B_1$ | coefficient defined by Equation 4.18 |
| $B_2$ | coefficient defined by Equation 4.19 |
| $C$ | ratio used to determine $T_s$ (Equation B.38) |
| $C_1$ | parameter defined by Equation C.13 |
| $C_2$ | parameter defined by Equation C.13 |
| $C_{avg}$ | parameter defined by Equation C.14 |
| $C_d$ | drag coefficient |
| $Cp$ | specific heat at constant pressure (kJ/kg-K) |
| $dwpt$ | dewpoint (°C) |
| $dl$ | differential length of contact line (m) See Figure 4.2 |
| $D$ | diameter (m) |
| $D_{AB}$ | binary mass diffusion coefficient ($m^2/s$) |
| $D_{coll}$ | collar outside diameter (m) |
| $\Delta N$ | number of droplets of diameter $D \pm 0.2D$ per $cm^2$ |
| $\Delta P_{HX}$ | heat exchanger differential pressure (kPa) |
| $E_1$ | tube distance from fin edge (m) See Figures 2.4 and 2.5 |
| $E_2$ | tube distance from fin edge (m) See Figures 2.4 and 2.5 |
| $f$ | friction factor |
| $f_s$ | fin spacing (m) See Figures 2.4 and 2.5 |
| $F$ | cross flow correction factor |
| $F_d$ | air drag force (N) |
| $F_g$ | gravitational force (N) |
| $F_s$ | surface tension force (N) |
| $g$ | gravitational acceleration ($9.81\ m/s^2$) |
| $G$ | mass velocity based on minimum free flow area ($kg/m^2$-s) |

| | |
|---|---|
| $h$ | air-side heat transfer coefficient (W/m$^2$-K) |
| $h_i$ | coolant-side heat transfer coefficient (W/m$^2$-K) |
| $h_D$ | mass transfer coefficient (kg/m$^2$-s) |
| $h_d$ | height of droplet (m) |
| $H$ | height of plane fin (m) |
| $H'$ | parameter defined by Equation C.8 |
| $H_f$ | height of fin (m) See Figures 2.4 and 2.5 |
| $HX$ | heat exchanger |
| $i$ | enthalpy (kJ/kg) |
| $i_{fg}$ | latent heat of vaporization (kJ/kg) |
| $i_s$ | saturated air enthalpy at coil surface temperature (kJ/kg) |
| $j$ | sensible j factor (Equation 3.1) |
| $k$ | thermal conductivity (W/m-K) |
| $k_w$ | thermal conductivity of water film (W/m-K) |
| $l$ | width of condensate bridge (m) See Figure 4.5 |
| $L$ | dimension used in Equation C.9 (See Figure C.1) |
| $L_{max}$ | max. length of fin-tube bridge neglecting air-flow forces (m) See Figure 4.5 |
| $L_f$ | length of fin (m) See Figures 2.4 and 2.5 |
| $L_t$ | length of tubing (m) |
| $Le$ | Lewis number |
| $\dot{m}$ | mass flow rate (kg/s) |
| $m$ | parameter defined by Equation C.6 |
| $m_{cond}$ | mass of retained condensate (g) |
| $M$ | dimension used in Equation C.9 (See Figure C.1) |
| $N_s$ | number of sectors (Equation C.11) |
| $N_{steps}$ | number of steps in discretization |
| $N_t$ | number of tubes |
| $Nu$ | Nusselt number |
| $P$ | pressure (kPa) |
| $P_f$ | perimeter of the fin (m) |
| $Pr$ | Prandtl number |
| $q$ | heat transfer rate (W) |
| $r_i$ | inner radius of circular fin (m) |
| $r_o$ | outer radius of circular fin (m) |
| $R$ | particular gas constant (kJ/kg-K) |

| | |
|---|---|
| $R_a$ | air-side thermal resistance (K/W) |
| $R_f$ | fin thermal resistance (K/W) |
| $R_i$ | internal thermal resistance (K/W) |
| $R_m$ | total metal thermal resistance (K/W) |
| $R_t$ | tube wall thermal resistance (K/W) |
| $Re$ | Reynolds number |
| $Re_b$ | Reynolds number based on bubble diameter |
| $S_t$ | transverse tube spacing (m) See Figures 2.4 and 2.5 |
| $S_l$ | longitudinal tube spacing (m) See Figures 2.4 and 2.5 |
| $Sc$ | Schmidt number |
| $St$ | Stanton number |
| $T$ | temperature (°C) |
| $T_r$ | fin surface temperature at radius r (°C) |
| $T_s$ | coil surface temperature (°C) |
| $u$ | local velocity (m/s) |
| $U$ | overall heat transfer coefficient ($W/m^2$-K) |
| $V$ | velocity (m/s) |
| $\rlap{-}V$ | volume ($m^3$) |
| $W$ | humidity ratio ($kg_{water}/kg_{dry\ air}$) |
| $W_d$ | heat exchanger finned width (m) See Figures 2.4 and 2.5 |
| $W_{s,r}$ | humidity ratio of saturated air at $T_r$ ($kg_{water}/kg_{dry\ air}$) |
| $y_f$ | half fin thickness (m) |
| $y_w$ | average water film thickness (m) |

*Greek Symbols*

| | |
|---|---|
| $\alpha$ | angle of inclination (radians) See Figure 4.2 |
| $\beta$ | parameter defined by Equation C.9 |
| $\chi$ | ratio of mass flow rate of air through HX to total mass flow rate of air |
| $\delta$ | fin thickness (m) |
| $\Phi$ | angular coordinate direction (radians) See Figure 4.2 |
| $\phi$ | fin efficiency |
| $\gamma$ | surface tension (mN/m) |
| $\eta$ | surface effectiveness |
| $\mu$ | dynamic viscosity (N-s/$m^2$) |
| $\theta$ | contact angle (radians) See Figure 3.21 |
| $\theta_A$ | advancing contact angle (radians) See Figure 3.22 |

| | |
|---|---|
| $\theta_M$ | mean contact angle (radians) $\theta_M = (\theta_A + \theta_R)/2$ |
| $\theta_R$ | receding contact angle (radians) See Figure 3.22 |
| $\rho$ | density (kg/m$^3$) |
| $\sigma$ | contraction ratio ($A_{min}/A_{fr}$) |
| $\nu$ | kinematic viscosity (m$^2$/s) |
| $\xi$ | parameter defined by Equation C.19 |
| $\Psi$ | parameter defined by Equation C.9 |
| $\zeta^*$ | location of adiabat at first tube row (Equation B.22) |

*Subscripts*

| | |
|---|---|
| *a* | air |
| *b* | base of fin |
| *c* | coolant |
| *calc* | calculated |
| *coll* | collar |
| *da* | dry air |
| *eff* | effective |
| *equiv* | equivalent |
| *f* | fin |
| *fr* | frontal |
| *i* | inside |
| *l* | liquid |
| *lat* | latent |
| *lm* | log mean |
| *ma* | moist air |
| *meas* | measured |
| *min* | minimum |
| *max* | maximum |
| *mp* | midpoint |
| *o* | outside |
| *p* | prime |
| *pr* | projected |
| *s* | saturation state for given temperature |
| *sens* | sensible |
| *t* | tube |

| | |
|---|---|
| *tot* | total |
| *w* | surface of water film |
| *x* | coordinate direction (See Figures 4.2 and 4.5) |
| *1* | HX inlet |
| *2* | HX outlet |

# Chapter 1 - Introduction and Literature Review

## 1.1 Introduction

When the heat transfer surfaces of a heat exchanger operate below the dewpoint of the incoming air, condensation occurs on these surfaces. This condensation will occur in either a dropwise or filmwise fashion depending on the wettability of the surfaces. Once condensate forms, it accumulates on the coil until it is removed by gravitational and air-flow forces. Water retained on the heat exchanger and droplets carried by the freestream air play an important role in the overall performance of heat exchangers in air-conditioning and refrigeration applications. In refrigeration, water retention characteristics are important during defrost when water must be drained from the evaporator. In air-conditioning systems, condensate on the evaporator may adversely affect heat transfer or occupant comfort by collecting and fouling the surface or blowing off the evaporator with conditioned air. Water retained on the heat exchanger increases the pressure drop across the heat exchanger by restricting the flow of air. A topic of recent attention has been the emission of unpleasant odors with conditioned air. Retained condensate provides a medium for biological activity which might cause these odors. Unfortunately, there are no general models for predicting the quantity of retained condensate, and the effects of retained condensate on heat exchanger performance are not clearly understood.

The focus of this project was to develop and validate a model that would allow an engineer to predict the quantity of retained condensate (water mass) on a heat exchanger surface as a function of the geometry, contact angle, orientation, and air-side Reynolds number and to investigate the effects of retained condensate on heat exchanger performance. A wind tunnel was constructed for testing heat exchangers under condensing conditions which allowed for both real-time and steady-state measurements of condensate retention. Experiments were conducted to provide data for validating a retention model. In addition, heat transfer and pressure drop data were recorded for heat exchangers operating under wet and dry conditions. An initial model for predicting the quantity of retained condensate has been developed for heat exchangers with wide fin spacings, and further improvements to this model have been outlined. Analytical techniques for modeling retained condensate have been developed and retained condensate geometries have been identified.

## 1.2 Literature Review

### 1.2.1 Background

Combined latent and sensible heat transfer in air-conditioning and refrigeration applications has attracted the interest of many researchers. The effects of condensation on

sensible heat exchanger performance and heat exchanger pressure drop are not clearly understood. While it is accepted that retained condensate results in an increase in heat exchanger air-side pressure drop, the extent of this increase appears to depend on the heat exchanger geometry and heat exchanger surface condition as well at the air-flow rate. Condensation has been shown to have a significant effect on sensible heat exchanger performance; however, the direction and magnitude of this effect also appears to be dependent upon the particular heat exchanger geometry and operating condition. The effect of condensation on sensible heat exchanger performance has been complicated by differences in the data reduction techniques applied to wet heat exchangers, with potentially important differences in the definition of the fin efficiency for wet fins. Typical wet fin efficiency analyses assume condensation occurring over the entire fin surface; however, few authors give evidence that they are operating under conditions for which this will occur. Although many researchers have noted the effects of condensate retention on heat exchanger performance, few studies have focused on surface wettability effects or made observations regarding the quantity and nature of retained condensate.

### 1.2.2 Wet Heat Exchanger Performance

#### A. Initial Experimental Studies

Bettanini [1] conducted experiments on simultaneous heat and mass transfer to a vertical surface. Bettanini observed an increase in sensible heat transfer under wet conditions for both filmwise and dropwise condensation with a greater increase for dropwise condensation. This enhancement was then simulated by placing solid gypsum drops on the surface. A direct relationship was observed between surface roughness and an increase in sensible heat transfer. The surface wall temperature was varied and higher mass transfer rates resulted in larger enhancements in sensible performance. Bettanini concluded that the observed enhancements were attributable to the combined effects of surface roughness and mass transfer on sensible heat transfer.

An enhancement in combined heat transfer (sensible plus latent) and an increase in pressure drop was reported by Guillory and McQuiston [2] for a parallel-plate heat exchanger operating under condensing conditions. These effects were attributed to an increase in surface roughness associated with the roughening of the heat exchanger walls by condensate deposition. These studies were extended and a second test loop was constructed to observe water retention behavior [3]. The friction factor was shown to be approximately 25% higher under condensing conditions. In addition, the presence of water droplets in a developing flow field was claimed to be responsible for an enhancement in heat and mass transfer coefficients.

Visual studies revealed dropwise condensation on aluminum, copper-nickel, and copper surfaces. The airstream did not appear to effect droplets through shear for Reynolds numbers between 600 and 4000 based on hydraulic diameter. The air flow was downward through the heat exchanger suggesting that vapor-shear and pressure-drop forces were small compared to gravitational and surface tension forces acting on retained condensate. At low Reynolds numbers, McQuiston claimed that there was a significant time required for steady-state droplet formation. Tree and Helmer [4] conducted studies with a very simple two parallel plate heat exchanger. An increase in pressure drop and sensible heat transfer was measured under wet conditions in the transitional and fully turbulent flow regimes.

## B. Plate-Fin-Tube Heat Exchangers

McQuiston extended earlier research to full scale heat exchanger geometries by presenting data [5] and developing correlations [6] for plate-fin-tube heat exchangers with staggered tube configurations operating under condensing conditions. Identical four-row heat exchangers were studied with the only variation being the fin spacing. Fin spacings of 4, 8, 10, 12, and 14 fins per inch (fpi) were tested. Three different surface conditions were tested for each heat exchanger: dry, wet surface with filmwise condensation, and wet surface with dropwise condensation. Dropwise condensation was obtained by cleaning the heat exchangers with perchloroethylene and filmwise condensation by boiling in household dishwashing detergent and water. The mode of condensation was reported to be stable throughout the experiments. McQuiston claimed that the surface type and surface condition have an effect on the transport processes. McQuiston also stated that the nature (dropwise or filmwise) and quantity of retained condensate has an important effect on performance. Measured total and latent heat transfer rates were typically higher for dropwise than filmwise condensation.

McQuiston observed an enhanced sensible performance for wide fin spacings (4 and 8 fpi). For fin spacings less than 8 fpi, a decrease in sensible heat transfer performance was observed under condensing conditions. A simulated 12 fpi heat exchanger showed an interaction between the airstream and dropwise condensate for Reynolds numbers above 500 based on heat exchanger hydraulic diameter. An increase in pressure drop was measured under both wet surface conditions (dropwise and filmwise). For wider fin spacings, dropwise condensation increased heat exchanger pressure drop while the effects of filmwise condensation were minor. For fin spacings less than 10 fpi, the effects of filmwise and dropwise condensation on pressure drop were approximately equal. The effect of condensate on the friction factor was more pronounced at low Reynolds numbers. Although not mentioned, this may be caused by a change in the quantity of retained condensate as Reynolds number increases. As Reynolds number increases, it is possible that more condensate is being removed by the air-flow and gravitation forces leading to a lower steady-state value of retained condensate. Contrary to previous results reported by Guillory [2], heat and mass transfer processes were reported to be unaffected by the rate of condensation.

Eckels and Rabas [7] studied plate-fin-tube heat exchangers with fin spacings from approximately 8 fpi to approximately 13 fpi. An enhanced sensible heat transfer was observed under wet conditions. An increase in heat exchanger pressure drop was observed under wet conditions; however, this effect diminished at high Reynolds numbers similar to the trend observed by McQuiston [5]. An analogy between the transverse velocity of the condensing phase during dehumidification and the transverse velocity at the wall when exercising boundary layer control by fluid extraction through a permeable wall was used to explain this enhancement. Eckels and Rabas found that this analogy could account for all of the sensible heat and mass transfer augmentation and most of the differential pressure increase. Kandlikar [8] challenged these conclusions. Eckels and Rabas based their analogy on work by Hartnett and Eckert [9]. Hartnett and Eckert determined the transverse velocity at the wall based on the mass transfer rate and the density of the freestream air. Eckels and Rabas calculated the transverse velocity at the wall based on the density of water vapor at the partial pressure of water vapor corresponding to the wall temperature. Kandlikar showed that for typical operating conditions the augmentation predicted by Eckels and Rabas could be as much as 110 times higher than the actual value based on the work of Hartnett and Eckert. Kandlikar showed that this enhancement would be less than 0.5% for a typical operating condition.

Recent studies on the performance of plate-fin-tube heat exchangers under dehumidifying conditions have been reported by Wang *et al.* [10]. These studies investigated the effects of fin spacing, the number of tube rows, and air inlet conditions. Friction factors under wet conditions were reported to be 60% to 120% higher than for dry conditions and insensitive to the inlet relative humidity. A degradation in sensible heat transfer performance for wet conditions was reported for low Reynolds numbers based on tube diameter. Sensible heat transfer performance increased or remained the same for wet conditions at high Reynolds numbers with the increase diminishing as the number of tube rows increased. The change between sensible degradation and enhancement under wet conditions was observed at a Reynolds number of approximately 2000 based on tube diameter. The sensible heat transfer performance was shown to be independent of the inlet air relative humidity. Wet heat exchanger correlations were developed and compared to the reduced data presented by McQuiston [5]. The correlations presented by Wang did not agree with McQuiston's reduced data. The discrepancies were shown to be due to differences in the calculation of the wet fin efficiency. Wang rereduced McQuiston's raw data applying consistent wet fin efficiency evaluations. This analysis resulted in good agreement between the correlations presented and McQuiston's raw data.

### C. Heat Exchangers with Enhanced Fin Geometries

Several other heat exchanger fin geometries have been studied and the effects of condensation on heat exchanger performance for these geometries is also unclear. Wavy-fin heat exchangers were investigated by Mirth and Ramadhyani [11] and design correlations for wet heat exchanger performance were developed [12]. They found the effects of condensation on sensible heat transfer performance to be inconclusive. Comparing the wet sensible heat transfer coefficients to the dry sensible heat transfer coefficients, the wet values were sometimes higher and sometimes lower than the corresponding dry values with no clear trends. They reported that the sensible heat transfer coefficient decreased with an increase in inlet air dewpoint.

Wang *et al.* studied louver-fin-tube heat exchangers under wet conditions and considered the effects of an anti-corrosion surface treatment [13]. Contrary to the results for plate-fin-tube heat exchangers, sensible heat transfer performance was reported to decrease as the inlet air relative humidity increased. Also, the friction factor was reported to decrease as the inlet air relative humidity increased. Sensible heat transfer, combined heat and mass transfer, and friction factor were all shown to be dependent on the fin spacing. Both sensible and combined transfer coefficients decreased as the fin spacing decreased. The friction factor increased as the fin spacing decreased. The effect of fin spacing on heat transfer and pressure drop performance decreased as the Reynolds number exceeded that for which condensate began to be blown off the heat exchanger. This condition began at an air-side Reynolds number between 1000 and 3000 based on the collar diameter. The surface treatment was observed to have no effect on heat exchanger performance.

The effects of hydrophilic surface coatings for wavy, lanced, and louver-fin heat exchangers were recently reported by Hong [14]. A lower sensible heat transfer coefficient was observed under condensing conditions for 12 fpi wavy and lanced-fin heat exchangers as well as for a 17 fpi louver fin heat exchanger. Both hydrophilic and uncoated heat exchangers were tested. The hydrophilic coating appeared to have no discernible effect on heat transfer performance; however, this coating significantly decreased the wet to dry pressure drop ratio. A 45% reduction was obtained for the louver-fin heat exchanger and a 15% reduction for the wavy-fin heat exchanger at a frontal air velocity of 2.5 m/s. These results are promising; however, contact angle testing of these coatings showed an initial contact angle of less than 10° which then increased to a constant value of about 60° during the first 1000 wet-dry cycles. This contact angle was comparable to the contact angle obtained for an uncoated sample after 1000 wet-dry cycles.

### D. Finned-Tube Heat Exchangers

The effects of condensation on finned-tube heat exchangers have also been reported and these results also appear inconclusive. For example, Bryan [15] reported an enhanced sensible performance under condensing conditions for a bare-tube heat exchanger; however, Bryan reported a decrease in sensible performance for a six row integral-fin-tube heat exchanger operating under condensing conditions [16]. Bryan hypothesized that the decrease in sensible performance was brought about by condensate retained on the heat exchanger surfaces decreasing the surface effectiveness below the calculated value. Jacobi and Goldschmidt [17] reported a decreased sensible heat transfer performance for baffled, finned-tube heat exchangers under wet conditions operating at low Reynolds numbers. This degradation diminished with increasing Reynolds number showing a cross-over for a Reynolds number of approximately 1200 based on hydraulic diameter. The work of Jacobi and Goldschmidt was supported by Uv and Sonju [18] who reported a degradation in heat transfer performance at low Reynolds numbers for finned-tube heat exchangers with small fin spacings (approximately 5 fpi).

### 1.2.3 Condensate Retention Modeling

Several models of condensate retention have been proposed; however, it does not seem possible to generalize these very specific results. Rudy and Webb [19] developed a method for measuring retained condensate on integral low-finned tubes and reported that retention was intensified for close fin spacings. A gravity-drained model proposed by Beatty and Katz [20] was suggested to be inadequate by Rudy and Webb because it failed to consider surface tension effects. Webb and co-workers [21] [22] developed models taking into account surface tension effects. These models were for negligible vapor shear, and there is little hope of generalizing their results. Jacobi and Goldschmidt [17] presented a simple model of condensate retained as "bridges" formed between adjacent fins. This model was qualitatively successful in explaining the cross-over in sensible heat transfer coefficient they observed. Although there have been few attempts to model retained condensate, research in the areas of dropwise condensation and surface and colloid science may provide useful results for retention modeling. These topics are discussed Chapter 4.

### 1.2.4 Conclusion

Although there have been numerous studies on the effects of condensation on heat exchanger performance, there are several questions which have yet to be answered. The effects of condensation on sensible heat transfer and pressure drop appear to be closely related to the particular geometry and surface characteristics of the heat exchanger. Many researchers have identified the interaction of retained condensate with the air flow as a probable mechanism for sensible heat transfer enhancement. These enhancement mechanisms were supported by the work of Hu *et al.* [23]. Hu simulated retained condensate with nearly spherical elements of polystyrene. Using a naphthalene sublimation technique, an enhancement of up to 30% in the spatially averaged heat transfer coefficient was observed. Small horseshoe vortices associated with the simulated droplets significantly influenced local sublimation rates. This mechanism appears to dominate any enhancement that would be associated with the transverse velocity of the condensing vapor. Retained condensate has also been associated with a degradation in sensible heat transfer performance. This degradation is typically observed for heat exchangers with narrow fin spacings or at low air-side Reynolds numbers and may be an effect of condensate accumulating and acting as an additional resistance to heat transfer. Discrepancies exist regarding the effects of inlet relative humidity on heat transfer and pressure drop performance. The heat transfer discrepancies may be due to different techniques which have been applied to determine wet fin efficiencies. Heat exchanger pressure drop has been shown to decrease when heat exchanger surfaces are coated with hydrophilic surface coatings; however, the longevity of these coatings is often poor. A hydrophilic surface may also be realized by increasing the surface roughness of the heat exchanger surfaces [24]. It might be possible to explain the effects of water retention on air-side heat exchanger performance by the nature and quantity of retained condensate. There have been few studies which discuss the nature of condensate retention and there appear to have been no attempts to measure the quantity of retained condensate for plate-fin-tube heat exchangers.

## 1.3 Project Objectives

The objectives of this study were to develop a condensate retention model, to measure the quantity of condensate retained on heat exchangers for validation of this retention model, and to investigate the performance of heat exchangers operating under condensing conditions. These objectives were fulfilled as follows:

Retention Modeling: There are no general models which allow an engineer to predict the quantity of condensate retained on a heat exchanger as a function of heat exchanger geometry, heat exchanger orientation, contact angles, and air-side Reynolds number. This study provides analytical techniques and initial efforts to develop such a model. These techniques are used to understand retention characteristics observed during experiments.

In attempting to model and predict condensate retention, one must identify the size, shape, and distribution of retained condensate geometries. The experiments reported in this thesis were conducted in a test section which was optically accessible and photographs of retained condensate were taken to provide this type of information.

Condensate Retention Measurements: Although the quantity of retained condensate may have a significant influence on heat exchanger performance, retention measurements have not been reported in previous studies. This study includes both real-time and steady-state measurements of retained condensate for various heat exchangers operating under condensing conditions. These measurements provide unique insights into the dynamics of water retention as well as data for the validation of modeling efforts. The effects of air-flow rate, fin spacing, and surface condition have been considered.

Wet Heat Exchanger Performance: The air-side heat transfer performance of heat exchangers operating under condensing conditions has been a topic of much interest, but the effects of condensate on sensible heat transfer are not well understood. These effects appear to be related to the particular heat exchanger geometry and operating condition and may be influenced by the nature and quantity of condensate retained on the heat transfer surfaces. Air-side heat transfer data have been recorded during condensate retention experiments. Various techniques for determining the air-side heat transfer coefficient have been considered and are presented. The effects of condensate on the air-side sensible heat transfer coefficient were considered by conducting experiments under conditions for which the entire heat exchanger was dry and then repeating these experiments under condensing conditions.

In determining overall air-side heat exchanger performance, air-side pressure drop must be considered. Heat exchanger pressure drop affects air-flow pumping power and can be an important element in overall system performance. Increases in air-side pressure drop are often associated with enhanced fin surfaces and may be magnified by water retention. Water retained on the heat exchanger acts to restrict air flow and increase pressure drop. Air-side pressure drop data have been recorded for both wet and dry heat exchanger surfaces to determine the increase in pressure drop attributable to retained condensate.

# Chapter 2 - Experimental Apparatus and Methods

A wind tunnel was designed and constructed for studying wet heat exchanger performance and measuring condensate retention. This wind tunnel included a unique test section providing real-time measurements of condensate retention. The experimental apparatus and instrumentation are described in this chapter. The experimental methods are also presented.

## 2.1 Experimental Apparatus

The experimental apparatus consisted of a closed-loop wind tunnel, a unique test section, and a coolant loop circulating a single-phase coolant. Other equipment included a contact angle goniometer and an electronic balance for measuring the quantity of retained condensate.

### 2.1.1. Wind Tunnel

The wind tunnel designed and constructed for this study is shown in Figure 2.1. Air was circulated in this closed-loop wind tunnel and conditioned to provide a controlled dewpoint, temperature, and flow rate at the test section inlet. Steam was injected at a controlled rate to maintain the desired inlet air dewpoint. Air was sampled at the test section inlet and the dewpoint of the sampled air was measured using a chilled mirror hygrometer. The chilled mirror hygrometer provided a control signal for closed-loop dewpoint control. This control signal was supplied to a PID controller which regulated the power input to a humidifier capable of providing 0.19 kg/min (25.5 lbs/hr) of steam. Inlet air temperature was regulated manually by varying the power supplied by five strip heaters capable of adding 2.5 kW to the air flow. A baffle was installed just upstream of the heaters to prevent air from flowing backwards through the wind tunnel at low air flow rates due to natural convection. The airstream was heated and humidified upstream of the blower allowing the blower to mix the flow. The axial blower was capable of providing air flow rates up to 300 cfm. Flow straighteners were installed in the contraction at the blower outlet. Air entering the test section was drawn from a plenum chamber through honeycomb flow straighteners, screens, and a rectangular contraction with an area contraction ratio of 9:1.

### 2.1.2. Coolant Loop

A single-phase ethylene glycol and water mixture with inhibitors (DOWTHERM 4000) was diluted with distilled water and circulated on the tube side of the heat exchanger. The temperature was controlled by a chiller and the mixture circulated by two pumps capable of providing tube-side flow rates up to approximately 0.15 kg/s. The ethylene glycol mixture provided the advantage of being able to frost and then defrost a coil in order to investigate the difference between loading a heat exchanger by defrosting rather than condensing on the heat transfer surfaces.

### 2.1.3. Test Section

The wind tunnel test section is shown in Figure 2.2. This test section was designed to allow real-time measurements of retained condensate and easy specimen removal for measuring the steady-state value of retained condensate. The test section consisted of an inner frame mounted to the outer walls of the test section using high precision linear bearings. The inner frame supported the heat exchanger, and this assembly was suspended using a cable and pulley system. The weight of the inner frame, the heat exchanger, and drag forces associated with air flow were balanced by counterweights outside the test section. Condensate accumulating on the heat exchanger was measured using a calibrated load cell. The side walls of the test section were removable and windows allowed access for removing the heat exchanger and inserting a tray below the heat exchanger to catch any water which fell from the heat exchanger during the removal process.

The inner frame consisted of rectangular contraction and diffusing sections with area contraction ratios of 4:1 which reduced the test section flow area to the frontal area of the heat exchanger. The contraction was designed to provide a uniform velocity profile at the heat exchanger inlet while avoiding flow separation. The contraction was designed using techniques developed by Morel [25] for axisymmetric wind tunnel contractions.

The test section was made of clear acrylic to allow optical access. The entire test section was insulated to limit conduction losses. Pressure taps were located in the side walls of the test section at the heat exchanger inlet and outlet. These taps were used to measure air-side pressure drop across the heat exchanger. A second set of pressure taps were located across the inner frame for measuring the air-side pressure drop across the heat exchanger and the contraction and diffusing sections. This measurement was required to account for the additional drag force associated with condensate accumulating on the heat exchanger which was subtracted from the load cell measurement to determine the quantity of condensate which had accumulated on the heat exchanger.

### 2.1.4 Contact Angle Goniometer

Advancing and receding contact angles for typical heat exchanger fin surfaces were measured using a contact angle goniometer shown in Figure 2.3. The goniometer consisted of a telescope with a magnification ratio of 7:1 fitted with a vernier eyepiece with divisions of 0.2°. Crosshairs on the lens rotated with the eyepiece and were used to measure the contact angles. The droplet was illuminated by a diffuse light source. The viewing platform could be rotated in order to measure advancing and receding contact angles. In order to control the vapor pressure and prevent evaporation of the droplet, water was placed in a trough around the specimen holder and a cover was placed over the droplet.

## 2.2 Instrumentation

### 2.2.1. Air-Side Instrumentation

**A. Dewpoint Measurement**

The dewpoint of the air was measured at the test section inlet and outlet in order to determine mass transfer rates and provide a control signal for humidity control. Air was drawn by a diaphragm air pump through fluted tubes that were located in the inlet and outlet air-side measurement sections of the wind tunnel (Figure 2.4). The dewpoint of the sampled air was measured using chilled mirror hygrometers with a measurement uncertainty of ±0.2°C. The chilled mirrors were periodically cleaned with alcohol to remove insoluble contaminants which accumulated on the mirror surface. The dewpoint measured by the inlet and outlet chilled mirrors agreed to within the measurement uncertainty when no condensation was occurring on the heat exchanger.

**B. Temperature Measurements**

Type-T thermocouples with special limits of error were used to measure air temperatures. The thermocouples were located in the inlet and outlet air-side measurement sections of the wind tunnel (See Figure 2.1). Each thermocouple was individually referenced to a thermocouple located in an ice bath. A six-thermocouple grid was used to measure the average inlet air temperature and a twelve-thermocouple grid was used to measure the average outlet air temperature. The thermocouples were calibrated to a NIST traceable mercury-in-glass thermometer using an isothermal temperature controlled bath. The calibration data were fit with individual fifth order polynomials. These data were compared to NIST polynomials and the standard deviation from the NIST polynomials was typically less than 0.1°C.

**C. Air Mass Flow Rate**

An ASME standard orifice plate was used to measure the air mass flow rate (Figure 2.1). The orifice plate was installed following ASME standard MFC-3M-1989 [26]. Three different orifice plates were used to cover the air flow range. Honeycomb flow straighteners were located upstream of the orifice plate at the distance specified by the standard. The orifice plate differential pressure was measured using an electronic manometer with an uncertainty of ±0.0005" water.

### D. Heat Exchanger Face Velocity

The air velocity at the heat exchanger and mass flow rate through the heat exchanger could not be determined from the air mass flow rate directly. A clearance was required between the inner frame which supports the heat exchanger and the outer walls of the test section to provide frictionless suspension for real-time condensate retention measurements. A fraction of the air flow passed through this clearance rather than through the heat exchanger; therefore, face velocities were measured using a constant temperature thermal anemometer with a calibrated uncertainty of ±1%. The average velocity was determined by traversing the flow in three locations with one traverse along the centerline and the others approximately 1/4" from the side walls. Measurements were recorded at seven equally spaced locations for each traverse and the values were averaged. This average face velocity was then used to determine the mass flow rate based on the channel dimensions at the measurement location.

### E. Heat Exchanger and Suspension Differential Pressures

The pressure drop across the heat exchanger and the pressure drop across the inner suspension assembly were measured using an electronic manometer with an uncertainty of ±0.0005" water. The wall pressure tap locations are shown in Figure 2.2.

## 2.2.2. Coolant-Side Instrumentation

### A. Temperature Measurement

Coolant-side temperatures were measured using type-T immersion thermocouples. The thermocouples were installed so that the thermocouple junction would be located at approximately the center of the tube. These thermocouples were installed in insulated copper tubing approximately six feet upstream and downstream of the heat exchanger. The heat exchanger was connected to the copper tubing with flexible, reinforced, PVC tubing that was insulated with 3/8" of insulation to prevent conduction losses. The coolant-side thermocouples were calibrated following the same procedure as the air-side thermocouples. These thermocouples were also referenced individually to thermocouples located in an ice bath.

### B. Flow Rate

An oscillating piston type flow meter was used to measure the coolant flow rate. The manufacturer stated uncertainty of this meter was ±0.5%. A transmitter attached to the flow meter provided a 1-5 VDC pulse with a frequency proportional to the volumetric flow rate. The number of pulses were counted over a timed cycle with an uncertainty of ±1 pulse at the beginning and end of the counted interval using a Philips programmable timer/counter and the value was transferred to the data acquisition system over a GPIB interface.

### 2.2.3 Condensate Retention Measurements

Both real-time and steady-state measurements of retained condensate were recorded. The real-time mass of retained condensate was measured using a calibrated, cantilever beam, thin film load cell with a nominal output of 1 millivolt per volt excitation. The details of this measurement are discussed in Appendix A. The steady-state value of retained condensate was measured by removing the heat exchanger after prolonged exposure to condensing conditions. The heat exchanger was weighed using an electronic balance with a readability of 0.1 g and a reproducibility of 0.1 g.

### 2.2.4 Data Acquisition

All experimental measurements, except the differential pressure measurements, were logged using a computerized data acquisition system. The data acquisition system sampled 25 channels and averaged these values over 11 measurements. These average values were recorded at 45 second intervals.

## 2.3 Experimental Overview

### 2.3.1. Experimental Scope

This research focused on plate-fin-tube heat exchangers. This geometry was chosen in order to provide validation for retention modeling techniques. This geometry is relatively simple to characterize, and at wide fin spacings the retained condensate geometries could be identified. Modeling techniques developed for plate-fin-tube heat exchangers provide a starting point for modeling of retained condensate on more complex heat exchanger fin surfaces, e.g. louvered fins, wavy fins, vortex generators. Condensate retention measurements for this geometry also provide a benchmark to which condensate retention on enhanced surfaces can be compared. The heat exchanger dimensions are provided in Table 2.1 and the geometry is depicted in Figures 2.4 and 2.5. Similar heat exchangers were provided by the two manufacturers. The heat exchangers provided by Brazeway had "dogbones" or slits in the fins between the tubes and did not include fin collars. The heat exchangers provided by HeatCraft did not have slits in the fins between the tubes and the fins had collars which met the adjacent fin completely covering the copper tube. The air flow was downward through the heat exchanger which means that the gravitational and air-flow forces were aligned during the experiments. Aligning the air-flow and gravitational forces enabled the effects of air-flow forces on retained condensate to be more readily identified since the gravitational component is independent of the air flow.

Simultaneous heat transfer, pressure drop, and condensate retention measurements were recorded during the first set of experiments which included heat exchangers 1 and 2. The final steady-state value of retained condensate was also measured and compared to the real-time measurement. The focus of these experiments was to investigate the effects of retained condensate on heat exchanger performance, to study the dynamics of condensate retention, and to compare measurements of retained condensate using the two different techniques. During these experiments, air flow passed over the return bends which allowed the condensate on the outside surface of the outer fins to be photographed. Further experiments were conducted with different fin surface coatings. These experiments included heat exchangers 3 through 9. During these experiments, the flow was restricted to the finned area of the heat exchanger. The return bends were blocked off and insulated. The focus of these experiments was to determine the effects of surface coatings on the quantity of retained condensate. A corrosion resistant prepainted surface, Mt. Holly Gold, and a hydrophilic corrosion resistant surface, Hycor, were included in the experimental studies. A summary of the experimental studies is presented in Table 2.2.

### 2.3.2 Experimental Conditions

The steady-state experimental conditions are shown in Tables 2.3 and 2.4. Dry experiments were conducted by setting the inlet coolant temperature so that the temperature at the tube wall was above the dewpoint of the air throughout the heat exchanger. Dry conditions were verified by observing that no condensation was visible on the heat exchanger surfaces and by comparing the inlet and outlet dewpoints. There was some variation in the coolant temperature for the dry runs because the inlet coolant temperature was adjusted according to the dewpoint of the air which depended on the lab conditions. The experimental conditions for the wet runs were determined so that the entire heat exchanger would be wet and wet-dry partitioning would not complicate data reduction techniques. At the highest air flow rates the heat exchanger was beginning to dry out and in some cases dry regions could be identified on areas of the fin furthest from the tube at the heat exchanger inlet. These regions were small, however, compared to the total fin area and should not significantly effect the experimental results. Many previous investigators do not observe the fins to be wet or dry or do not clearly state the criteria applied to determine these conditions.

The inlet air temperature for the wet experimental runs was approximately 34°C with an inlet dewpoint of approximately 23.9°C. These conditions correspond to a inlet air relative humidity of 56%. The effects of inlet air humidity on air-side heat transfer and condensate retention were not investigated, and this is an area which would be recommended for future study. As discussed in the literature review, the effects of inlet air relative humidity on wet heat exchanger performance are not well understood.

### 2.3.3 Experimental Procedures

#### A. Dry Experiments

For the dry experiments inlet air temperatures were used to determine when the experimental conditions had reached steady state. Measurements were then recorded and averaged over a five minute interval. The average inlet air temperature typically varied by less than ±0.15°C while the data were recorded. While recording the data, the orifice and heat exchanger differential pressures were measured and recorded manually using an electronic manometer.

#### B. Wet Experiments

Wet experiments were conducted following procedures similar to those for the dry experiments. Steady state was determined by the inlet air temperature and inlet air dewpoint. In addition, sufficient time was allowed for the retained condensate to reach a steady value. If real-time retention measurements were being made, this condition could be identified by observing the load cell voltage. For experiments where real-time measurements of retained condensate were not recorded, the heat exchanger was exposed to condensing conditions for at least one hour before starting to record the data. The condensate retention was observed to reach steady state in less than 20 minutes by real-time measurements.

At the end of each wet run, the heat exchanger was removed and weighed to determine the quantity of retained condensate. A tray was inserted through a window below the heat exchanger (See Figure 2.2) to catch any condensate which was shaken from the heat exchanger during removal. This tray was inserted beneath the heat exchanger and the air flow was shut off simultaneously. The coolant-side flow was shut off and the heat exchanger was disconnected from the coolant-side lines using quick-connect couplings. The side of the test section was then removed exposing the heat exchanger. The heat exchanger was taken out of the test section and placed on the tray. The wet heat exchanger and tray were weighed on the electric balance. The heat exchanger was then allowed to dry and placed back on the tray. By subtracting the weight of the dry heat exchanger and tray from the initial measurement, the quantity of retained condensate was determined. The trapped volume of the coolant is also weighed but this is a constant for the two measurements because the heat exchanger leads are sealed by the quick-connect couplings.

### C. Real-Time Condensate Retention

In addition to steady-state heat transfer, pressure drop, and condensate retention measurements, real-time measurements of retained condensate were recorded. When performing this measurement, the inlet air temperature, air-flow rate, and dewpoint were set at the desired experimental conditions. The coolant was set to the desired temperature and circulated through a separate loop. The load cell was zeroed by adding and removing counterweight to the cable and pulley assembly. The load cell was then calibrated holding the air-flow rate constant. The data acquisition program was started and valves were adjusted to redirect the coolant flow through the heat exchanger. The average load cell voltage as well as all other experimental conditions were recorded at 45-second intervals. The differential pressure across the heat exchanger and inner frame assembly was measured manually using an electronic manometer. This measurement was made at approximately 45-second intervals in order to determine the increase in drag force due to the retained condensate. This force was then subtracted to determine the quantity of retained condensate. The details of this measurement technique are presented in Appendix A. The PID controller adjusted the steam flow rate to compensate for the condensate removal. The heaters were adjusted manually to compensate for the heat removal rate. A short time was required for the PID controller to respond to this step input and reach steady state. The inlet air dewpoint dropped as much as 8°C but this value typically recovered to the setpoint within five minutes and exhibited little or no overshoot. Inlet air temperatures were controlled to within ±1°C of the average value throughout the experiment.

Table 2.1 Heat exchanger information

| HX | 1 | 2 | 3 | 4 | 5 | 6 | 7 | 8 | 9 |
|---|---|---|---|---|---|---|---|---|---|
| **Manufacturer*** | A | A | B | B | B | B | B | B | B |
| **Rows** | 14 | 14 | 14 | 14 | 14 | 14 | 14 | 14 | 14 |
| $W_d$ **(m)** | 0.264 | 0.264 | 0.249 | 0.249 | 0.249 | 0.249 | 0.249 | 0.249 | 0.249 |
| $H_f$ **(m)** | 0.0508 | 0.0508 | 0.0508 | 0.0508 | 0.0508 | 0.0508 | 0.0508 | 0.0508 | 0.0508 |
| $L_f$ **(m)** | 0.269 | 0.269 | 0.267 | 0.267 | 0.267 | 0.267 | 0.267 | 0.267 | 0.267 |
| $E_1$ **(mm)** | 7.15 | 7.15 | 6.35 | 6.35 | 6.35 | 6.35 | 6.35 | 6.35 | 6.35 |
| $E_2$ **(mm)** | 18.25 | 18.25 | 19.05 | 19.05 | 19.05 | 19.05 | 19.05 | 19.05 | 19.05 |
| $f_s$ **(mm)** | 6.35 | 3.175 | 2.962 | 2.362 | 1.924 | 2.962 | 2.291 | 2.428 | 1.979 |
| $S_t$ **(mm)** | 25.4 | 25.4 | 25.4 | 25.4 | 25.4 | 25.4 | 25.4 | 25.4 | 25.4 |
| $S_l$ **(mm)** | 19.25 | 19.25 | 19.05 | 19.05 | 19.05 | 19.05 | 19.05 | 19.05 | 19.05 |
| $\delta$ **(mm)** | 0.168 | 0.168 | 0.152 | 0.152 | 0.152 | 0.152 | 0.152 | 0.114 | 0.114 |
| $D_{o,t}$ **(mm)** | 7.9375 | 7.9375 | 9.525 | 9.525 | 9.525 | 9.525 | 9.525 | 9.525 | 9.525 |
| $D_{i,t}$ **(mm)** | 6.668 | 6.668 | 8.865 | 8.865 | 8.865 | 8.865 | 8.865 | 8.865 | 8.865 |
| **Fin Material** | Al | Al | Al | Al | Al | Al | Al | Al | Al |
| **Tube Material** | Al | Al | Cu | Cu | Cu | Cu | Cu | Cu | Cu |
| $k_f$ **(kW/m-K)** | 0.222 | 0.222 | 0.222 | 0.222 | 0.222 | 0.222 | 0.222 | 0.222 | 0.222 |
| $k_t$ **(kW/m-K)** | 0.222 | 0.222 | 0.339 | 0.339 | 0.339 | 0.339 | 0.339 | 0.339 | 0.339 |
| **Coating** | None | None | Mt. Holly | Mt. Holly | Mt. Holly | None | None | Hycor | Hycor |

* A = Brazeway, B = HeatCraft

Table 2.2 Experimental Study

| HX | Dry HT | Dry $\Delta P_{HX}$ | Wet HT | Wet $\Delta P_{HX}$ | Real-Time Retention | S.S. Retention |
|---|---|---|---|---|---|---|
| 1 | X | X | X | X | X | X |
| 2 | X | X | X | X | X | X |
| 3 | | | | X | | X |
| 4 | | | | X | | X |
| 5 | | X | | X | | X |
| 6 | | X | | X | | X |
| 7 | | X | | X | | X |
| 8 | | | | X | | X |
| 9 | | | | X | | X |

Table 2.3 Steady-state experimental conditions for dry runs

| **HX** | **$V_c$ (m/s)** | **$T_{in,c}$ (°C)** | **$V_{max,a}$ (m/s)** | **$T_{in,a}$ (°C)** |
|---|---|---|---|---|
| **1** | 3.6-4.1 | 6.6-11.9 | 1.2-8.7 | 33.1-36.8 |
| **2** | 3.6-3.8 | 7.2-8.3 | 1.2-8.1 | 33.6-38.3 |
| **5** | 2.5-2.53 | 11.2-11.9 | 1.4-8.3 | 34.1-34.7 |
| **6** | 2.3-2.5 | 7.3-8.9 | 1.5-9.7 | 33.5-34.6 |
| **7** | 2.5-2.51 | 7.9-11.3 | 1.5-9.9 | 33.5-34.3 |

Table 2.4 Steady-state experimental conditions for wet runs

| **HX** | **$V_c$ (m/s)** | **$T_{in,c}$ (°C)** | **$V_{max,a}$ (m/s)** | **$T_{in,a}$ (°C)** | **$Dwpt_{in,a}$ (°C)** |
|---|---|---|---|---|---|
| **1** | 3.37-3.52 | -0.45-1.69 | 1.27-7.78 | 30.2-36.1 | 23.8-24.0 |
| **2** | 3.33-3.63 | -0.2-2.1 | 1.33-8.18 | 30.3-36.4 | 23.8-24.9 |
| **3** | 2.54-2.59 | -0.1-1.4 | 1.59-9.81 | 33.9-34.6 | 23.8-24.0 |
| **4** | 2.55-2.64 | -0.4-2.3 | 1.44-8.62 | 33.5-34.3 | 23.9-24.0 |
| **5** | 2.54-2.58 | 0.0-2.4 | 1.53-8.22 | 33.8-35.0 | 23.9 |
| **6** | 2.45-2.59 | -0.1-1.1 | 1.69-9.13 | 33.5-34.1 | 23.7-24.0 |
| **7** | 2.57-2.59 | -0.2-1.4 | 1.57-9.0 | 34.3-34.5 | 23.8-23.9 |
| **8** | 2.56-2.6 | -0.2-1.3 | 1.59-9.26 | 34.1-34.3 | 23.9-24.1 |
| **9** | 2.56-2.58 | -0.1-1.1 | 1.5-8.21 | 33.6-34.6 | 23.9-24.0 |

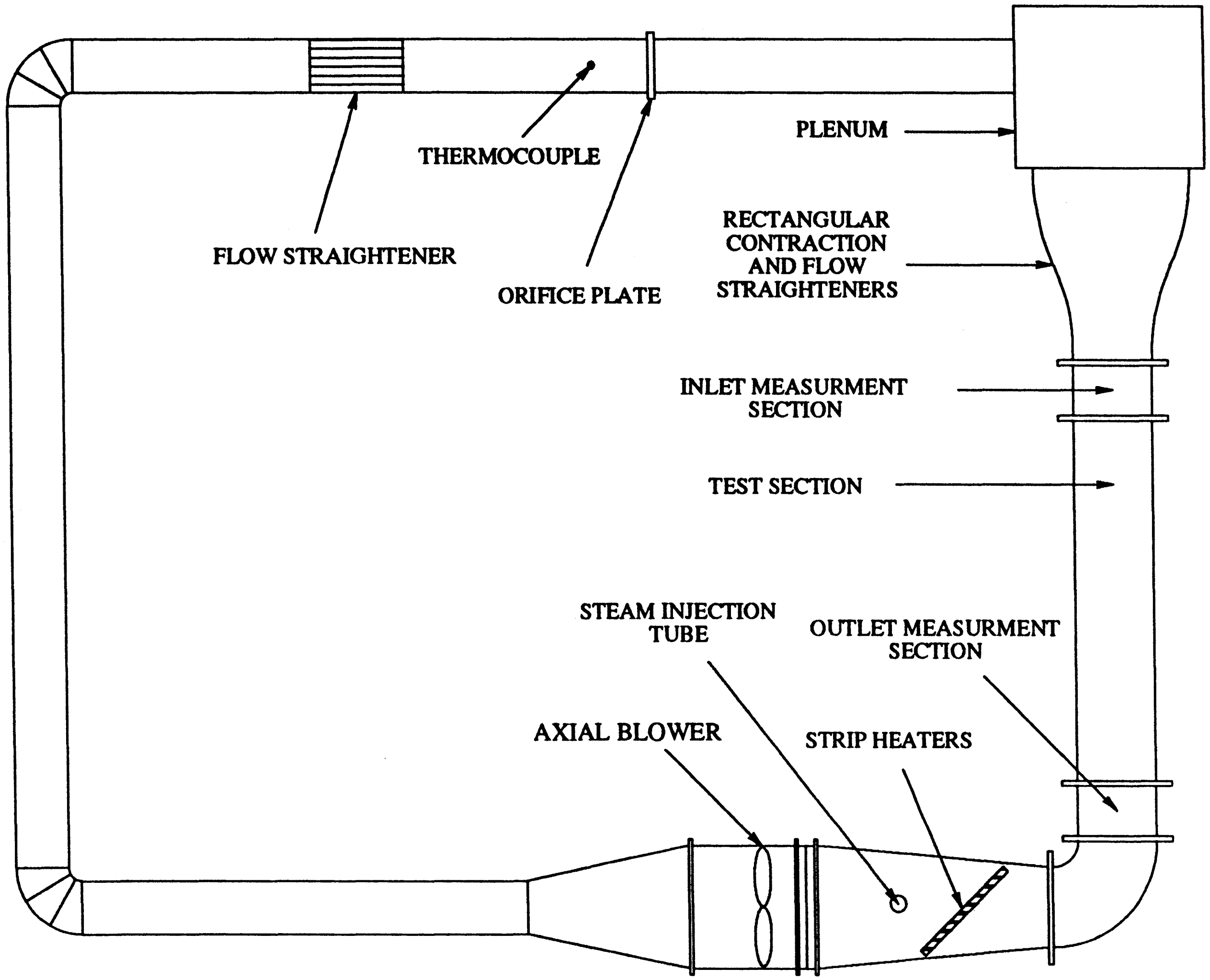

Figure 2.1 Wind tunnel for testing heat exchangers under condensing conditions

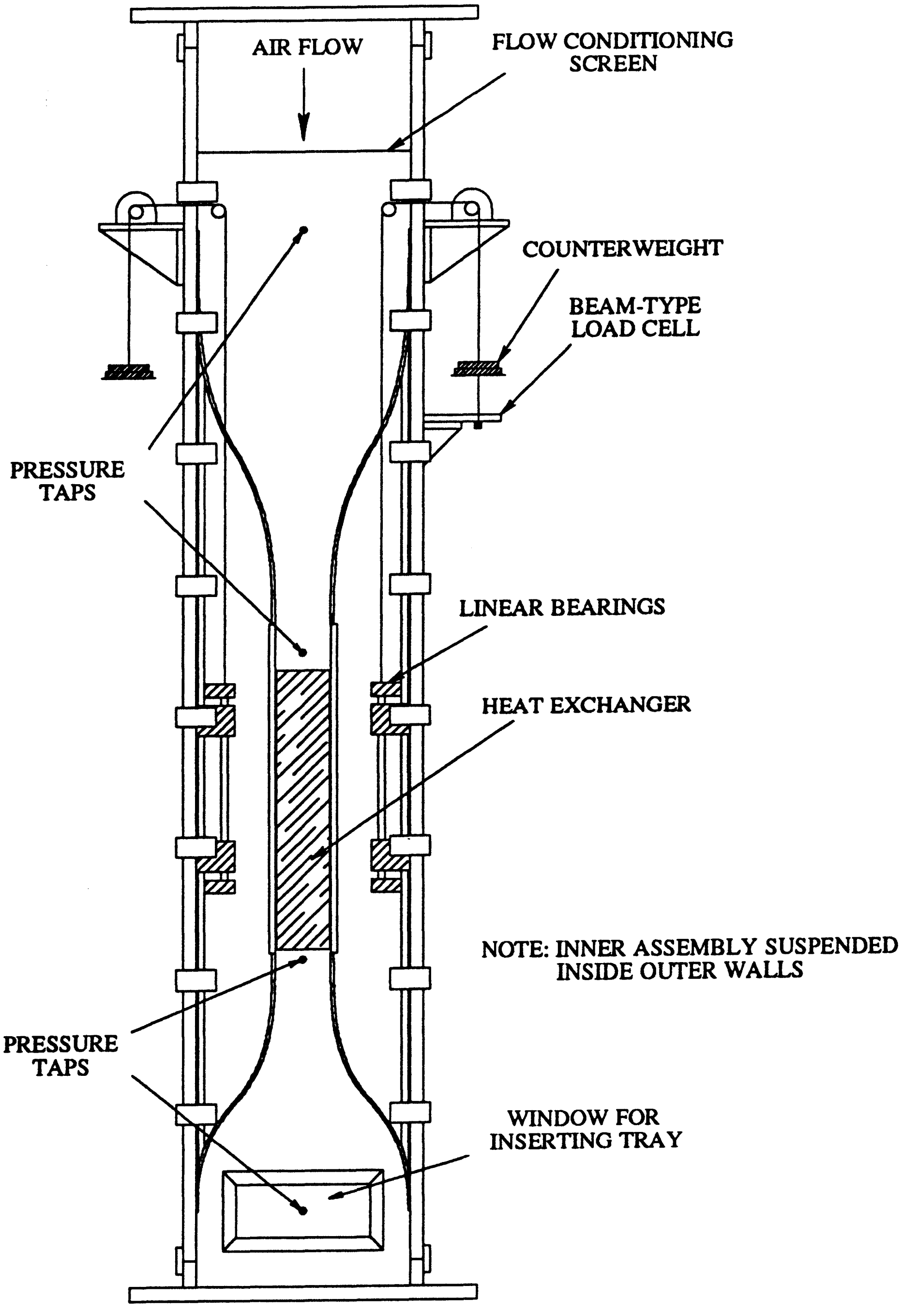

Figure 2.2 Test section for condensate retention experiments

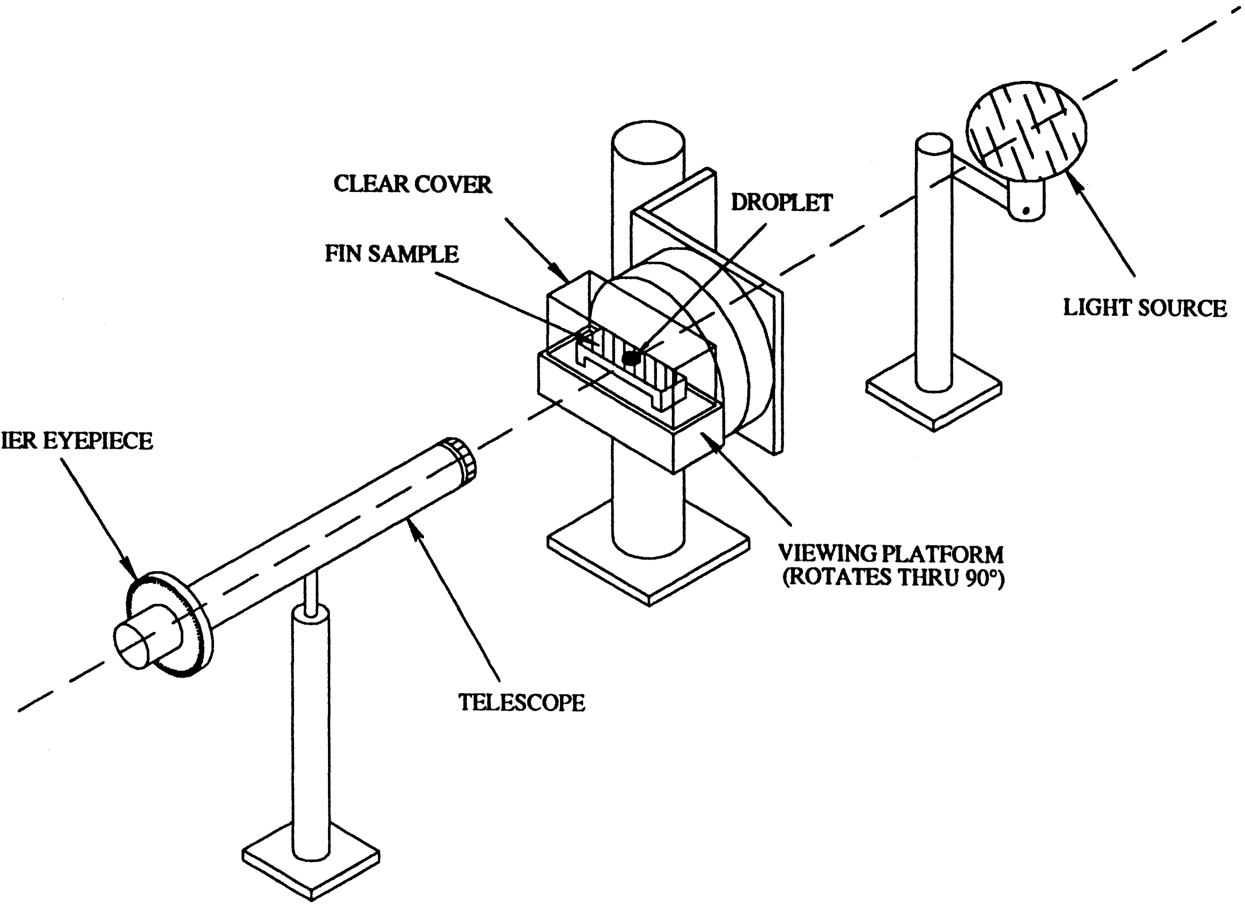

Figure 2.3 Contact angle goniometer

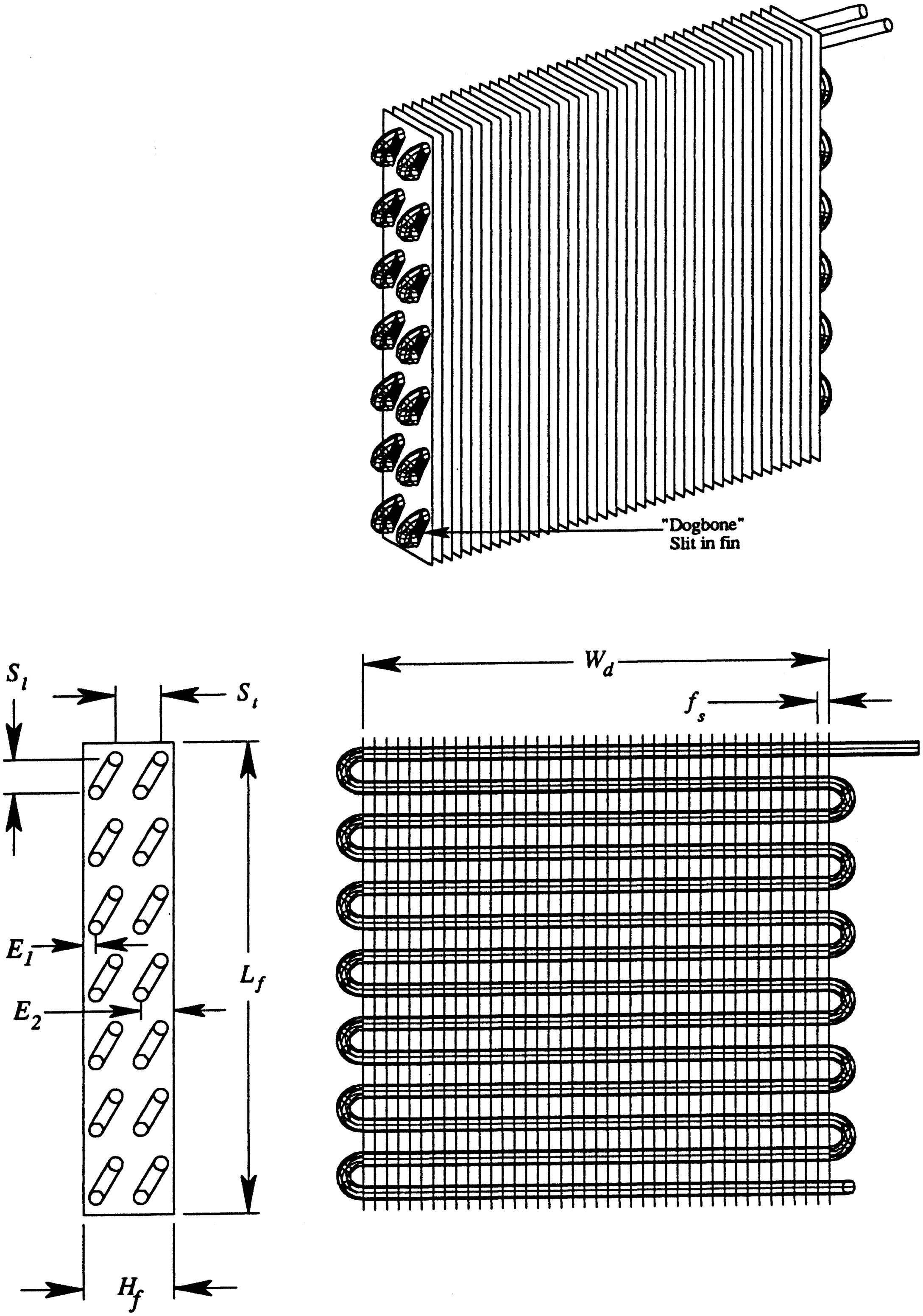

Figure 2.4 Heat exchanger geometry (HX's 1 and 2)

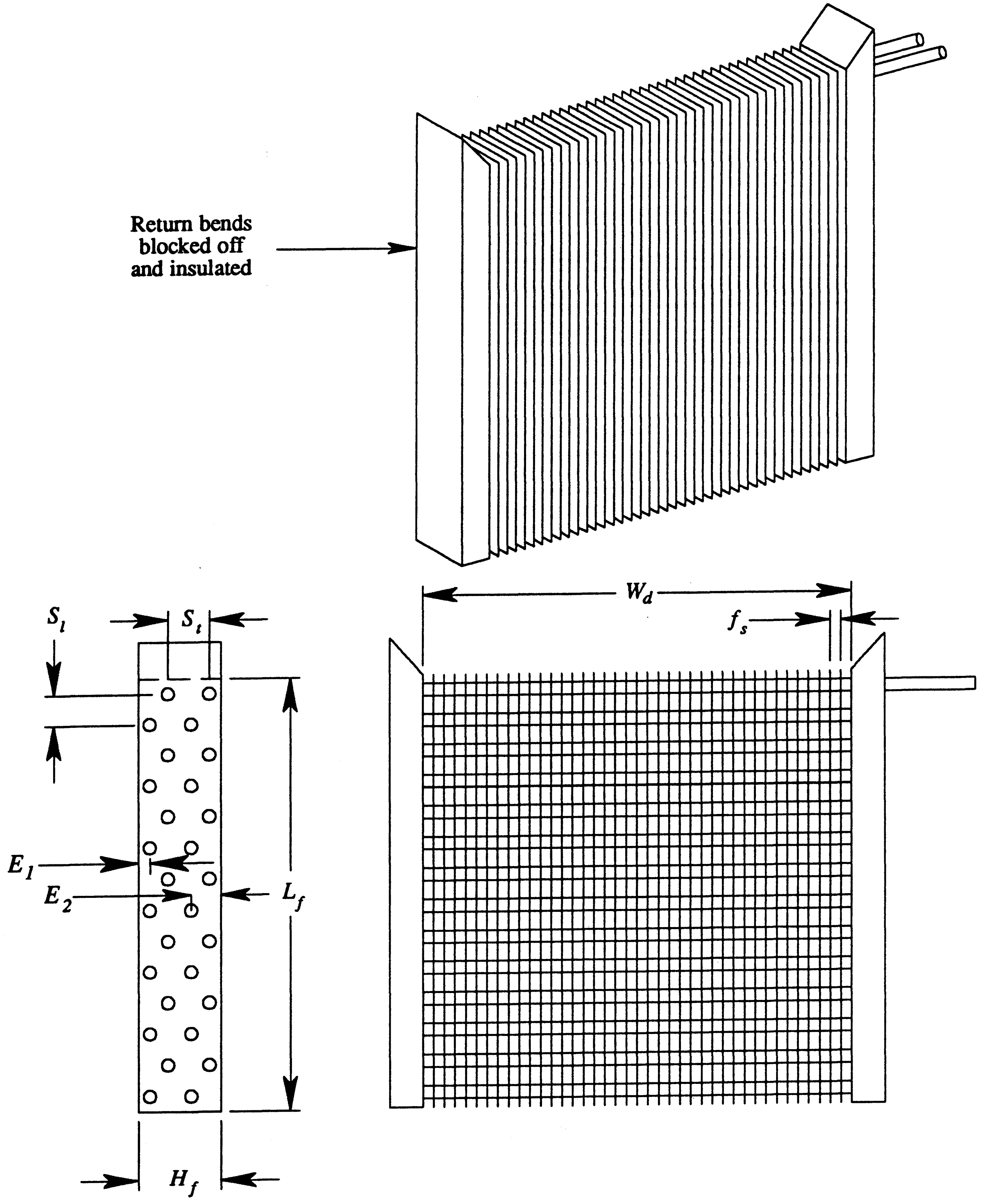

Figure 2.5 Heat exchanger geometry (HX's 3 - 9)

# Chapter 3 - Experimental Results and Discussion

The effects of retained condensate on the air-side performance of plate-fin-tube heat exchangers has been investigated. The quantity of retained condensate was determined by weighing heat exchangers in the test section as condensation occurred and by removing heat exchangers fully loaded with condensate. These results have been used to validate initial condensate retention modeling techniques and to provide direction for future refinements of these techniques.

## 3.1 Condensate Retention Results

### 3.1.1 Transient Condensate Retention

A test section was designed to provide real-time measurements of retained condensate in order to address experimental issues and further understand the dynamics of condensate retention. At the onset of this study it was not clear whether condensate retention was a steady or cyclic phenomenon. Two possible scenarios were considered. (1) Condensate may accumulate on the heat exchanger surfaces until there is a balance between condensate deposition and shedding. (2) The quantity of retained condensate may oscillate between maximum and minimum values due to periodic accumulation and shedding of condensate. Real-time measurements provided a means of validating measurements made by removing the heat exchanger and weighing it outside the test section. In addition, it is difficult to determine *a priori* the time required for a heat exchanger to reach a steady value of condensate retention for a given set of experimental conditions. The time required for a heat exchanger to reach a steady value of condensate retention could be determined from the real-time measurement.

Transient condensate retention measurements were recorded for heat exchangers 1 and 2 for velocities between 2.1 and 5.6 m/s based on the heat exchanger minimum free flow area. Difficulties in controlling the dewpoint and calibrating the load cell prevented real-time retention measurements at velocities outside this range. The load cell measured the weight of the retained condensate as well as the drag force increase associated with the retained condensate. The drag force increase was subtracted to determine the mass of the retained condensate. The load cell measurement was only valid for loading conditions due to hysteresis. The details of the real-time measurements are discussed in Appendix A.

The quantity of retained condensate increased and asymptotically approached a maximum value as shown in Figures 3.1 and 3.2. Condensate accumulated on the heat exchanger and began to shed as gravitational and air-flow forces overcame the surface-tension retaining forces. The quantity of retained condensate continued to increase eventually reaching a steady value, reflecting an equilibrium between condensate deposition and shedding. The time required to reach a steady value of retained condensate decreased or was unaffected by increases in air-flow rate. A decrease in the condensation rate is noticeable in Figures 3.1 and 3.2 slightly after condensation had begun. This decrease was due to the dewpoint of the inlet air falling while the PID controller adjusted the steam input rate to accommodate the dehumidification.

The quantity of retained condensate measured in the test section typically agreed within the experimental uncertainty with the value obtained by removing the heat exchanger and weighing it loaded with condensate. The value obtained by removing the heat exchanger is the steady-state value given in Figures 3.1 and 3.2. This value is indicated by the line crossing the vertical axis. The agreement between the maximum quantity of retained condensate recorded by the real-time measurement and the value obtained by removing the heat exchanger suggests that the quantity of retained condensate obtains a steady value and that any oscillations are within the experimental uncertainty. The real-time measurements exhibited good repeatability as shown in Figure 3.3. The real-time measurements validated heat exchanger removal as an accurate technique for determining condensate retention and were used to determine exposure times for later retention studies.

### 3.1.2 Steady-State Condensate Retention

#### A. Proposed Mechanisms for Condensate Removal (Shedding)

Steady-state condensate retention results were dependent on surface wettability, fin spacing, and air-flow rate. Different trends in the data were observed for variations in these parameters. Three different mechanisms of condensate removal are proposed in Figure 3.4. The first mode is appropriate for wide fin spacings with no interactions between condensate on adjacent fins. Condensate removal from one fin surface is independent of the adjacent fin surface. A condensate droplet travels down the fin coalescing with droplets in its path either leaving the heat exchanger or meeting a tube at a fin-tube junction. As the fin spacing decreases, condensate on one fin surface begins to interact with condensate on the adjacent fin surface. The occurrence of these interactions will depend on the surface wettability which determines the height of the droplet adhering to the fin surface. Droplets will be flatter as the surface wettability increases. Droplets on adjacent fins may interact in two different ways. (1) A droplet moves down the fin surface sweeping only one of the two adjacent fin surfaces until it grows large enough to come into contact with condensate on the adjacent fin. A condensate bridge then forms which continues to move down the heat exchanger sweeping both fin surfaces. (2) The drop departure size is large enough that droplets on adjacent surfaces grow to form a bridge before moving down the fin surface. This bridge then travels down the heat exchanger between the two fins sweeping both fin surfaces. A stable bridge could form between adjacent fins, especially at small fin spacings. This condition was not observed even for the lowest air-flow rates and smallest fin spacings of this study.

In addition to the shedding mechanisms proposed above, condensate shed from the tubes may interact with condensate on the fins. At wide fin spacings, droplets shed from the tubes may remove condensate from the fins. At tighter fin spacings condensate may be swept from adjacent fin surfaces by bridges shed from the wake region of a tube at a fin-tube junction as depicted in Figure 3.5. Shedding of a fin-tube bridge will depend on the local velocity, the size of the tube wake region, the quantity of condensate in the tube wake region and the advancing and receding contact angles. These shedding mechanisms may significantly influence condensate retention by effecting the size and distribution of retained condensate geometries.

### B. Condensate Retention Experiments I

Initial condensate retention studies included the Brazeway heat exchangers with 4 and 8 fpi (HX's 1 and 2). The steady-state quantity of retained condensate was determined by exposing the heat exchanger to prolonged condensing conditions and then removing the heat exchanger loaded with condensate. The heat exchanger was weighed, allowed to dry, and then weighed again to determine the quantity of retained condensate. The results are plotted in Figures 3.6 and 3.7 versus air velocity based on the minimum free flow area. Figure 3.6 provides the measured condensate retention and Figure 3.7 provides the measured condensate retention divided by the total heat transfer area. The quantity of retained condensate divided by the total heat transfer area was typically greater for the heat exchanger with wider fin spacing. These trends may be explained by shedding mechanisms. At tighter fin spacings, interactions between condensate on adjacent fin surfaces and between condensate shed from the tubes and condensate on the fins may act to decrease the quantity of retained condensate per unit area.

Figures 3.6 and 3.7 indicate a decrease in retained condensate for increasing air flow rates. The quantity of retained condensate appeared to be influenced by vapor shear and pressure drop forces. The results suggest that condensate departure size, which is affected by air-flow forces, governs retention behavior rather than condensate removal mechanisms or other effects which may lead to an increase in retained condensate with increasing air-flow rate. This decrease in retained condensate for increasing air-flow rate was not observed for the second set of retention experiments discussed in the next section.

There was a considerable amount of scatter in the data. Upon further investigation, much of this scatter was explained by wettability effects. Photographs of condensate and contact angle measurements revealed an increase in wettability for heat exchangers 1 and 2 over the course of the experiments. Figure 3.8 shows this change in wettability. Initially condensate formed as distinct droplets, typical of dropwise condensation. The condensation mode then became more filmwise. Rather than distinct droplets, irregular shaped droplets formed on the surface. As the wettability increased, the heat exchanger tubes were observed to be coated with a film rather than droplets. This change in wettability occurred during the first 100 hours of exposure to condensing conditions. Contact angle measurements verified the change in wettability and are reported in Section 3.3. Lubricants were used in manufacturing the heat exchangers, and it is possible that removal of these lubricants by the condensate was responsible for the change in surface wettability. The change in wettability could also have been due to contaminants accumulating on the heat exchanger surfaces.

The effect of the increase in surface wettability on condensate retention appeared to be dependent on the fin spacing. For heat exchanger 1 with 4 fpi, the increase in wettability reduced the quantity of retained condensate. For heat exchanger 2 with 8 fpi, the increase in wettability increased the quantity of retained condensate. Tables 3.1 and 3.2 show the variation in the quantity of retained condensate as the wettability increased. The first column provides the measurement number. It should be noted that these measurements were separated by an undefined number of wet-dry cycles and this table is provided only to show the trends in the quantity of retained condensate. The same effects of surface wettability on condensate retention were observed in the real-time measurements.

Except at the lowest air-flow rate, the quantity of retained condensate divided by the total area for heat exchanger 2 approached the quantity of retained condensate divided by the total area for heat exchanger 1 as the surface wettability increased. (See Figure 3.9) As the surface wettability increases, the condensate meets the fin surface at smaller advancing and receding contact angles. The droplet is flatter and does not extend as far from the fin surface. This shape may reduce interactions between condensate on adjacent fin surfaces and interactions between condensate shed from the tubes with condensate on the fins resulting in an increase in retained condensate.

The quantity of retained condensate for heat exchanger 1 decreased as the wettability increased. (See Table 3.1) As the wettability increases, the droplets on the fin surfaces are flatter and the volume of a droplet decreases for a given droplet diameter. If the same area of the heat exchanger is covered by condensate, the mass of retained condensate will decrease as the wettability increases. This explanation assumes that there are no interactions between condensate on adjacent fin surfaces which should be true as the fin spacing increases.

## C. Condensate Retention Experiments II

The experimental scope was extended to include heat exchangers with surface coatings and fin spacing down to 12 fpi. Different trends were observed for these heat exchangers. For example, an increase in the quantity of retained condensate was measured for increasing air-flow rates. This trend was not expected because air-flow forces on retained condensate increase as the air-flow rate increases.

The condensate retention data for heat exchangers 3 through 9 are provided in Table 3.3 with the air velocity based on the minimum free flow area. These results were obtained by exposing the heat exchanger to condensing conditions for at least one hour, removing the heat exchanger, weighing the heat exchanger wet, and then repeating the measurement with the heat exchanger dry. Real-time condensate retention measurements for heat exchangers 1 and 2 indicated that one hour should be sufficient for the quantity of retained condensate to reach steady state.

The effects of fin spacing and air flow rate on retained condensate are shown in Figure 3.10 for the Mt. Holly Gold specimens. Similar to the results for heat exchangers 1 and 2, the quantity of retained condensate divided by the total heat transfer area decreased as the fin spacing decreased. Figure 3.10 indicates an increase in retained condensate as the air-flow rate increases. This is contrary to the results for heat exchangers 1 and 2 where a decrease in retained condensate was observed with increasing air-flow rates.

The mechanisms for the increase in retained condensate with air-flow rate are not clearly understood; however, a few possibilities have been identified. A significant amount of condensate may accumulate as fin-tube bridges (Figure 3.5) in the wake regions behind the tubes. As the air-flow rate increases, the tube wake regions will grow in size and more condensate may be retained in these regions. The maximum quantity of condensate that may be retained as bridges at fin-tube junctions when neglecting air-flow forces was calculated based on the methods outlined in Section 4.3.2. The results of this analysis are shown in Table 4.1. The increase in retained condensate with increasing air-flow rates often exceeded the maximum calculated value of condensate retained as fin-tube bridges; therefore, it does not appear that this effect alone can account for all of the increase in retained condensate. Another possibility is that there is a change in the way condensate is being removed from the heat exchanger as the velocity increases. Condensate may be removed from the heat exchanger by mechanism (b) shown in Figure 3.4. For this condition condensate retention may be related to departure size, and early drop departure may lead to an increase in retained condensate because of decreased interaction between condensate on adjacent fins.

At the tightest fin spacing, 12 fpi, the effects of air-flow rate on condensate retention were minimal. This may indicate that condensate was being removed by mechanism (c) shown in Figure 3.4. For this condensate removal mechanism, the quantity of retained condensate may be independent of the air flow rate as long as stable bridges do not form between the adjacent fins at locations other than at fin-tube junctions. This type of bridging was not observed during condensate retention experiments.

The primary geometrical differences between heat exchangers 1 and 2 and heat exchangers 3 through 9 were the tube diameters and the fin geometries. These differences may explain the trends in retention behavior as related to air-flow rate. Tube wake effects for heat exchangers 1 and 2 should be less significant because the slits in the fins result in half the number of tube wake regions between fins compared to the solid fins. In addition, the tube diameters are smaller for heat exchangers 1 and 2 which will result in smaller wake regions and possibly smaller fin-tube bridges. Slits in the fins may limit the effects of condensate removal mechanisms because bridges traveling down a fin will meet the slit in the fin and travel toward the tube rather than continuing down the fin surfaces. Further experimental observations are required to identify condensate removal mechanisms which may be significant in modeling condensate retention.

The results for the Mt. Holly Gold specimens (HX's 3 and 4) agreed with the results for the uncoated specimens (HX's 6 and 7) as shown in Figure 3.11. The advancing and receding contact angles were similar for these surfaces. These results indicate that surfaces with similar wetting characteristics retain the same quantity of condensate if the heat exchanger geometry and operating conditions are identical. Contact angle measurements indicated similar wetting characteristics for several heat exchanger surface coatings which may result in similar quantities of retained condensate for heat exchangers with these coatings.

The effects of the Hycor, hydrophilic, surface coating on retained condensate are shown in Figure 3.12. The retained condensate was relatively independent of the air-flow rate for the hydrophilic surface. The influence of vapor-shear and pressure-drop forces on retained condensate depend on the size and shape of the retained condensate. The shape of a droplet adhering to a vertical fin surface will be different for the hydrophilic surface than the untreated and corrosion resistant surfaces. These differences may explain why air flow forces are less influential for the hydrophilic surface. The results indicate that for the tightest fin spacing (12 fpi) the quantity of retained condensate is relatively independent of the surface coatings. Condensate may be shedding by mechanism (c) in Figure 3.4, making condensate retention independent of air flow forces.

## 3.2 Condensate Retention Effects on Air-Side Heat Exchanger Performance

### 3.2.1 Air-Side Heat Transfer Results

The effects of condensate retention on air-side heat transfer were determined by conducting experiments under dry conditions and then conducting experiments with the entire heat exchanger wetted by condensate. The experimental results were reduced to provide sensible air-side heat transfer coefficients for both conditions. These coefficients were then compared to determine the effects of retained condensate on heat transfer performance.

Several options were considered in developing data reduction techniques for determining air-side heat transfer coefficients from the combined heat and mass transfer data. The data reduction procedures implemented were similar to those outlined in ARI Standard 410 [27]. The important differences were that the heat exchanger was discretized in the flow direction and the air-side heat transfer coefficient was determined by iteration following techniques similar to those applied by Mirth and Ramadhyani [11]. Various data reduction techniques were compared to determine the effects of these techniques on the calculated air-side heat transfer coefficient. The details of these considerations and the data reduction techniques are presented in Appendices B and C.

Sensible air-side heat transfer results for heat exchangers 1 and 2 are shown in Figures 3.13 and 3.14. For heat exchanger 1 with 4 fpi, there was an increase in sensible air-side Nusselt number for wet conditions compared to dry conditions at the same Reynolds number. The results for heat exchanger 2 with 8 fpi were inconclusive with sensible wet Nusselt numbers sometimes higher and sometimes lower than the corresponding dry values. Wide fin spacings may be able to sustain larger droplets since there will be less interaction between condensate droplets on adjacent fin surfaces. Heat transfer enhancement may depend on the size of condensate droplets on the heat transfer surface. These results were similar to the results of McQuiston [5] who observed an increase in air-side sensible performance under wet conditions for wide fin spacings (4 and 8 fpi) and a decrease in sensible performance under wet conditions for fin spacings less than 8 fpi. Curve fits are plotted with the data. These curve fits apply to the Nusselt numbers for Reynolds numbers greater than 1000 based on the tube diameter. Below this Reynolds number, air-side Nusselt numbers were significantly lower than the values predicted by these curve fits for both heat exchangers and for wet and dry conditions. This may indicate a change from fully developed laminar flow to turbulent flow.

Air-side heat transfer coefficients have been shown to be independent of fin spacing at a given mass velocity based on the minimum free flow area for plate-fin-tube heat exchangers operating under dry conditions [28]. Similar results were observed by Fu *et al.* [13] for louvered finned tube heat exchangers. Figure 3.15 shows the effects of fin spacing on dry air-side Nusselt numbers. The tube diameters were equivalent for heat exchangers 1 and 2; therefore, equivalent dry Nusselt numbers were expected for the same Reynolds number based on the tube diameter. The data have been fit with a common correlation for Reynolds numbers between 1000 and 4500. All of the data fell within 12% of this correlation over this range of Reynolds number with Nusselt numbers for HX 1 typically being slightly higher than Nusselt numbers for HX 2.

### 3.2.2 Sensible j and friction factors (Wet and Dry)

The sensible j factors and friction factors for heat exchangers 1 and 2 are presented in Figure 3.16 and Figure 3.17. Sensible j factors and friction factors were calculated using Equations 3.1 and 3.3. Entrance and exit loss effects have been included in the friction factor. The air-side Reynolds number was calculated based on the tube diameter (Equation 3.4).

$$j = St\,\mathrm{Pr}^{2/3} \tag{3.1}$$

$$St = \frac{Nu}{\mathrm{Re}\,\mathrm{Pr}} = \frac{h}{GCp_{ma}} \tag{3.2}$$

$$f = \frac{2\Delta P_{HX}\rho_a}{G^2}\left(\frac{A_{\min}}{A_{tot}}\right) - \left(1+\sigma^2\right)\left(\frac{\rho_{a,1}}{\rho_{a,2}} - 1\right)\left(\frac{A_{\min}}{A_{tot}}\right)\left(\frac{\rho_a}{\rho_{a,1}}\right) \tag{3.3}$$

where

$$\rho_a = \frac{\rho_{a,1} + \rho_{a,2}}{2}$$

$$\mathrm{Re}_{D_{o,t}} = \frac{GD_{o,t}}{\mu_a} \tag{3.4}$$

The effect of condensation on the air-side friction factor was negligible for heat exchanger 1 with 4 fpi; however, there was a significant increase in friction factor for heat exchanger 2 with 8 fpi under wet conditions. At fin spacings of 4 fpi, McQuiston noted an increase in friction factor for dropwise condensation but not for filmwise condensation [5]. The mode of condensation for these studies varied from dropwise to filmwise (See Figure 3.8). The increase in friction factor for heat exchanger 2 is more pronounced at low Reynolds numbers which agrees with the results of McQuiston [5].

### 3.2.3 Surface Coating Effects on Air-Side Friction Factor

The effects of surface coatings on air-side friction factors were determined by recording heat exchanger differential pressures under wet and dry conditions. Under wet conditions the heat exchanger differential pressure was measured after allowing sufficient time for the quantity of retained condensate to reach a steady value. Friction factors were calculated using Equation

3.3. Heat exchangers 3 through 9 had fin collars covering the tubes. The Reynolds number was calculated based on the collar diameter rather than the tube diameter (Equation 3.5):

$$\mathrm{Re}_{D_{coll}} = \frac{V_{\max}\rho_a D_{coll}}{\mu_a} \tag{3.5}$$

The effects of the surface coatings on friction factors are shown in Figures 3.18 to 3.20. For the widest fin spacing, approximately 8 fpi, similar friction factors were obtained for wet and dry conditions for the uncoated sample. Slightly higher friction factors were recorded for the Mt. Holly Gold corrosion resistant surface coating at high Reynolds numbers. These results are significantly different from the results obtained for heat exchanger 2 which also had 8 fpi. For heat exchanger 2, an increase in friction factor was observed for wet conditions and this increase diminished with increasing Reynolds number. At fin spacings of approximately 10 fpi, the Mt. Holly Gold surface resulted in the largest increase in friction factor when compared to the dry aluminum surface. This increase was apparent over the entire Reynolds number range. The friction factor increase for the wet condition was similar for the Hycor hydrophilic surface and the uncoated aluminum surface with the increase in friction factor increasing with increasing Reynolds numbers. Similar friction factor trends were observed at 12 fpi. Once again the Mt. Holly Gold surface exhibited the largest friction factor increase for wet conditions and this increase was noticeable over the entire Reynolds number range. An increase in friction factor was observed for the Hycor, hydrophilic, surface for wet conditions when compared to the dry Mt. Holly Gold surface at high Reynolds numbers. The hydrophilic surface did not provide a clear advantage in terms of the friction factor under wet conditions. The friction factor performance for the hydrophilic and uncoated aluminum surfaces were similar at 10 fpi under wet conditions. Both the uncoated aluminum and hydrophilic surface provided smaller wet friction factors than the Mt. Holly Gold surface. The Mt. Holly Gold surface is the least hydrophilic of the three surfaces and this may lead to the higher friction factors for wet conditions.

## 3.3 Contact Angle Measurements

### 3.3.1 Background

The contact angle is defined as the angle between the liquid-vapor interface and the solid measured through the liquid at the contact line where the liquid, solid, and vapor phases meet (See Figure 3.21). The contact angle is measured to characterize the wettability or affinity of the liquid for the solid. Many researchers have used the equilibrium contact angle of a liquid drop placed on a solid surface to characterize wettability and this a common technique for heat transfer surfaces. This angle is a fundamental measurement only for smooth, homogenous, solids without surface impurities. Real heat transfer surfaces do not meet these ideal conditions and a drop placed on the surface will obtain an equilibrium contact angle between $\theta_A$ and $\theta_R$, the advancing and receding contact angles. A region of equilibrium will exist between $\theta_A$ and $\theta_R$ which often covers several dozen degrees as discussed by Chappuis [29]. The angle measured by placing a drop on a solid surface and recording the equilibrium angle will be dependent on the way this angle was established, the drop size, and other factors. For these reasons, the advancing and receding contact angles are of more interest for heat transfer surfaces. In addition, the advancing and receding contact angles are the significant angles in defining retention characteristics.

Contact angle hysteresis, the difference between advancing and receding contact angles, provides the interfacial surface tension forces necessary for a droplet to remain on a vertical surface against the effects of gravity and air flow forces. The advancing contact angle, the maximum possible contact angle, is the angle established as the contact line advances over a previously unwetted portion of the solid. The receding contact angle, the minimum possible contact angle, is established as the contact line recedes over a previously wetted portion of the solid. These different values for the contact angle and contact angle hysteresis are attributable to surface inhomogeneity, surface roughness, and surface impurities [30]. How these angles relate to drop departure size is discussed in Chapter 4.

### 3.3.2 Measurement Techniques for Advancing and Receding Contact Angles

Various techniques exist for measuring advancing and receding contact angles. Some of these techniques are discussed by Johnson and Dettre [31]. Figure 3.22 illustrates these various techniques. Advancing and receding contact angles are established using technique (a) by keeping a syringe or capillary in contact with the liquid droplet. The liquid is fed or withdrawn to establish the advancing and receding contact angles. These angles are the angles just prior to incipient motion of the contact line. This procedure may be modified, (b), by feeding and withdrawing the liquid through a capillary in the solid surface. The third technique, (c), is achieved by keeping the syringe or capillary in contact with the droplet and moving the solid and syringe with respect to each other. The advancing and receding contact angles are established as the liquid moves over the solid surface. A fourth technique, (d), is achieved by tilting the solid surface. The angles formed as the drop begins to move down the solid are the advancing and receding contact angles.

Two techniques were implemented during this course of this study to determine advancing and receding contact angles. Technique (a) of Figure 3.22 was performed by advancing and withdrawing liquid using a syringe and measuring the advancing and receding angles using the contact angle goniometer described in Section 2.1.4. These results were compared to a second technique. The second technique was similar to technique (d) of Figure 3.22. Droplets were placed on a fin stock specimen and the specimen was rotated through 90°. The droplet volume was varied to determine the maximum size droplet that would adhere to the surface rather than moving down the test specimen at 90°. The advancing and receding contact angles were then measured using the contact angle goniometer for a droplet of this size on the specimen which was rotated 90°. For both techniques the vapor pressure was controlled by placing water in a trough around the test specimen holder and placing a cover over the specimen. Ultrapure, milliQ, water was used for all contact angle measurements.

### 3.3.3 Average Advancing and Receding Contact Angles

Contact angle measurements were made by three different observers using the two techniques. Variations in advancing and receding contact angles were observed for different sides of the fin stock material and for different locations on the same side. Average values of the measured advancing and receding contact angles for the fin material supplied by Brazeway are shown in the first three rows of Table 3.4. Heat exchangers 1 and 2 were produced using this fin material. Good agreement was achieved between the values obtained by the three observers and the two techniques.

The effects of wet-dry cycling are evidenced in Table 3.4. The last column of Table 3.4 provides average values of the measured advancing and receding contact angles after experimental testing. A change in wettability was observed in photographs of retained condensate (Figure 3.8) and this change is reflected in the contact angle results. These contact angles were measured by cutting apart the heat exchanger and creating specimens from different positions along the length of the fin. An increased standard deviation was observed for the contact angle measurements after exposure to condensing conditions. This was due to the increase in surface wettability varying over the surface of the fin.

Average advancing and receding contact angles measured for fin materials provided by HeatCraft are provided in Table 3.5. These measurements included the fin materials and surface coatings used in manufacturing heat exchangers 3 through 9 included in the second set of condensate retention experiments. The contact angles measured for the untreated aluminum surface provided by HeatCraft were similar to the measured values for samples taken from the untreated aluminum Brazeway heat exchangers after the experiments. This similarity may indicate that the increase in wettability observed for heat exchangers 1 and 2 is a result of lubricants on the fin surface which are removed by the condensate. The Mt. Holly Gold surface coating increased both the advancing and receding contact angles compared to the uncoated aluminum specimen providing a more hydrophobic surface. The effect of the hydrophilic coating produced by JW Aluminum was a decrease in both advancing and receding contact angles; however, the ALCOA hydrophilic did not exhibit hydrophilic behavior. There were significant differences in the contact angles measured by the two different techniques and by different observers for the hydrophilic surfaces. It is not clear why these differences arose, and measurements of contact angles for hydrophilic surfaces should be further investigated.

Table 3.1 Wettability effects on retained condensate (HX 1, uncoated Al, 4 fpi)

| Measurement # | $V_{max}$ (m/s) | Retained Condensate (g) |
|---|---|---|
| 1 | 2.8 | 144 |
| 2 | 3 | 124 |
| 3 | 3.1 | 119.6 |
| 4 | 3.2 | 107.2 |

Table 3.2 Wettability effects on retained condensate (HX 2, uncoated Al, 8 fpi)

| Measurement # | $V_{max}$ (m/s) | Retained Condensate (g) |
|---|---|---|
| 1 | 5.6 | 137.3 |
| 2 | 5.6 | 167.4 |
| 3 | 5.6 | 175 |
| 4 | 5.6 | 187.9 |
| 5 | 5.5 | 202.7 |

Table 3.3 Condensate retention results (HX's 3 through 9)

| HX | $V_{max}$ (m/s) | Retained Condensate (g) | Condensate/$A_{tot}$ (g/m$^2$) |
|---|---|---|---|
| 3 | 1.59 | 164.3 | 81.3 |
| 3 | 2.45 | 178.3 | 88.2 |
| 3 | 4.72 | 188.6 | 93.3 |
| 3 | 9.81 | 208.6 | 103.2 |
| 4 | 1.44 | 161.4 | 65.8 |
| 4 | 2.36 | 186.1 | 75.9 |
| 4 | 4.49 | 190.8 | 77.8 |
| 4 | 8.62 | 211.6 | 86.3 |
| 5 | 1.53 | 185.8 | 63.4 |
| 5 | 2.42 | 197.9 | 67.5 |
| 5 | 4.38 | 196.5 | 67.1 |
| 5 | 8.22 | 204.4 | 69.8 |
| 6 | 1.69 | 159 | 78.7 |
| 6 | 2.55 | 174 | 86.1 |
| 6 | 4.82 | 175.6 | 86.9 |
| 6 | 9.13 | 215 | 106.4 |

|  |  |  |  |
|---|---|---|---|
| **7** | 1.57 | 166.9 | 66.2 |
| **7** | 2.51 | 183.9 | 72.9 |
| **7** | 4.64 | 194.6 | 77.2 |
| **7** | 9 | 212.2 | 84.2 |
| **8** | 1.59 | 172.1 | 70.6 |
| **8** | 2.49 | 176.9 | 72.6 |
| **8** | 4.6 | 170.9 | 70.1 |
| **8** | 9.26 | 180.4 | 74.0 |
| **9** | 1.5 | 175.2 | 60.1 |
| **9** | 2.41 | 192.2 | 65.9 |
| **9** | 4.66 | 190.8 | 65.4 |
| **9** | 8.21 | 191.9 | 65.8 |

Table 3.4 Contact angle measurements for fin materials supplied by Brazeway
Techniques: (1) feeding and withdrawing liquid (2) rotating sample through 90°

| **Mat.** | **Coating** | **Observer** | **Technique** | **Condition** | **$\theta_A$** | **Standard Dev.** | **$\theta_R$** | **Standard Dev.** |
|---|---|---|---|---|---|---|---|---|
| Al | None | 1 | 1 | New | 94.4° | 1.1° | 52.9° | 5.1° |
| Al | None | 2 | 1 | New | 91.7° | 1.4° | 50° | 3.2° |
| Al | None | 3 | 2 | New | 90.9° | 1.5° | 56.2° | 6.7° |
| Al | None | 3 | 2 | <100 hrs wet-dry cycling | 81.9° | 10.8° | 35.1° | 7° |

Table 3.5 Contact angle measurements for fin materials supplied by HeatCraft Techniques: (1) feeding and withdrawing liquid (2) rotating sample through 90°·

| **Mat.** | **Coating** | **Observer** | **Technique** | **Condition** | $\theta_A$ | **Standard Dev.** | $\theta_R$ | **Standard Dev.** |
|---|---|---|---|---|---|---|---|---|
| Al | None | 3 | 2 | New | 80.5° | 1.4° | 34.4° | 2.4° |
| Al | FOA Gray | 1 | 1 | New | 92° | 1.2° | 57.5° | 1.5° |
| Al | Mount Holly Gold | 1 | 1 | New | 91.8° | 1.2° | 56.7° | 2.4° |
| Al | Mount Holly Gold | 2 | 1 | New | 87.8° | 4.1° | 49.2° | 2.3° |
| Al | Mount Holly Gold | 3 | 2 | New | 82.2° | 2.3° | 48.3° | 2.4° |
| Al | ALCOA Hydrophilic | 1 | 1 | New | 97° | 1.7° | 49.9° | 3.3° |
| Al | ALCOA Hydrophilic | 2 | 1 | New | 92.9° | 1° | 62.6° | 1° |
| Al | JW Hydrophilic (Hycor) | 2 | 1 | New | 55.1° | 1.6° | 37.6° | 1.1° |
| Al | JW Hydrophilic (Hycor) | 3 | 2 | New | 64.5° | 5.5° | 25.5° | 3.7° |

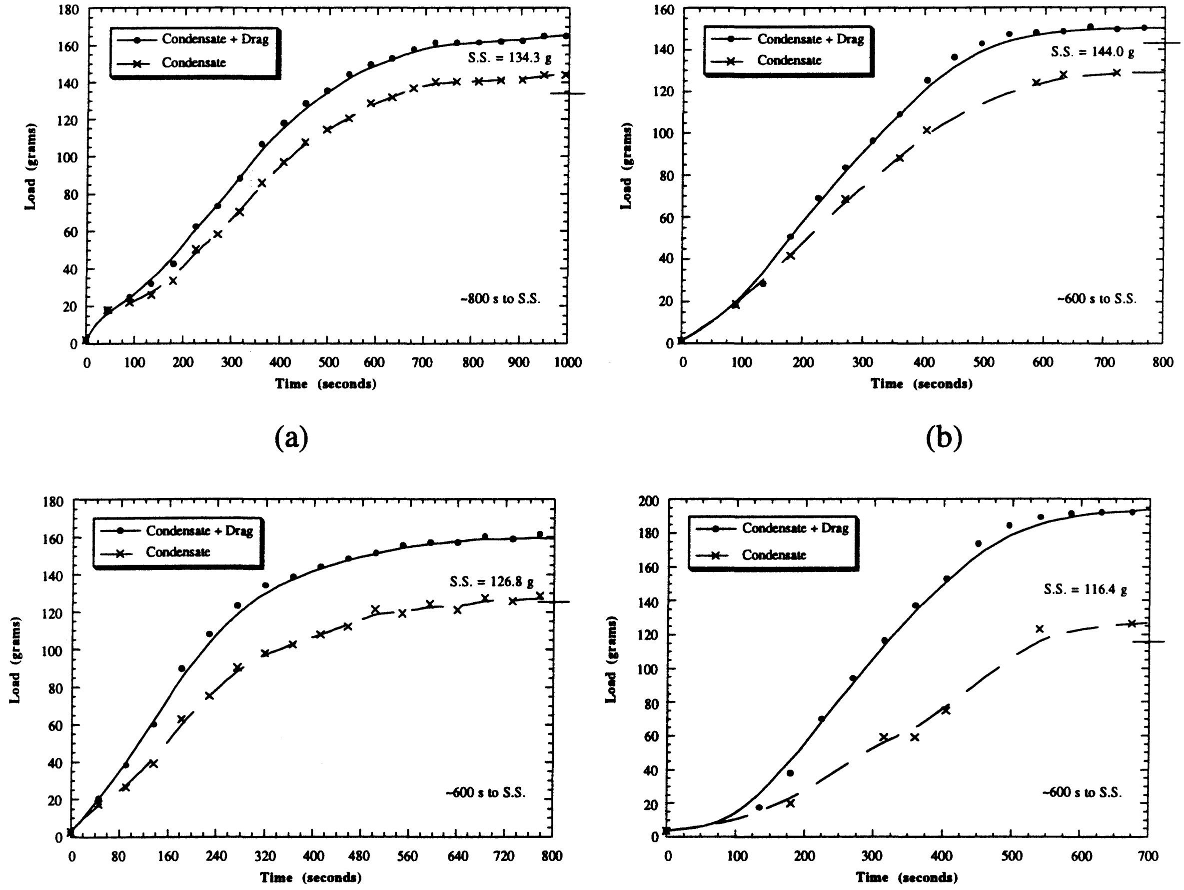

(a) (b)

(c) (d)

Figure 3.1 Retention plots for HX 1 (Uncoated Al, 4 fpi)
Inlet air conditions: $T_1$ ~34°C, $dwpt_1$ ~23.9°C
(a) $V_{max}$ = 2.2 m/s (b) $V_{max}$ = 2.8 m/s (c) $V_{max}$ = 3.9 m/s (d) $V_{max}$ = 6.0 m/s

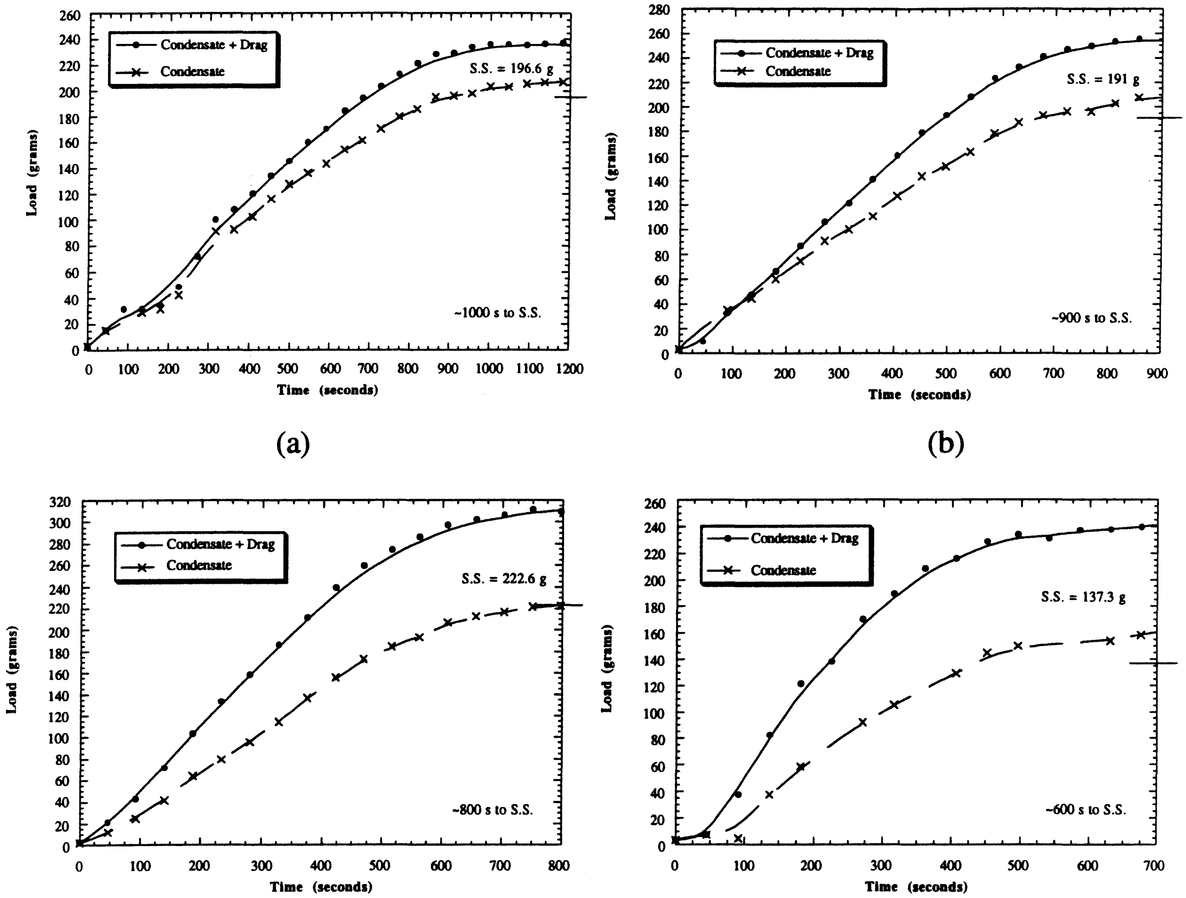

(a) (b)

(c) (d)

Figure 3.2 Retention plots for HX 2 (Uncoated Al, 8 fpi)
Inlet air conditions: $T_1$ ~34°C, $dwpt_1$ ~23.9°C
(a) $V_{max}$ = 2.1 m/s (b) $V_{max}$ = 2.8 m/s (c) $V_{max}$ = 3.6 m/s (d) $V_{max}$ = 5.6 m/s

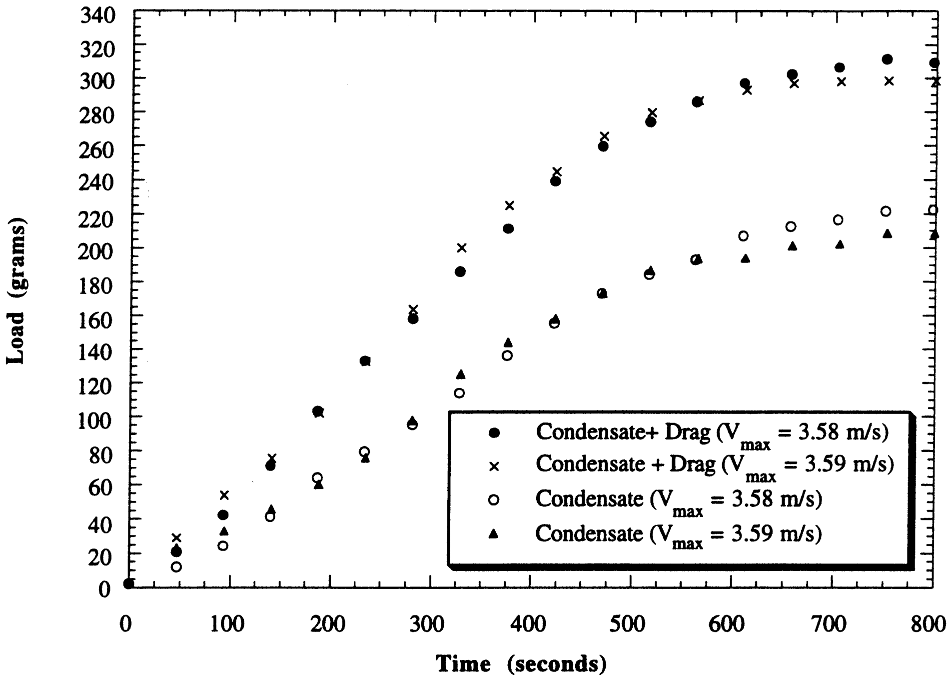

Figure 3.3 Condensate retention plots for HX 2 (Uncoated Al, 8 fpi) illustrating repeatability of measurement technique

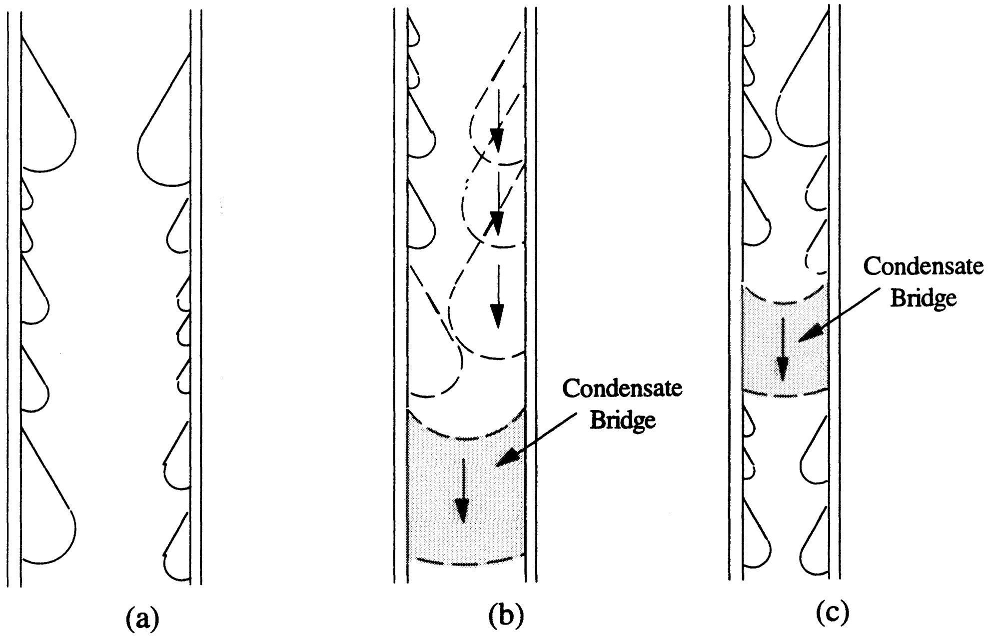

Figure 3.4 Condensate removal mechanisms (a) no interaction between droplets on adjacent fins, droplet grows to departure size and moves down the fin surface (b) droplet grows to departure size on one fin surface and moves down the fin surface growing by coalescence until it meets a droplet on the adjacent fin to form a bridge which moves down the fins (c) droplets grow on adjacent fins and meet forming a bridge which moves down the fins

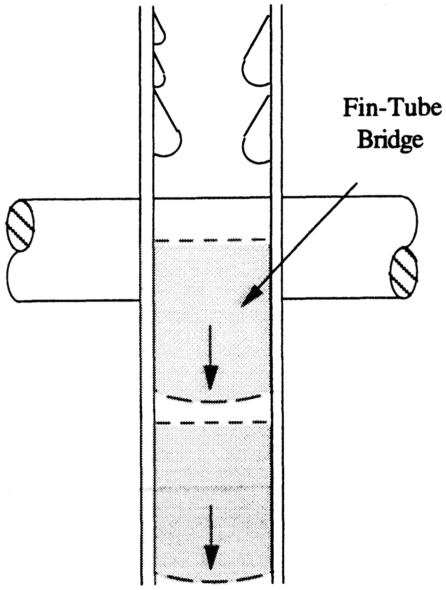

Figure 3.5 Condensate removal by fin-tube bridge sweeping adjacent fins

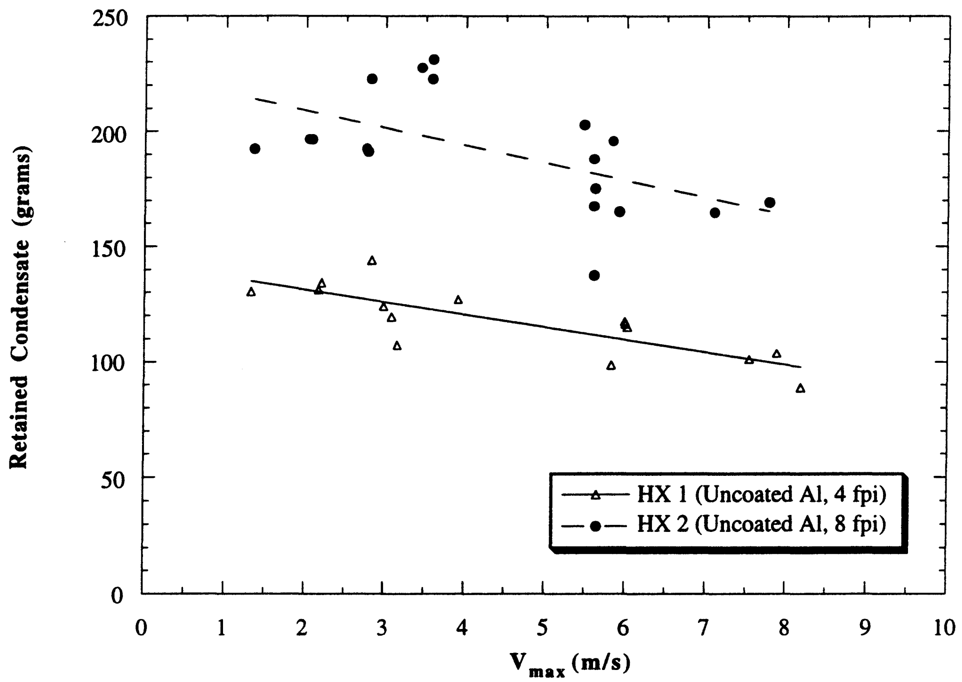

Figure 3.6 Steady-state condensate retention for HX's 1 and 2

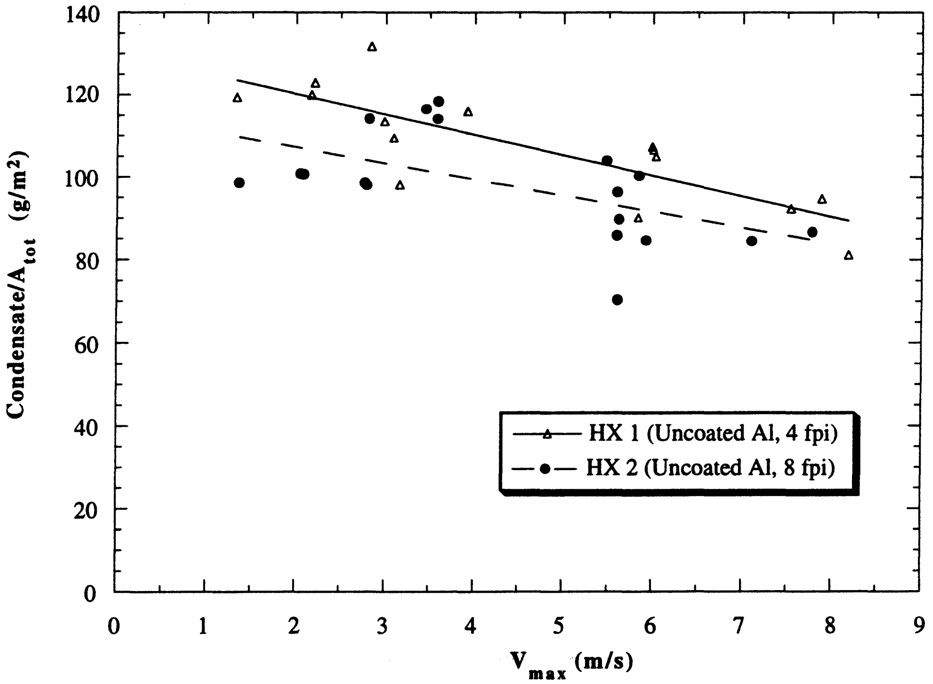

Figure 3.7 Steady-state condensate retention / $A_{tot}$ for HX's 1 and 2

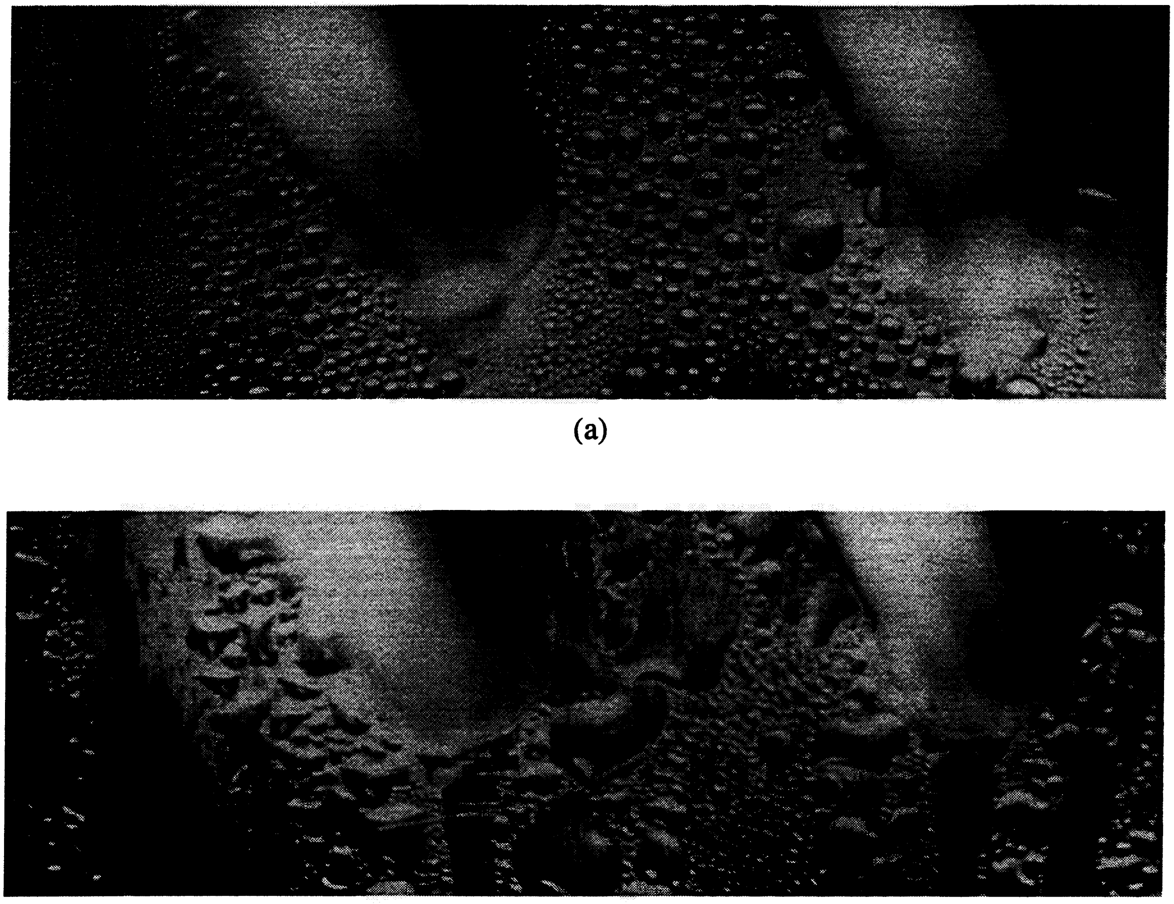

(a)

(b)

Figure 3.8 Change in wettability during first 100 hours of exposure to condensing conditions (a) dropwise condensation (b) mixed mode dropwise-filmwise condensation

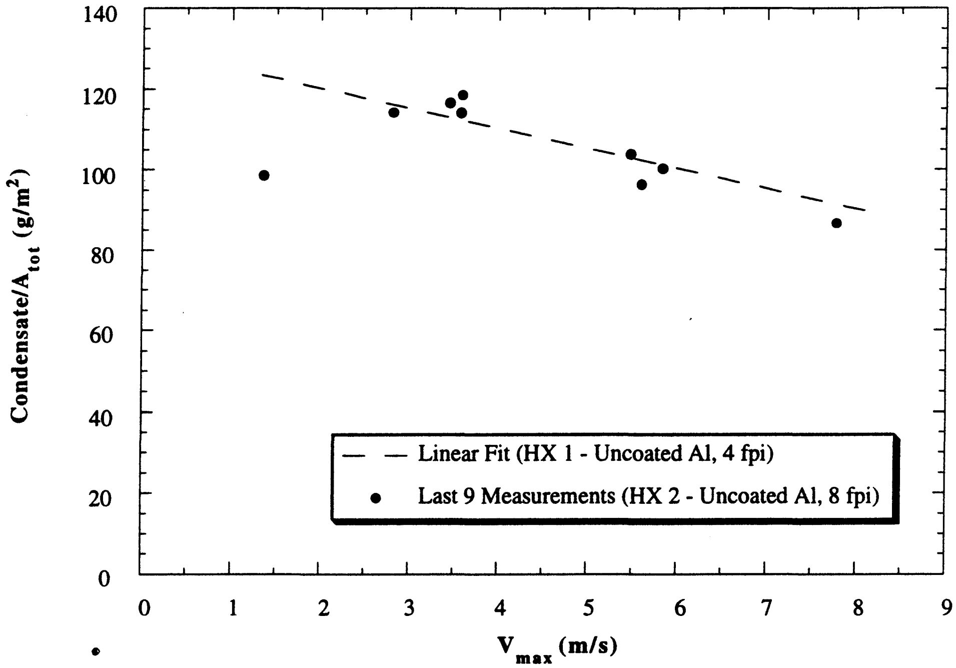

Figure 3.9 Effect of increased wettability on retained condensate / $A_{tot}$ (HX 2)

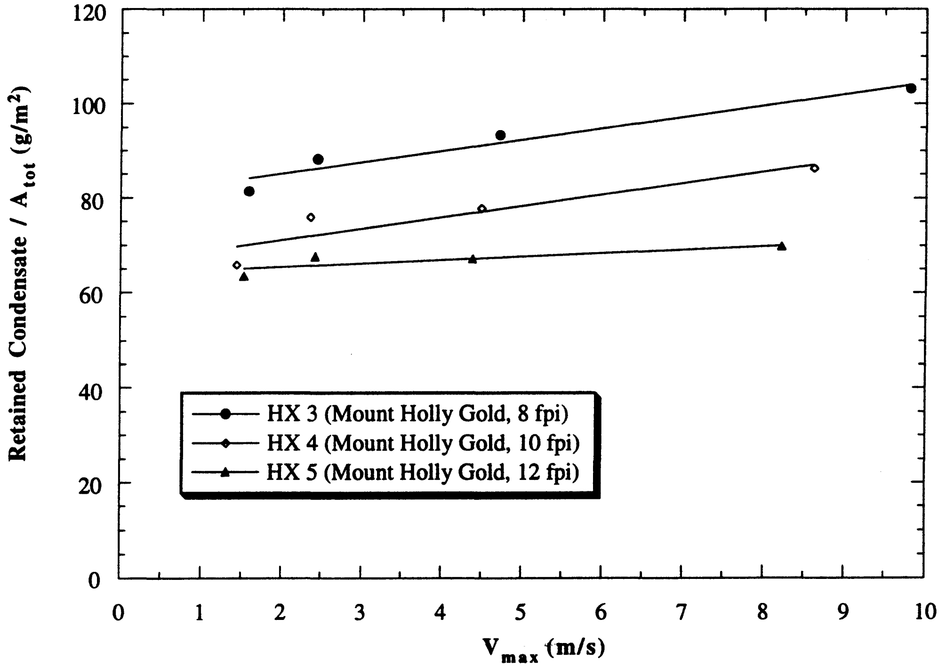

Figure 3.10 Effects of fin spacing on retained condensate

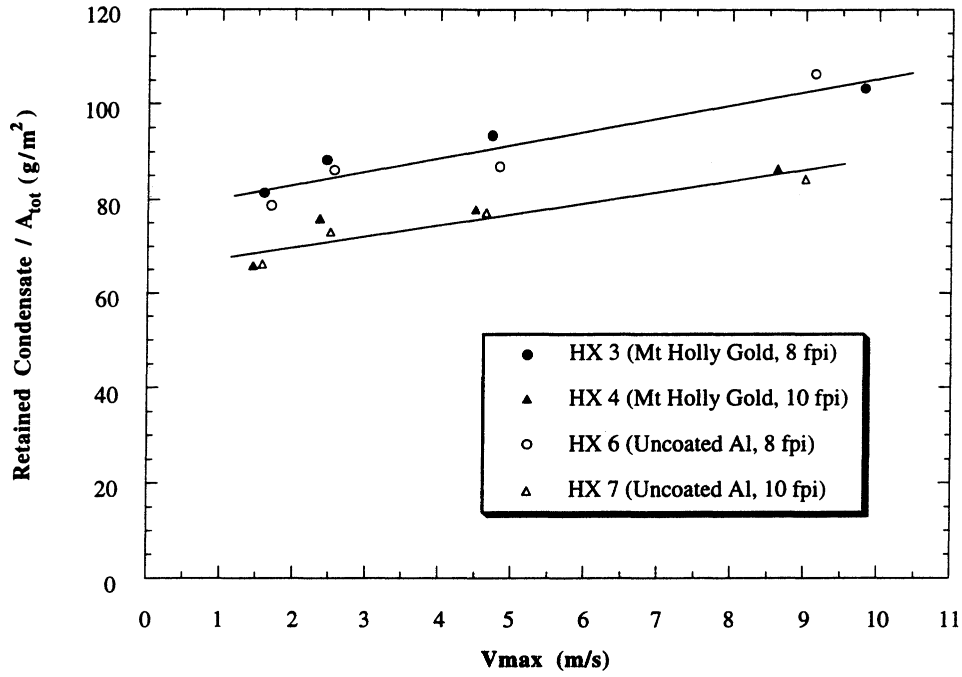

Figure 3.11 Effects of Mt. Holly Gold surface coating on condensate retention

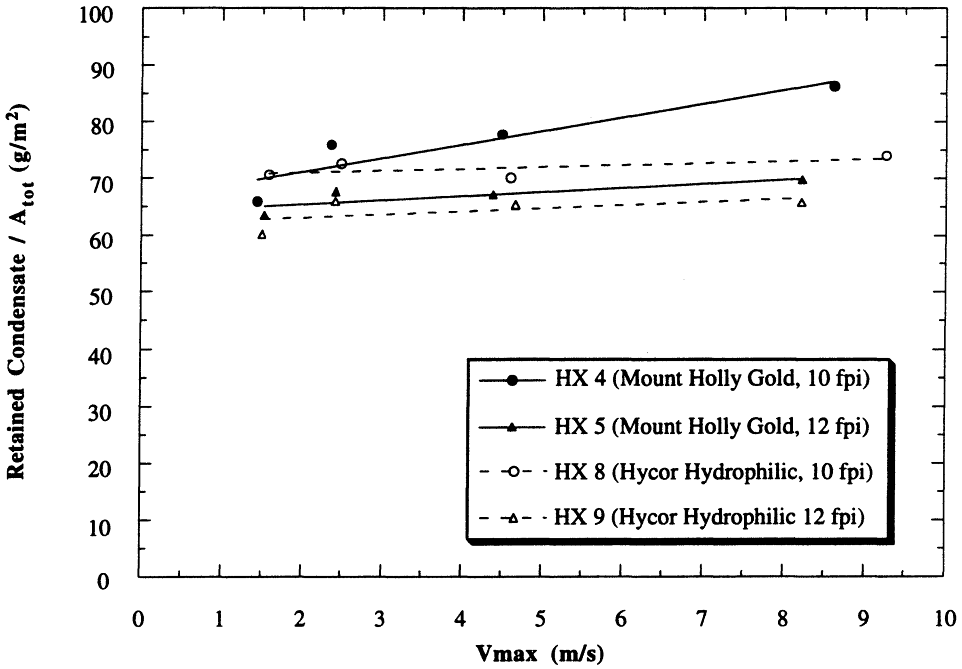

Figure 3.12 Effects of hydrophilic surface coating on retained condensate

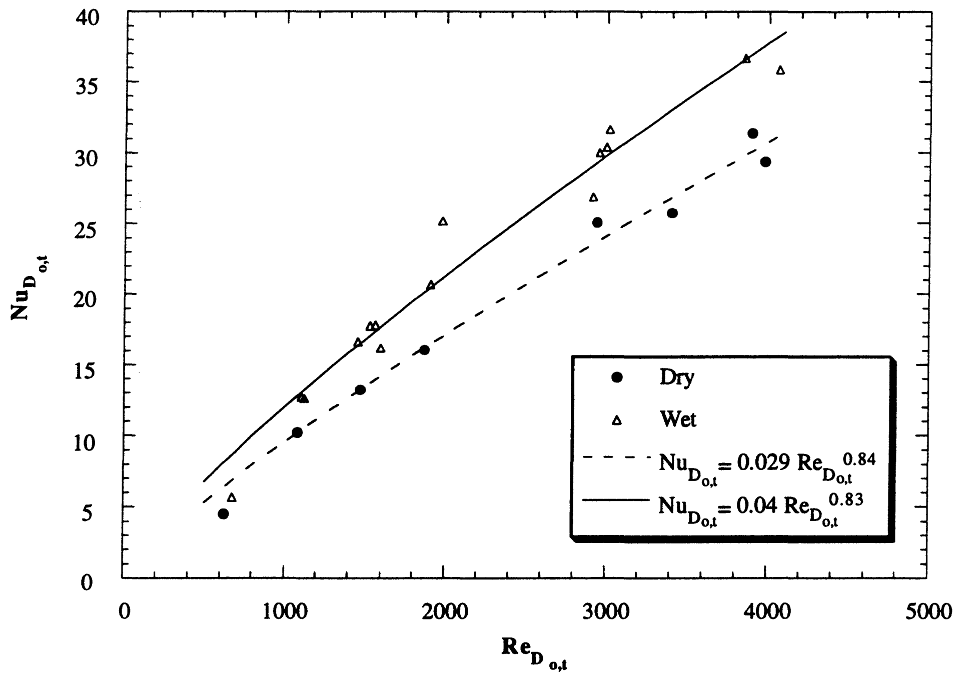

Figure 3.13 Air-side sensible heat transfer results for HX 1 (uncoated Al, 4 fpi)

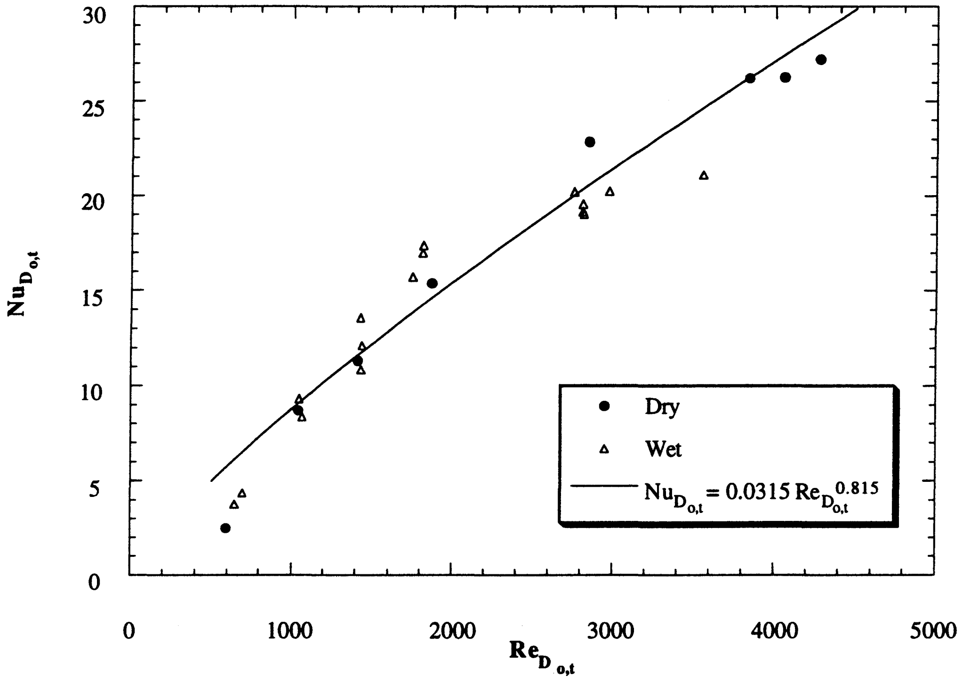

Figure 3.14 Air-side sensible heat transfer results HX 2 (uncoated Al, 8 fpi)

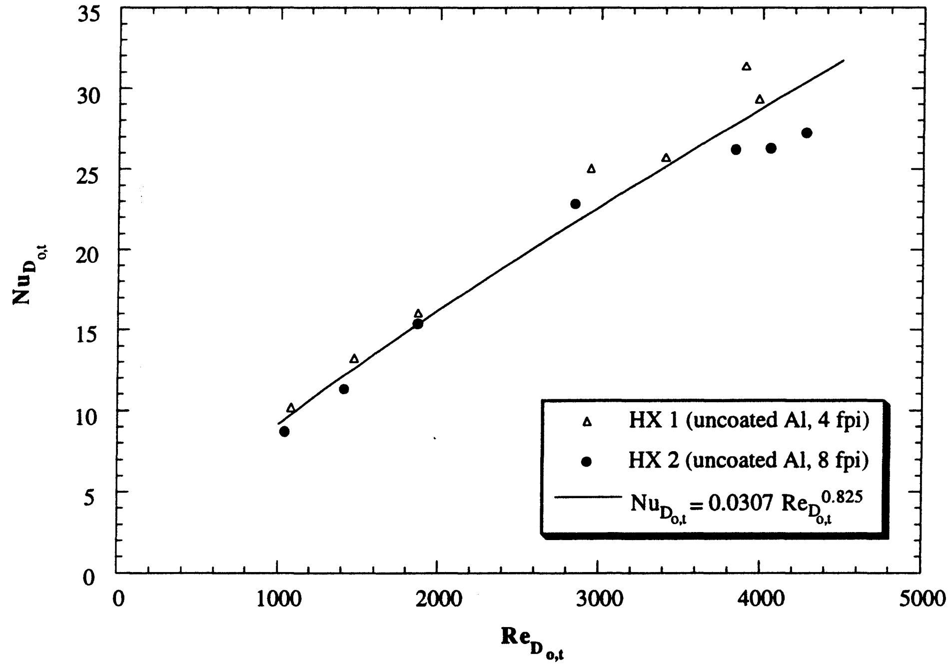

Figure 3.15 Dry air-side sensible heat transfer results with dry correlation

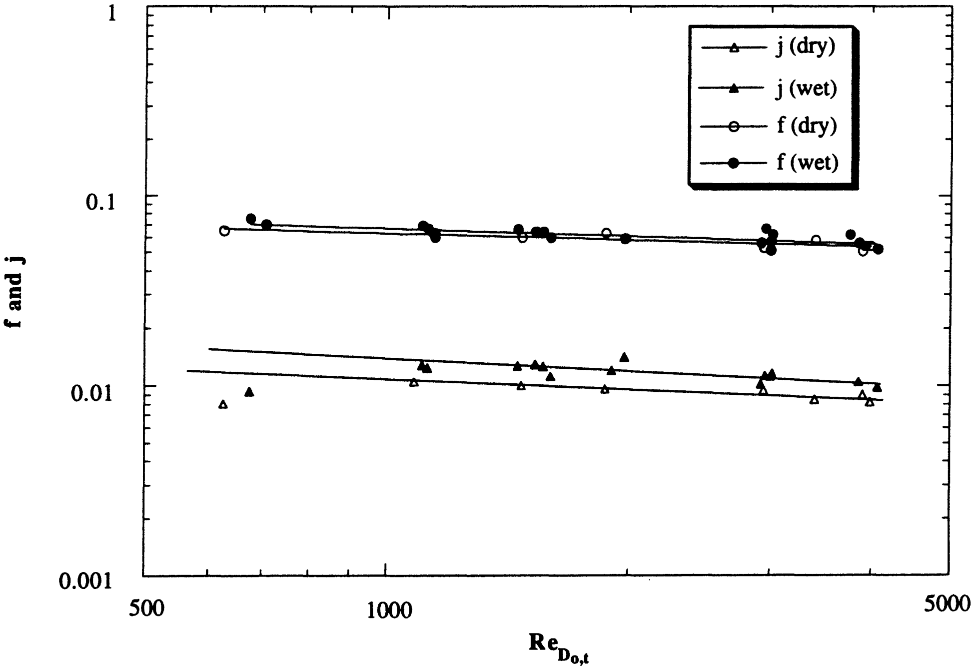

Figure 3.16 Sensible j and f for HX 1(uncoated Al, 4 fpi)

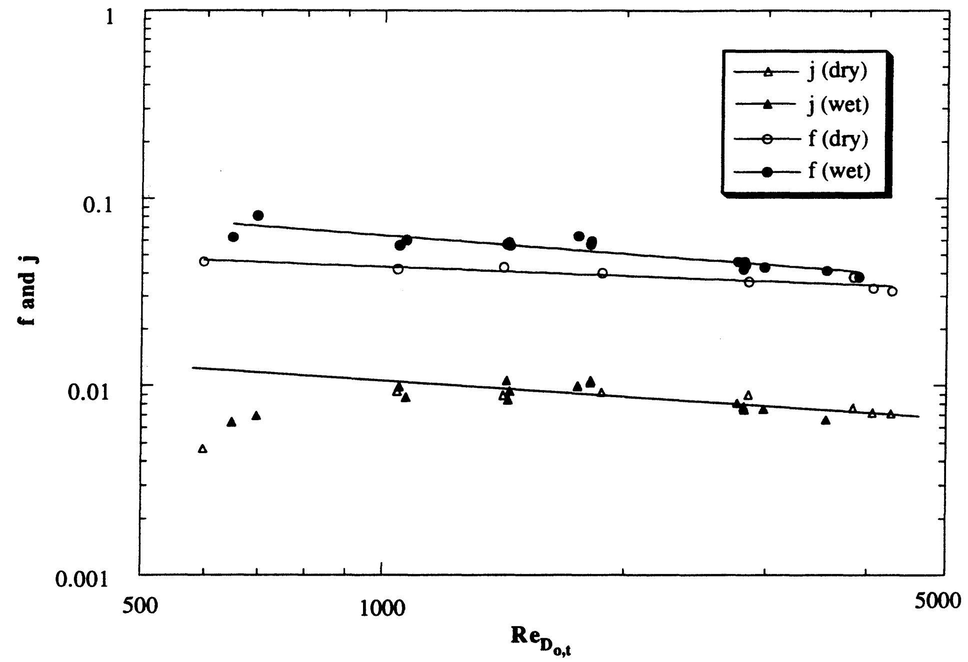

Figure 3.17 Sensible j and f for HX 2 (uncoated Al, 8 fpi)

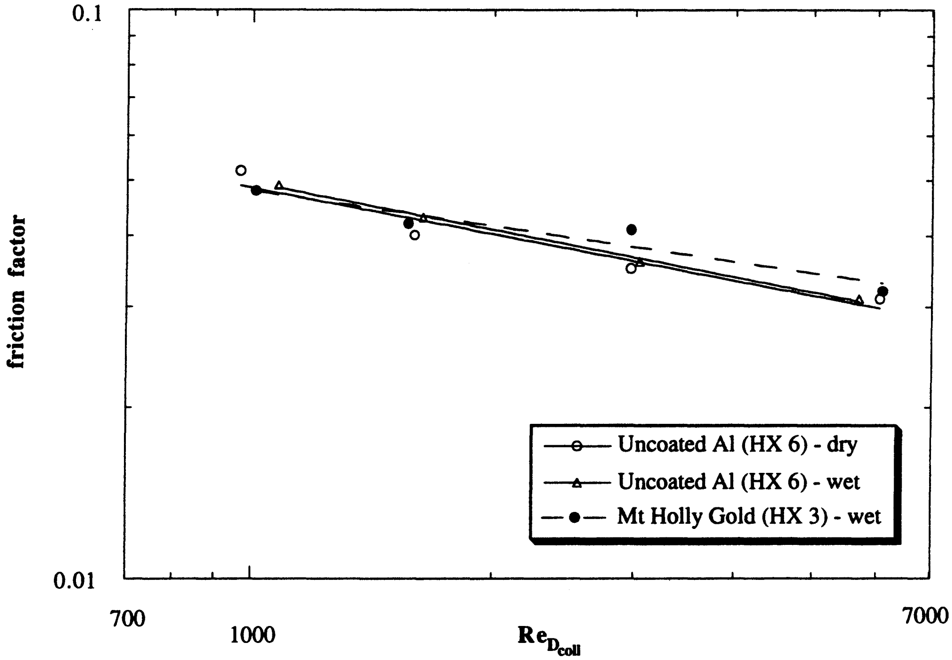

Figure 3.18 Friction factors for heat exchangers with 8 fpi, wet and dry

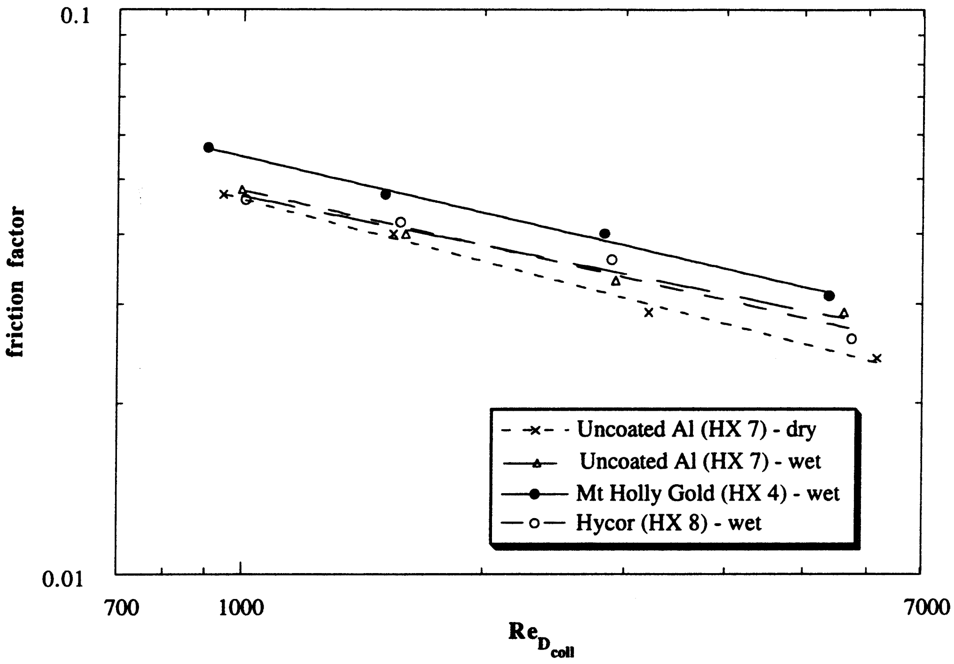

Figure 3.19 Friction factors for heat exchangers with 10 fpi, wet and dry

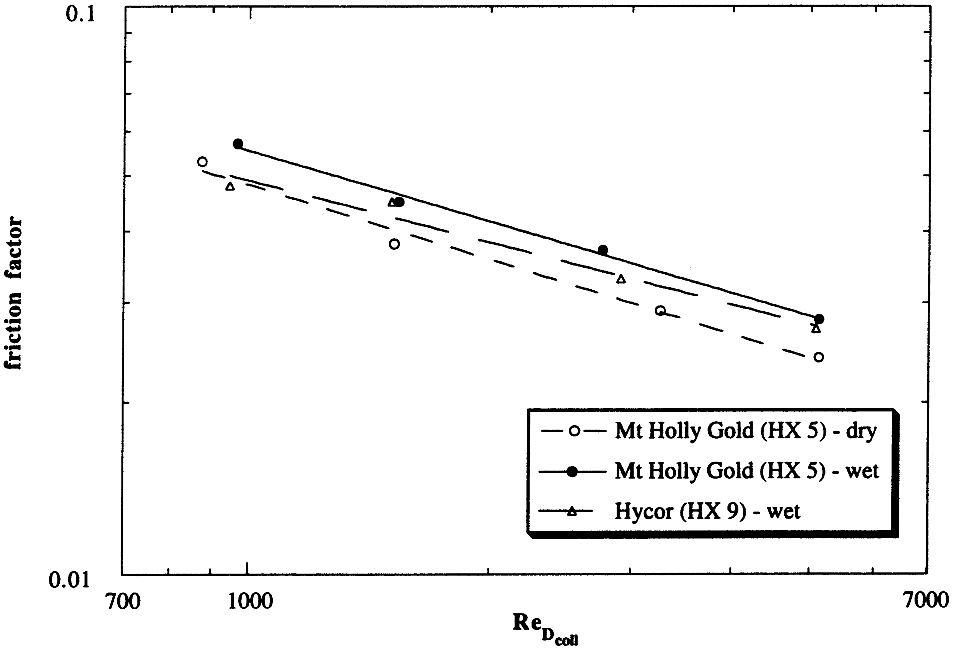

Figure 3.20 Friction factors for heat exchangers with 12 fpi, wet and dry

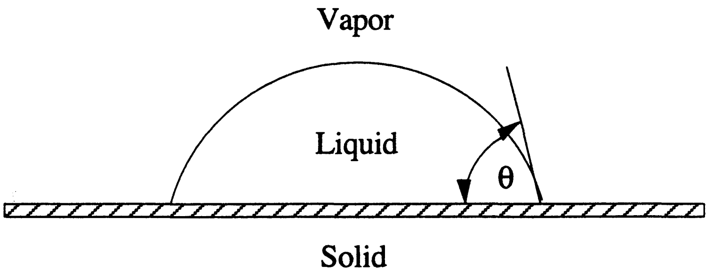

Figure 3.21 Contact angle of a liquid on a solid surface

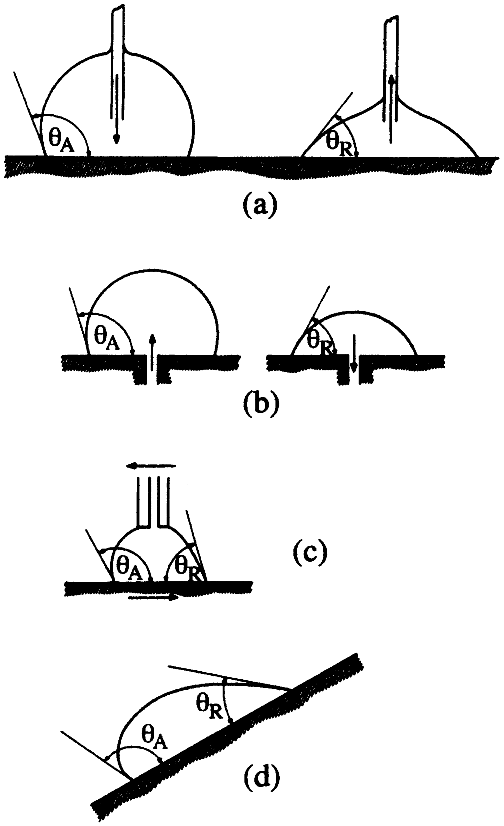

Figure 3.22 Techniques for measuring advancing and receding contact angles [31]

# Chapter 4 - Condensate Retention Modeling

Proposed techniques for modeling condensate retention are discussed in this chapter. Retained condensate geometries have been identified during experiments conducted under condensing conditions for plate-fin-tube heat exchangers. Analytical techniques have been developed for these geometries based on force balances between gravitational, air-flow, and surface-tension forces. These techniques have been used to explain condensate retention behavior and to develop a simple retention model for wide fin spacing. Direction for future retention modeling efforts has been provided and sources which may aid modeling have been cited.

## 4.1 Proposed Retention Modeling Procedure

The proposed retention modeling procedure is illustrated graphically in Figure 4.1. The quantity of retained condensate (mass of liquid water) is determined by calculating the volume of retained condensate and multiplying this volume by the density of the water. To determine the total volume of retained condensate, the retained geometries must be identified. The particular retained condensate geometries will relate to the heat exchanger geometry which must be simply characterized to make the model general. The maximum size of a particular geometry may be determined by considering the balance between gravitational, air-flow, and surface-tension forces. If the combined gravitational and air-flow forces exceed the surface-tension retaining force, the condensate geometry will be removed from the heat exchanger surface. In addition to the maximum size, the size distribution of geometries smaller than the maximum must be determined and the percentage of the total heat transfer area covered by the particular geometry. After determining the maximum size, the distribution, and the area covered by the various retained condensate geometries, the total volume and mass of the retained condensate may be determined.

## 4.2 Forces Acting on Retained Condensate

### 4.2.1 Surface Tension Forces

Surface tension provides the force necessary to retain condensate against the effects of gravitational and air-flow forces. Surface-tension forces may be characterized by the interfacial tension of the liquid, the advancing and receding contact angles, and the shape of the contact line between the liquid and solid. The surface tension of water is determined by the following relationship developed by Jasper [32]. The temperature is expressed in degrees Celsius and the relationship is applicable over the temperature range 10°C ≤ T ≤ 100°C.

$$\gamma(mN/m) = 75.83 - 0.1477\,T \qquad (4.1)$$

A temperature of 12°C was used to determine the surface tension for the modeling results presented in this chapter. The advancing and receding contact angles for the heat exchanger materials of this study were measured using a contact angle goniometer. These angles depend on the fin material, the surface finish and roughness, and contaminants on the surface.

### 4.2.2 Gravitational Forces

The effects of gravitational forces depend on the heat exchanger orientation and the air-flow direction. If the air flow is downward through the heat exchanger, the gravitational and air-flow forces are aligned and will act together to remove condensate from the surface. For other heat exchanger and flow orientations, condensate removal mechanisms will vary depending on whether air-flow or gravitational forces are dominant. For example, if the air flow is perpendicular to the gravitational force, condensate may drain by the gravitational force or be shed perpendicular to the direction of gravity by air-flow forces.

Gravitational forces are simple body forces which may be defined based on the volume of a retained condensate geometry and the density of the liquid. The volume may be difficult to define. Simple approximations of the shapes of retained condensate geometries are provided in this chapter and used to determine the gravitational force. There have been numerous studies on the ability of drops or bubbles to adhere to non-horizontal surfaces against gravitational forces [33] [34] [35] [36].

### 4.2.3 Air-Flow Forces

The air-flow forces include two components, the shear forces due to the fluid viscosity and the presence of a boundary layer and the pressure-drop forces created by the pressure differential over the surface of the body. These forces may be summed and used to define a drag coefficient as a function of the Reynolds number. From the drag coefficient, the local air velocity, the fluid properties, and the projected area of a retained condensate geometry, the air-flow force may be determined.

Several difficulties exist in defining the air-flow forces acting on retained condensate: drag coefficients are not readily available for the condensate geometries of interest, the shape of the retained condensate may be influenced by the air-flow and gravitational forces, and the local air velocity is difficult to determine. Air velocities vary throughout the heat exchanger because the flow area varies. In addition, the condensate will be located in either a developing or fully developed boundary layer which may be either laminar or turbulent.

A literature review was completed to identify possible sources for determining air-flow forces acting on retained condensate. There have been several studies on the influences of motion of the surrounding fluid on dislodging drops. Dussan [37] discussed the ability of drops with small advancing contact angles and contact angle hysteresis to adhere to solid surfaces in the presence of a weak shear flow. An equation was presented which relates the maximum rate of strain and experimentally measurable quantities to drop dislodging. This equation is applicable in the limit as the advancing contact angle and the contact angle hysteresis approach zero which are not valid for the heat transfer surfaces of this study. Durbin [38] [39] applied free-streamline theory to determine drop dislodging by wind pressure. This analysis is applicable at high Reynolds numbers if the drop height is large compared to approaching boundary layer thickness. The analysis considers potential flow with free-streamline separation around a deformable surface. The shape of the surface is determined by surface-tension forces. Plots of the critical Weber number for drop dislodging versus a parameter defined in terms of the advancing and receding contact angles were provided. This analysis may provide insights into air-flow forces acting on retained condensate.

An experimental study was conducted by Al-Hayes and Winterton [40] on bubbles detaching from a solid surface in flowing liquids. Drag coefficients were defined as a function of the bubble Reynolds number based on the bubble diameter for different surfaces which provided equilibrium contact angles between 22° and 90°. The bubble was approximated as a truncated sphere and the Reynolds number was based on the local velocity at half the distance the bubble projected from the surface. The following drag coefficients were determined from the experimental results:

$$C_d = 1.22 \quad \text{for } 20 < Re_b < 400 \tag{4.2}$$

$$C_d = 24/Re_b \quad \text{for } 4 < Re_b < 20 \tag{4.3}$$

These drag coefficients may be applied to droplets adhering to heat transfer surfaces typical to this study. The difficulty in applying these results lies in determining the velocity used to calculate the Reynolds number. In addition, Reynolds numbers based on the droplet diameter may exceed 400. It is not clear whether these results may be extrapolated.

## 4.3 Retained Condensate Geometries and Force Balances

Retained condensate geometries were identified and photographed during experimental studies under condensing conditions. Force balances have been developed for these geometries. These force balances may be used to determine the maximum size of a particular geometry which may then be incorporated into a retention model.

### 4.3.1 Droplets Adhering to an Inclined Surface

A major contribution to the total quantity of retained condensate is attributable to droplets adhering to the fin and tube surfaces, especially at wide fin spacings. Figure 4.2 shows a droplet adhering to a surface at an inclination angle of α. The surface-tension and gravitational forces have been identified. In the current analysis the contact line is assumed to be circular as shown in Figure 4.2. Typically, the fin will be oriented such that the surface is vertical. A vertical surface corresponds to an inclination angle of $\alpha = \pi/2$.

A force balance was performed in the x-direction on the droplet shown in Figure 4.2. The following assumptions were made which simplify the analysis:

- The contact line between the drop and the solid is circular.
- The droplet may be approximated as a truncated sphere meeting the solid at $\theta_M = (\theta_A+\theta_R)/2$. The volume of the droplet is thus given by:

$$\forall = \frac{\pi D^3}{24}\left(\frac{2-3\cos\theta_M+\cos^3\theta_M}{\sin^3\theta_M}\right) \tag{4.4}$$

- The contact angle varies linearly around the circumference of the drop and is given as follows:

$$\theta = \theta_A + (\theta_R-\theta_A)\frac{\Phi}{\pi} \quad \text{as} \quad \Phi:\ 0 \rightarrow \pi \tag{4.5}$$

The surface-tension force is the product of the surface tension and the differential length of the contact line. The projection of this force in the x-direction is given by:

$$dF_{s,x} = \gamma\cos\theta\cos(\pi-\Phi)dl \tag{4.6}$$

where

$$dl = \left(\frac{D}{2}\right)d\Phi$$

The surface tension force may be integrated around the circumference of the contact line as follows:

$$F_{s,x} = \gamma D\int_0^{\pi}\cos\left[\theta_A+(\theta_R-\theta_A)\left(\frac{\Phi}{\pi}\right)\right]\cos(\pi-\Phi)d\Phi \tag{4.7}$$

The solution to this integral is:

$$F_{s,x} = \frac{\gamma D}{2}\left[\frac{\sin\theta_R-\sin(\theta_A-\pi)}{\left(\frac{\theta_R-\theta_A}{\pi}\right)+1}+\frac{\sin\theta_R-\sin(\theta_A+\pi)}{\left(\frac{\theta_R-\theta_A}{\pi}\right)-1}\right] \tag{4.8}$$

The gravitational force is given by:

$$F_{g,x} = -\rho_l g \forall \sin\alpha \tag{4.9}$$

The air-flow force based on the projected area of the truncated sphere and an assumed drag coefficient is given as follows:

$$F_{d,x} = -C_d \frac{1}{2}\rho_a u^2 A_{pr} \tag{4.10}$$

where

$$A_{pr} = \frac{D^2\theta_M}{4} - \frac{D^2}{4}\cos\theta_M \sin\theta_M$$

The maximum diameter is determined by summing the forces in the x-direction. The maximum diameter, determined by Equation 4.11, represents the largest droplet that surface-tension forces can retain against air-flow and gravitational forces. Equation 4.11 may not be solved explicitly for the maximum diameter and must be solved iteratively.

$$F_{g,x} + F_{d,x} + F_{s,x} = 0 \tag{4.11}$$

Sugawara and Michiyoshi [41] performed a similar analysis for a two-dimensional laminae of the droplet and considered only gravitational and surface tension forces. Sugawara and Michiyoshi presented the following equation for the maximum drop diameter.

$$D_{\max} = \left[\left(\frac{\gamma}{\rho_l g \sin\alpha}\right)\left(\frac{16\sin^3\theta_M}{2\theta_M - \sin(2\theta_M)}\right)\sin\left(\frac{\theta_A - \theta_R}{2}\right)\right]^{½} \tag{4.12}$$

Figure 4.3 shows the maximum droplet diameter on a vertical surface predicted by Sugawara and Michiyoshi and the maximum droplet diameter based on Equation 4.11 with $F_{d,x} = 0$. The results of the above three-dimensional analysis are in good agreement with the results of Sugawara and Michiyoshi.

Equation 4.11 can be used to predict the maximum drop diameter which can be retained on a heat exchanger surface as a function of the contact angles, the local air velocity, the drag coefficient, and the fluid properties. This maximum drop diameter can be coupled with a drop size distribution and an area coverage to determine the quantity of retained condensate associated with droplets on the heat exchanger surfaces.

The above analysis is applicable when the air-flow direction is aligned with the x-component of the gravitational force. Similar force balances may be developed for other air-flow directions. For other air-flow directions, the gravitational force will remain unchanged while the drag force will be imposed in the air-flow direction. The surface-tension force will always act to oppose motion and the droplet can be assumed to take on a shape that will maximize the surface-tension force.

### 4.3.2 Condensate Bridging between Adjacent Fins at Fin-Tube Junctions

Condensate was observed to accumulate as bridges between adjacent fins at fin-tube junctions during condensate retention experiments for fin spacings less than 4 fpi. At 4 fpi this type of condensate retention was not observed. The condensate accumulated in the region downstream of the tube as shown in Figure 4.4. If the flow separates as it passes the tube, the condensate is accumulating in a wake region. The low local air velocity in this wake region may allow a significant portion of the total retained condensate to accumulate in these regions. Force balances are presented for condensate retained as bridges in these regions.

Force balances were developed for the geometry illustrated in Figure 4.5. The analysis is similar to the analysis in the preceding section. The air-flow forces have been neglected. It is difficult to determine the air force acting on this condensate geometry, because it is located immediately downstream of a tube. These forces may decrease with increasing air-flow rate as the tube wake region grows in size. In addition, the air flow may begin to bypass this region of the heat exchanger at high air-flow rates and travel through paths unobstructed by the tubes.

Neglecting air-flow forces, the maximum size of this condensate geometry may be determined by a balance between surface tension and gravitational forces. The surface tension forces in the x-direction are determined as follows:

$$F_{s1} = 2\gamma l \cos(\pi - \theta_A) \tag{4.13}$$

$$F_{s2} = 2\gamma f_s \cos\theta_R \tag{4.14}$$

The gravitational force in the x-direction is:

$$F_{g,x} = -\rho_l g \mathcal{V} \tag{4.15}$$

The volume of the fin-tube bridge may be determined from the geometry of Figure 4.5.

$$\mathcal{V} = L_{\max}(l \cdot f_s) - A_1 \cdot f_s + A_2 \cdot l \tag{4.16}$$

where

$$A_1 = \left(\pi R_1^2\right)\left(\frac{\pi/2 - \theta_R}{\pi}\right) - \frac{l}{2}\left[R_1^2 - \left(\frac{l}{2}\right)^2\right]^{1/2}$$

$$A_2 = \left(\pi R_2^2\right)\left(\frac{\theta_A - \pi/2}{\pi}\right) - \frac{f_s}{2}\left[R_2^2 - \left(\frac{f_s}{2}\right)^2\right]^{1/2} \quad \text{if } \theta_A > \pi/2$$

$$A_2 = \left(\pi R_2^2\right)\left(\frac{\theta_A - \pi/2}{\pi}\right) + \frac{f_s}{2}\left[R_2^2 - \left(\frac{f_s}{2}\right)^2\right]^{1/2} \quad \text{if } \theta_A < \pi/2$$

and

$$R_1 = \frac{D_{o,t}}{2}$$

$$R_2 = \frac{f_s}{2\sin(\theta_A - \pi/2)}$$

Combining Equations 4.13 through 4.16 to form a force balance in the x-direction and solving for $L_{max}$ yields the following expression:

$$L_{\max} = \frac{2\gamma f_s \cos\theta_R + 2\gamma l \cos(\pi - \theta_A) + \rho_l g A_1 f_s - \rho_l g l A_2}{\rho_l g l f_s} \qquad (4.17)$$

The quantity of retained condensate associated with fin-tube bridges can be determined by calculating $L_{max}$ and assuming a distribution of bridges smaller than this size.

### 4.3.3 Other Condensate Geometries

Other condensate geometries were observed during retention experiments. At the widest fin spacing, 4 fpi, condensate was not observed to bridge the fins at a fin-tube junction. Instead, condensate was retained as fillets as shown in Figure 4.6. A mixture of bridges and fillets were observed for fin spacing less than 4 fpi with bridging more prevalent as the fin spacing decreased. As the wettability increases, the fillet meets the fin at a much smaller contact angle as shown in Figure 4.6 (b). A change in the mode of condensation on the tubes was also apparent as the wettability increased and is shown in Figure 4.6 (b). The wettability increased with wet-dry cycling and the condensate formed as a film on the tubes rather than as distinct droplets.

Two condensate retention geometries were observed at the fin tips as illustrated in Figure 4.7. At 4 fpi condensate was not observed to bridge adjacent fins at the fin tips; rather, condensate was retained as pendant shaped droplets clinging to the fins. For fin spacings of 8 fpi and less, condensate was retained as bridges between the adjacent fins at the fin tips as well as being retained as pendant shaped droplets at the fin tips.

Similar force balances may be performed for these geometries. These derivations have not been included in this report. The majority of the retained condensate is assumed to be associated with droplets on the heat exchanger surfaces and bridges retained at fin-tube junctions. Retention modeling efforts have only included these geometries.

## 4.4 Retained Condensate Size Distribution

The analytical techniques above may be used to predict the maximum size of retained condensate geometries. The quantity of retained condensate can be determined if the size distribution of retained condensate geometries smaller than the maximum size and the area covered by the particular geometry are known. These distributions are difficult to determine experimentally, because it is difficult to see between heat exchanger fins.

Drop size distributions have been determined for dropwise condensation on various surfaces, because this distribution is needed to predict heat transfer rates for dropwise condensation. Graham [42] determined drop size distributions for dropwise condensation on a vertical mirror-smooth copper surface at atmospheric pressure. The number of drops per unit area was determined to vary as $D^{-1.73}$ for drop diameters between 10 and 500 micrometers and $D^{-2.8}$ for drop diameters between 500 and 2500 micrometers. These drop distributions were determined by counting drops of size $D \pm 0.2D$. Drops larger than 10 micrometers were reported to cover 82% of the total surface area. Drop distributions obtained during studies such as this may provide estimates for retention modeling. These distributions may be affected by water shedding mechanisms which may be significantly different in a full scale heat exchanger.

## 4.5 Higher Order Effects

Various effects complicate condensate retention modeling and need to be investigated to refine current retention modeling techniques. Higher order effects will complicate drop distributions and the area covered by droplets for a full scale heat exchanger when compared to results for dropwise condensation on a single vertical surface.

Several condensate removal mechanisms were discussed in Chapter 3 in an attempt to explain differences in condensate retention trends. Different condensate removal mechanisms may result in different distributions in the size of retained condensate geometries and the area covered by the condensate. Depending on the fin spacing, condensate on a fin surface may be removed by condensate moving down the adjacent fin surface. Condensate may also be removed by condensate shed from the tubes. These tube-fin and fin-fin interactions will reduce the area covered by droplets on the surface when compared to the area covered for dropwise condensation on a single vertical surface.

Drop distributions for studies such as the one conducted by Graham are performed without air flow. Air-flow forces on retained droplets will vary with drop size for a given air mass flow rate. Assuming a constant drag coefficient as given by Equation 4.2, the air-flow force will increase with drop size because the projected area of the droplet increases and the velocity at half the distance the droplet projects from the surface increases assuming the drop is located within a boundary layer. It is not clear how air-flow forces effect condensate distributions and the area covered by condensate.

The length of the heat exchanger may further influence drop size distributions and the area covered by droplets when compared to distributions determined from studies such as those performed by Graham. Graham determined drop size distributions and the area covered by the droplets for a round condensing surface with a diameter of 20 mm. The heat exchangers fins used in this study were approximately 26.7 cm long in the vertical direction (See Figures 2.4 and 2.5). Condensate distributions and the area covered by condensate along the length of the heat exchanger fins will vary. Condensate distributions and the area covered by condensate can by expected to be similar to the distribution measured by Graham only near the leading edge of the heat exchanger. Condensate retained on other portions of the heat exchanger may be swept by condensate departing from upstream portions of the heat exchanger. This sweeping will influence the area covered and possibly the drop size distributions. Figure 4.8 illustrates the variation in area covered by condensate along the length of the heat exchanger. The fraction of the fin area covered by condensate decreases from row to row in the flow direction which was downward through the heat exchanger. By the thirteenth row, the area covered by retained condensate has decreased significantly when compared to the area of the fin covered near the second tube row.

The higher order effects discussed will tend to decrease the area covered by condensate when compared to studies on a single vertical surface. These effects may also influence drop size distributions. Applying drop size distributions and the area covered for dropwise condensation on vertical surfaces should result in overpredicting the quantity of retained condensate.

## 4.6 Condensate Retention Model for Wide Fin Spacings

A condensate retention model for wide fin spacings has been developed and is presented to demonstrate potential condensate retention modeling procedures. The following assumptions limit the applicability of this model to heat exchangers with fin spacings at least twice the height of the largest droplets.

- droplet distributions on the fin surfaces are not effected by droplets on the adjacent fin surface
- bridges do not form between fins at fin-tube junctions, condensate is retained in these regions as fillets which do not significantly influence the quantity of retained condensate

### 4.6.1 Modeling Techniques

The model was developed assuming that droplets on the heat transfer surface are the only significant geometry contributing to the total quantity of retained condensate. The drop distributions were determined based on Graham's results [42]. Graham observed a discontinuity in the drop distribution at a drop diameter of 500 micrometers. The maximum drop diameter counted was 2500 micrometers. Graham explained this discontinuity by claiming that drop distributions for drops greater than 500 micrometers in diameter were influenced by departure mechanisms while drop distributions for drops less than 500 micrometers in diameter were influenced primarily by coalescence of droplets. Assuming this discontinuity to occur at the same location for the current study was not merited because of the much larger droplets identified during this study. Instead, the discontinuity was assumed to occur at the same $D/D_{max}$. The drop distributions were assumed to be of the same form as the distributions determined by Graham:

$$\Delta N = B_1 D^{-1.73} \qquad \text{for } 10\mu\text{m} < \text{D} < 0.2\text{D}_{max} \qquad (4.18)$$

$$\Delta N = B_2 D^{-2.8} \qquad \text{for } 0.2\text{D}_{max} < \text{D} < \text{D}_{max} \qquad (4.19)$$

where

$\Delta N$ = # of drops of diameter D±0.2D per cm$^2$

In order to define the drop distributions, the coefficients $B_1$ and $B_2$ must be determined. These coefficients were calculated by assuming that 82% of the total heat transfer area was covered by drops with diameters greater than 10 micrometers and that 36% of the area was covered by drops with diameters greater than $0.2D_{max}$. The percentage of area covered by droplets greater than 10 micrometers was based on Graham's results because drop sizes down to 10 micrometers could not be resolved based on photographs taken during the experiments. The percentage of the area covered by droplets greater than $0.2D_{max}$ was determined from Figure 4.8 (a).

The maximum drop size was determined using equations presented in Section 4.3.1. Only the Brazeway heat exchanger with 4 fpi had fin spacing wide enough for the current modeling techniques to be applicable. The contact angle for the fin surfaces of this heat exchanger varied over the course of the experiments as discussed in Section 3.1.2 B. The contact angles for the new fin material and the values for the fin material after the experimental study were used in determining the maximum droplet diameter.

The results of Al-Hayes and Winterton [40] were used to determine the air-flow force acting on the droplets. The drag coefficient was assumed to be 1.22. The Reynolds number based on the droplet diameter was between 49 and 972. The constant drag coefficient of 1.22 was reported for Reynolds numbers based on bubble diameter between 20 and 400. These results have been extrapolated to higher Reynolds numbers. It is difficult to define appropriate velocities for determining the air-flow force. The drag coefficients presented by Al-Hayes and Winterton were determined based on the local velocity at half the distance the bubble projected from the wall. This velocity was determined by laminar or turbulent boundary layer approximations depending on the flow regime. The flow regime through the heat exchanger may vary with Reynolds number. At low Reynolds numbers the flow may be fully developed and laminar. At slightly higher Reynolds numbers the flow may still be laminar but developing. At the highest Reynolds numbers the flow is most likely turbulent and may either be developing or fully developed. Further complications include air-flow maldistributions throughout the heat exchanger and velocity fluctuations do to area changes through heat exchanger passages.

The velocity at half the distance the drop projected from the wall was calculated based on a second order polynomial approximation to the boundary layer velocity profile. The boundary layer thickness was determined from the Blasius solution for flow over a flat plate with zero pressure gradient. The boundary layer thickness was calculated at a distance along the plate equal to half the fin length in the flow direction. The freestream velocity was assumed to be the velocity based on the minimum free flow area of the heat exchanger. The droplet was assumed to be a truncated sphere meeting the surface at angle $\theta_m$. The distance that the droplet protrudes from the wall (the height of the droplet) may be determined by Equation 4.20.

$$h_d = \frac{D}{2} - \frac{D}{2}\cos\theta_m \tag{4.20}$$

These approximations are very crude and have been applied primarily to illustrate modeling techniques. Further refinements are required to accurately determine the velocity and air-flow forces used to calculate the maximum drop size. After determining the air-flow force, the maximum drop size was calculated by Equation 4.11.

The maximum drop diameters for velocities less than 3 m/s based on the minimum free flow area of the heat exchanger were 4.27 mm for $\theta_m = 72.7°$ and 5.2 mm for $\theta_m = 58.5°$. Figure 4.9 shows the maximum drop size observed at $V_{max} = 2.1$ m/s. The droplet diameter falls within the limits predicted by Equation 4.11.

The quantity of retained condensate may be determined by the percent of the total heat transfer area covered, the maximum drop size, the drop volumes, and the drop size distributions. The drops were assumed to have circular contact areas and the volumes of the drops were calculated using Equation 4.4. The drop distributions for the tubes are assumed to be the same as for the fins and the tube area is included in determining the area covered by condensate. The total retained condensate was calculated using equation 4.21.

$$m_{cond} = \left( \sum_{D=10\mu m}^{D=D_{max}} \Delta N_D \mathcal{V}_D \rho_l \right) A_{covered} \tag{4.21}$$

### 4.6.2 Retention Modeling Results

The quantity of retained condensate determined by the model is compared to the experimentally measured condensate retention in Figure 4.10. The model tends to overpredict the quantity of retained condensate especially at high air-flow rates. This overprediction is expected because 82% of the heat transfer area is assumed to be covered by droplets greater than 10 micrometers. This percentage may be valid for the first few tube rows, but the percentage of the heat transfer area covered by condensate decreases significantly along the length of the fin (See Figure 4.8). The air-flow rate appears to have a more significant influence on the condensate retention than predicted by the model. The techniques used to determine the air-flow forces may need to be refined to predict this behavior. The laminar boundary layer profile is probably a poor assumption at high air-flow rates. The model predicts that velocities less than 3.5 m/s based on the minimum free flow area do not effect the quantity of retained condensate. The air-flow force below 3.5 m/s is predicted by the model to be much smaller than the gravitational and surface-tension forces.

The two predicted curves in Figure 4.10 represent the surface wettability conditions before and after testing for HX 1 (See Section 3.3.4). The average measured contact angles for the new fin material were $\theta_A = 92.3°$ and $\theta_R = 53.0°$ which give $\theta_M = 72.7°$. After testing, the contact angles were measured for fin material removed from the heat exchanger. These measurements indicated an increase in wettability due to wet-dry cycling. The average contact angles after testing were $\theta_A = 81.9°$ and $\theta_R = 35.1°$ which give $\theta_M = 58.5°$. The quantity of retained condensate was observed to decrease with an increase in wettability for HX 1 (See Table 3.1). A similar decrease in retained condensate was predicted by the model.

The percentage of the total retained condensate associated with droplets smaller than $D/D_{max}$ is illustrated by Figure 4.11 as predicted by the model. This relationship is independent of the surface wettability for the cases corresponding to $\theta_M = 72.7°$ and $\theta_M = 58.5°$. The largest drops are predicted to be the most influential in determining the quantity of retained condensate. Drops less than 10 micrometers in diameter have been considered to be negligible in terms of the total condensate retention. Figure 4.11 indicates that this assumption is valid. Based on the drop distribution assumed in this analysis, drops with $D/D_{max}$ less than 0.1 account for approximately 10% of the total condensate.

## 4.7 Maximum Condensate Retained as Bridges at Fin-Tube Junctions

The maximum quantity of condensate which may be retained as bridges between adjacent fins at fin-tube junctions was calculated based on the techniques outlined in Section 4.3.2 and assuming no air-flow forces. The average advancing and receding contact angles from Tables 3.4 and 3.5 were used in the calculation. All of the fin-tube regions downstream of the tubes were assumed to be flooded with condensate bridges of length $L_{max}$ determined by Equation 4.17. The dogbones in the fins on the Brazeway heat exchanger result in half the number of these fin-tube regions than for a similar heat exchanger with solid fins. There is no fin material in the region downstream of the tube at the fin-tube junction for the odd numbered tube rows. Table 4.1 presents the predicted maximum quantity of condensate retained as fin-tube bridges and the length of these bridges (See Figure 4.5).

A significant portion of the total retained condensate may be retained as bridges at fin-tube junctions for fin spacings less than 4 fpi. Table 4.1 should overestimate the quantity of condensate retained as fin-tube bridges because all of the regions will not be flooded with bridges of length $L_{max}$. The values for $L_{max}$ listed in Table 4.1 are significantly less than those observed during the experiments. In addition, the derivation of Section 4.3.2 indicates that fin-tube bridges will not form for the hydrophilic surface tested, HX's 8 and 9. Fin-tube bridges were observed for these specimens during retention experiments. Some aspect of the physics must not be reflected in the derivation of Section 4.3.2.

### 4.8 Summary

An initial model has been developed to predict the quantity of retained condensate for plate-fin-tube heat exchangers with wide fin spacings. This model incorporates measured advancing and receding contact angles which are used to determine surface-tension retaining forces. Air-flow forces have been included by assuming a constant drag coefficient and approximating the local velocity. This approach is very basic and is provided to illustrate modeling techniques. For heat exchangers with wide fin spacings the retained condensate has been assumed to be composed primarily of droplets adhering to the fin and tube surfaces. The maximum droplet size is calculated assuming the droplets to have circular contact lines and calculating the volume assuming the droplets to be truncated spheres meeting the solid at the average of the advancing and receding contact angles. The number of drops with diameters less than the maximum diameter were calculated based on drop size distributions experimentally determined by Graham [42] for dropwise condensation on a vertical surface.

Initial modeling techniques have been relatively successful in predicting the quantity of retained condensate at low air-flow rates for the Brazeway uncoated aluminum heat exchanger with 4 fpi (HX 1) while slightly overpredicting the condensate retention at high air-flow rates. The quantity of retained condensate was observed to decrease as the wettability increased for HX 1 and this trend was reflected by the model. HX 1 was the only heat exchanger tested for which the assumptions of the above modeling techniques were applicable. Further model validation and refinement requires additional condensate retention experiments for heat exchangers with wide fin spacings. Additional experiments should include a variety of hydrophilic and hydrophobic surface coatings providing various advancing and receding contact angles. In addition, various fin lengths should be included and the heat exchanger orientation and air-flow direction should be varied.

Force balances performed on bridges retained at fin-tube junctions indicate that these geometries may significantly contribute to the total quantity of retained condensate. The quantity of condensate retained as fin-tube bridges may increase with increasing air-flow rates as the wake regions of the tubes become larger. This effect may explain the increase in total retained condensate observed with increasing air-flow rates during the second set of condensate retention experiments.

Table 4.1 Predicted condensate retention as fin-tube bridges in region downstream of a tube

| HX | Manufacturer | fpi | Material | Surface Coating | $\theta_A$ | $\theta_R$ | $L_{max}$ (mm) | mass (g) |
|---|---|---|---|---|---|---|---|---|
| 2 | Brazeway | 8 | Al | none | 92.3° | 53° | 2.6 | 34.7 |
| 3 | HeatCraft | 8 | Al | Mount Holly Gold | 87.3° | 51.4° | 2.1 | 52.1 |
| 4 | HeatCraft | 10 | Al | Mount Holly Gold | 87.3° | 51.4° | 2.0 | 49.2 |
| 5 | HeatCraft | 12 | Al | Mount Holly Gold | 87.3° | 51.4° | 1.9 | 45.9 |
| 6 | HeatCraft | 8 | Al | none | 80.5° | 34.4° | 2.3 | 36.9 |
| 7 | HeatCraft | 10 | Al | none | 80.5° | 34.4° | 2.0 | 23.5 |

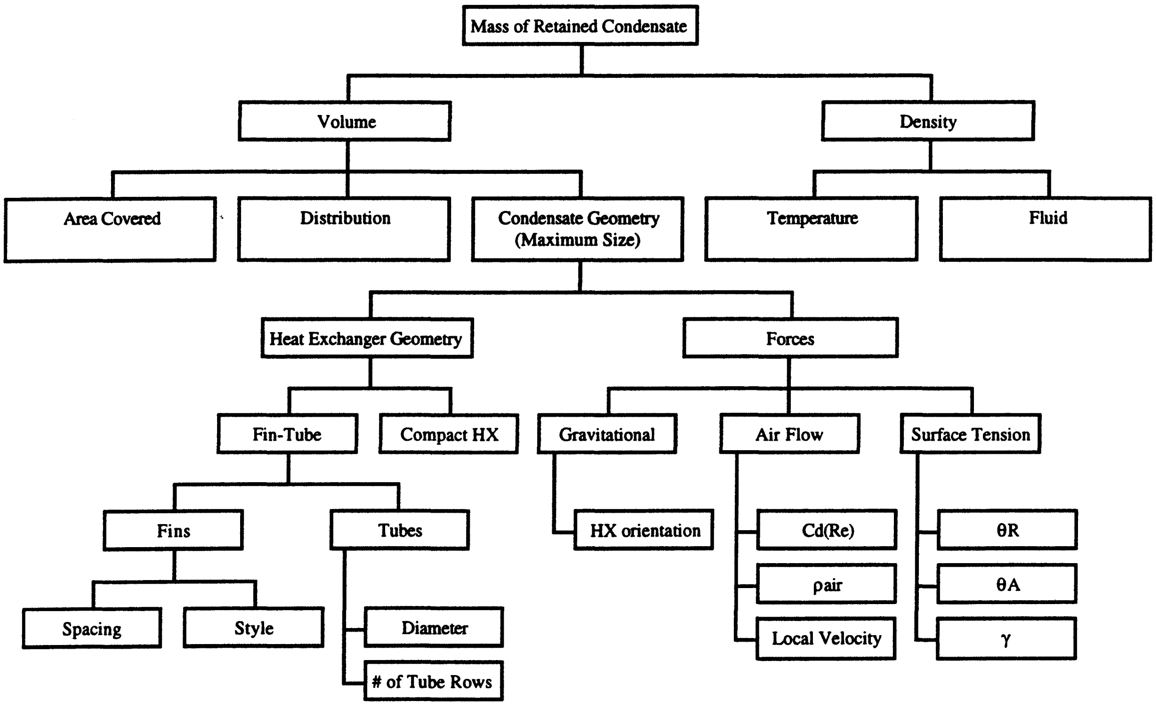

Figure 4.1 Proposed retention modeling technique

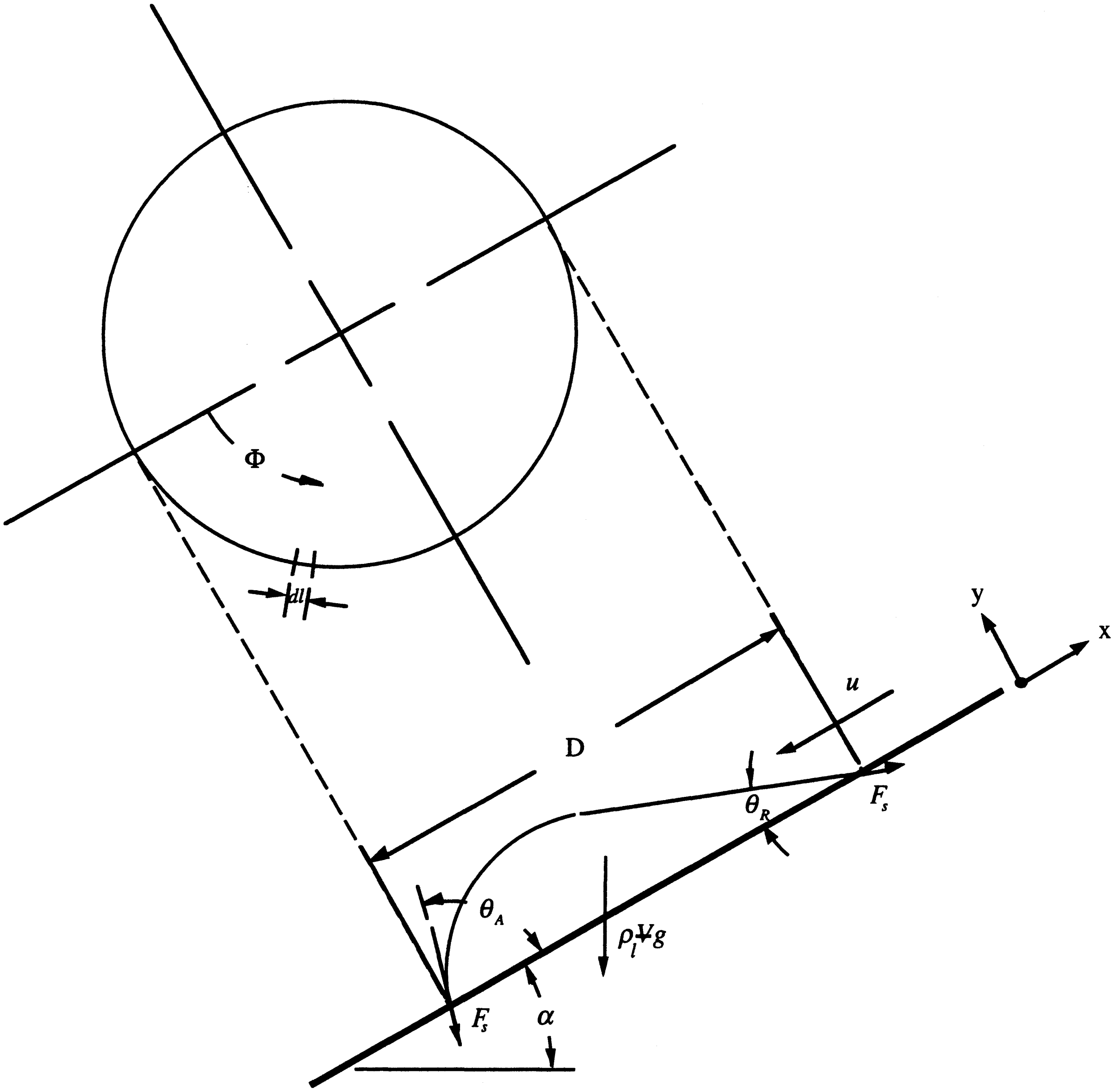

Figure 4.2 Droplet with a circular contact line on an inclined surface

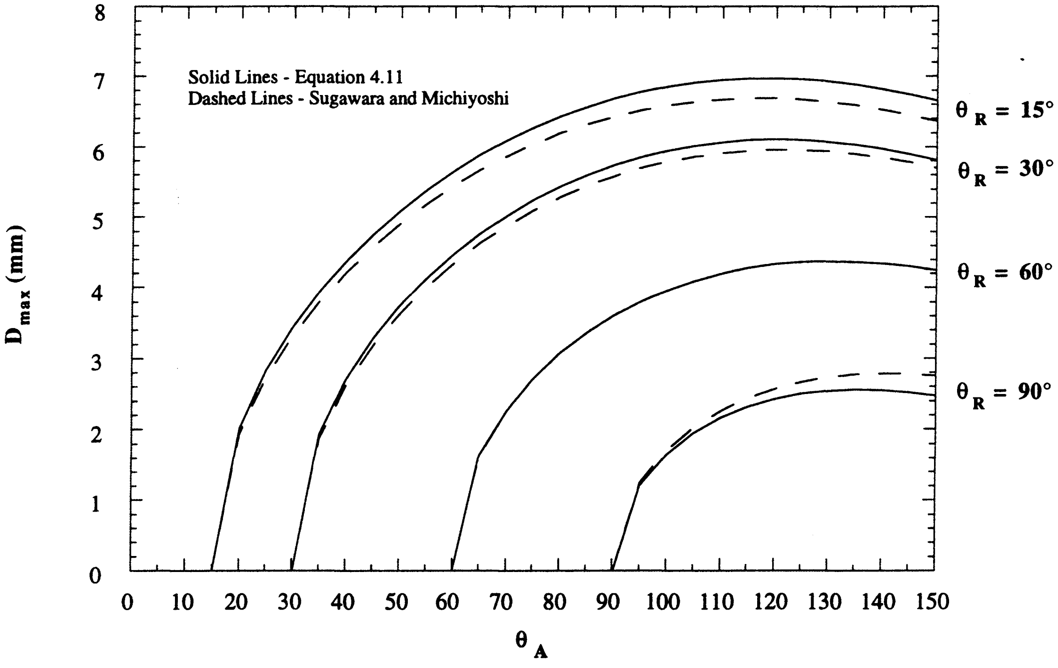

Figure 4.3 Maximum droplet diameter on a vertical surface without air flow

$\alpha = 90°$, $\gamma = 72.1$ mN/m, $\rho_l = 997.9$ kg/m$^3$

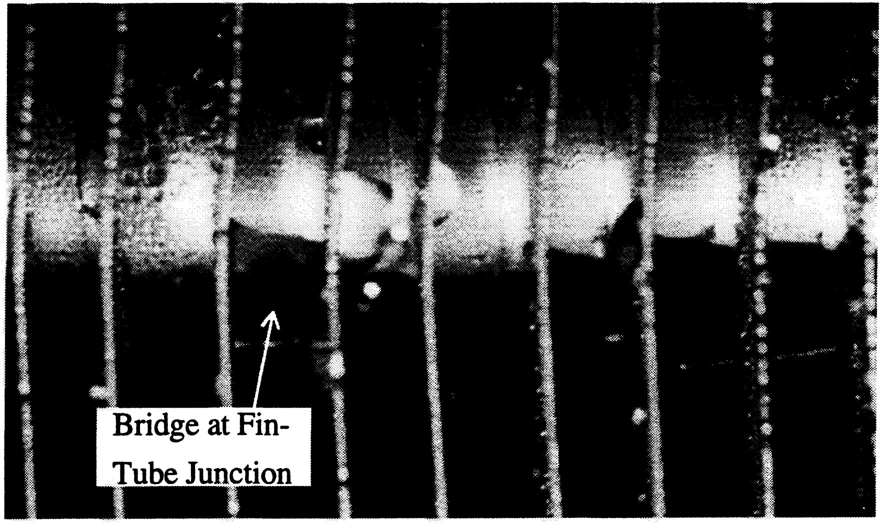

Figure 4.4 Bridges retained at fin-tube junctions, 8 fpi HX - uncoated

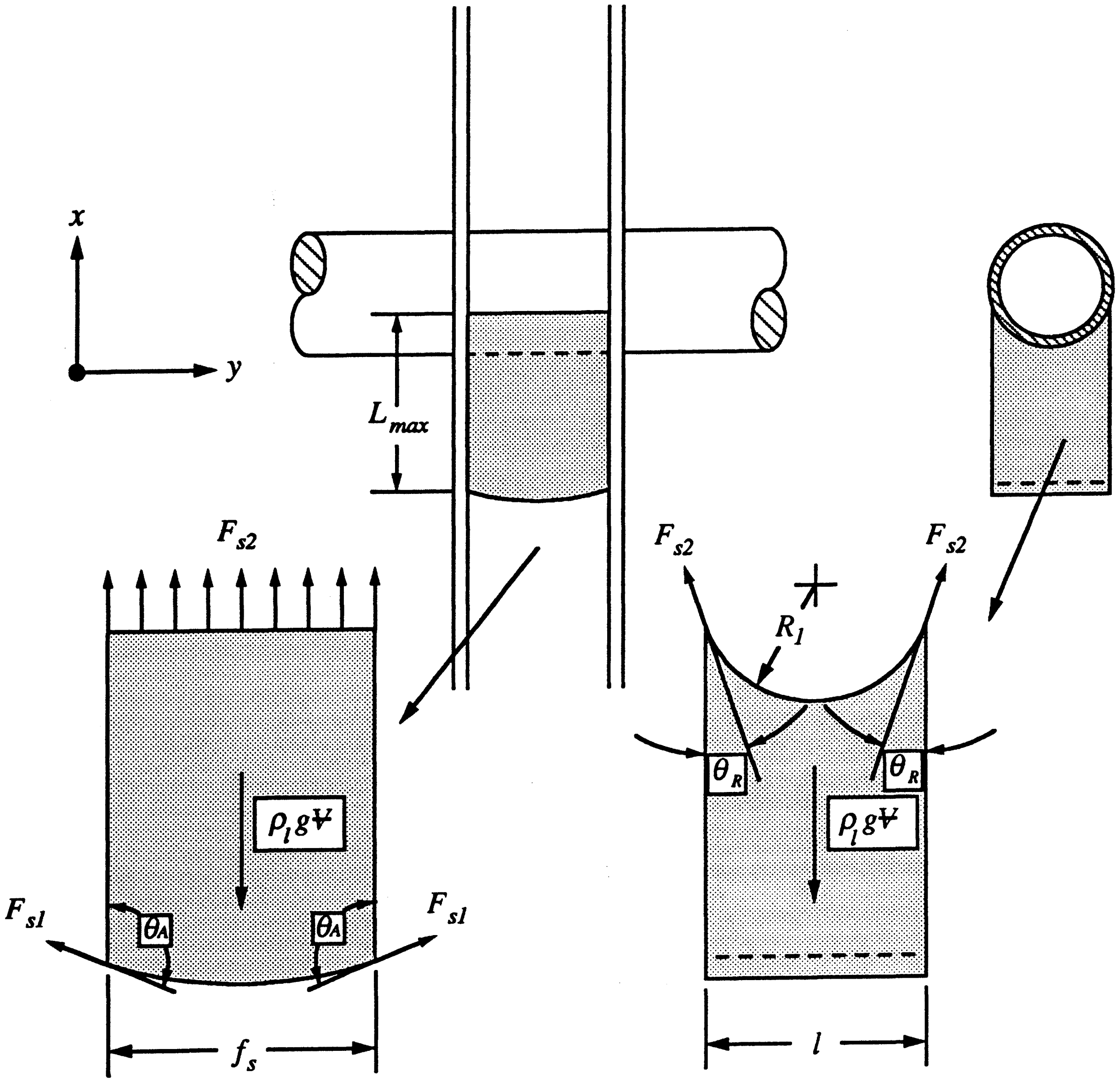

Figure 4.5 Forces acting on bridges retained between fins at fin-tube junctions

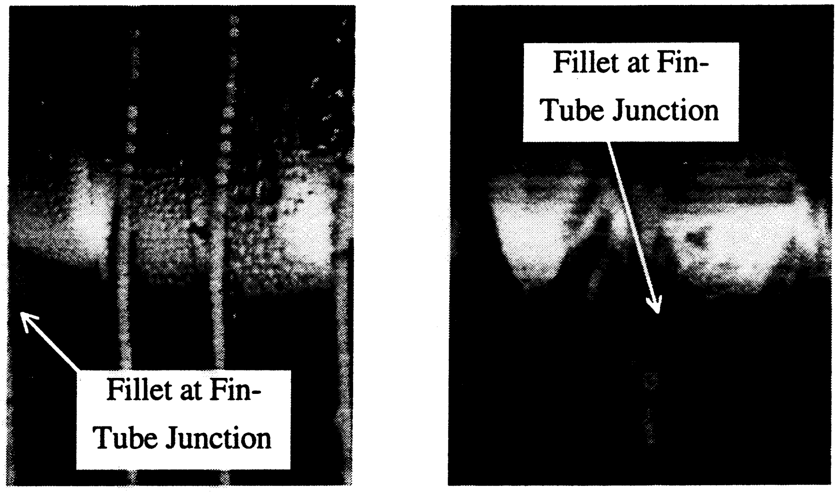

(a) (b)

Figure 4.6 Condensate fillets retained at a fin tube junction
(a) nonwetting condition (b) wetting condition

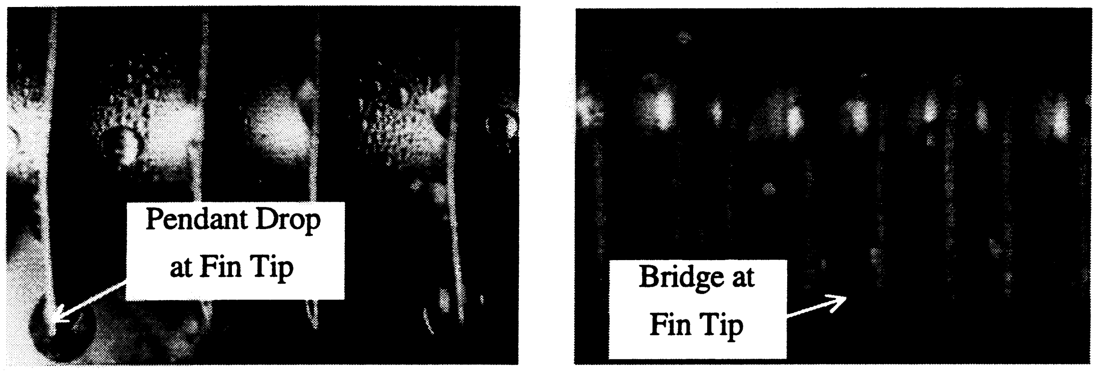

(a) (b)

Figure 4.7 Condensate retained at fin tips
(a) pendant drop - 4 fpi HX (b) bridge between adjacent fins - 8 fpi HX

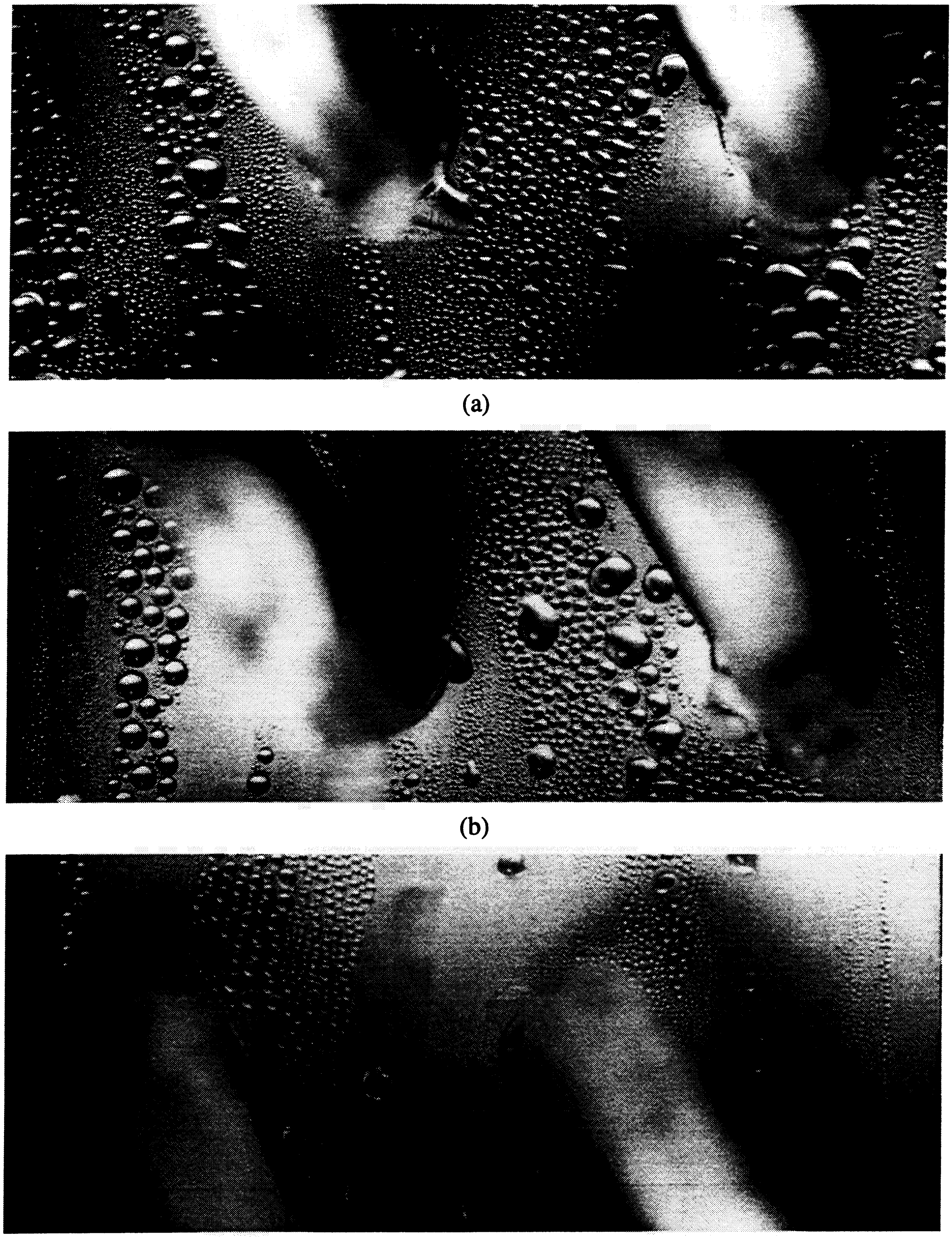

(a)

(b)

(c)

Figure 4.8 Dropwise condensation on uncoated aluminum fin surface
(a) 2nd tube row (b) 6th tube row (c) 13th tube row

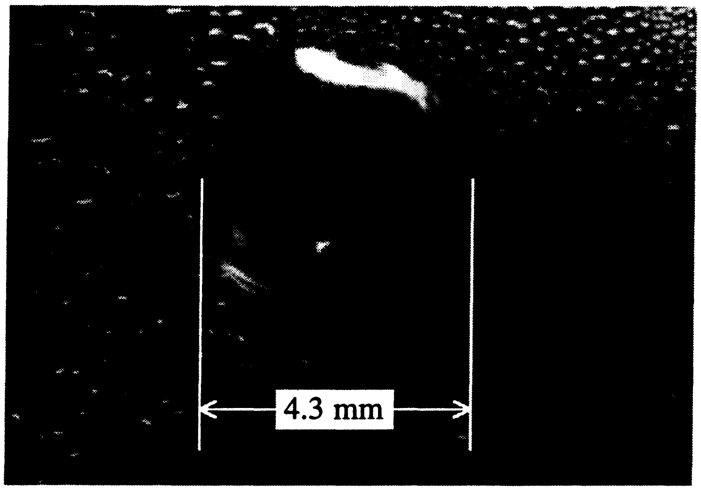

Figure 4.9 Large drop retained on bare aluminum fin surface

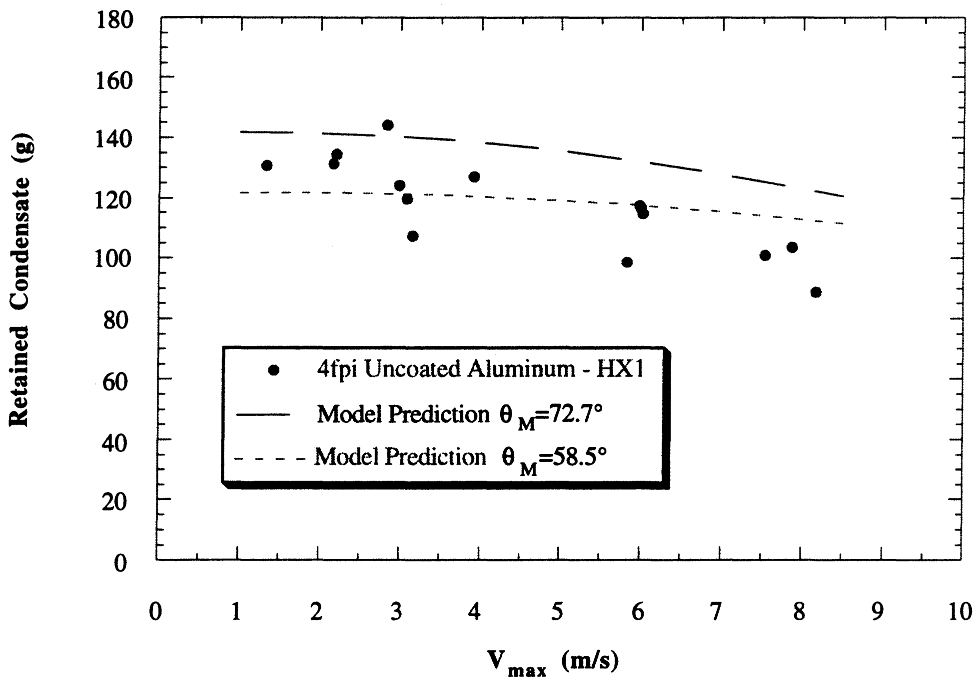

Figure 4.10 Condensate retention model predictions with measured quantity of retained condensate for HX 1

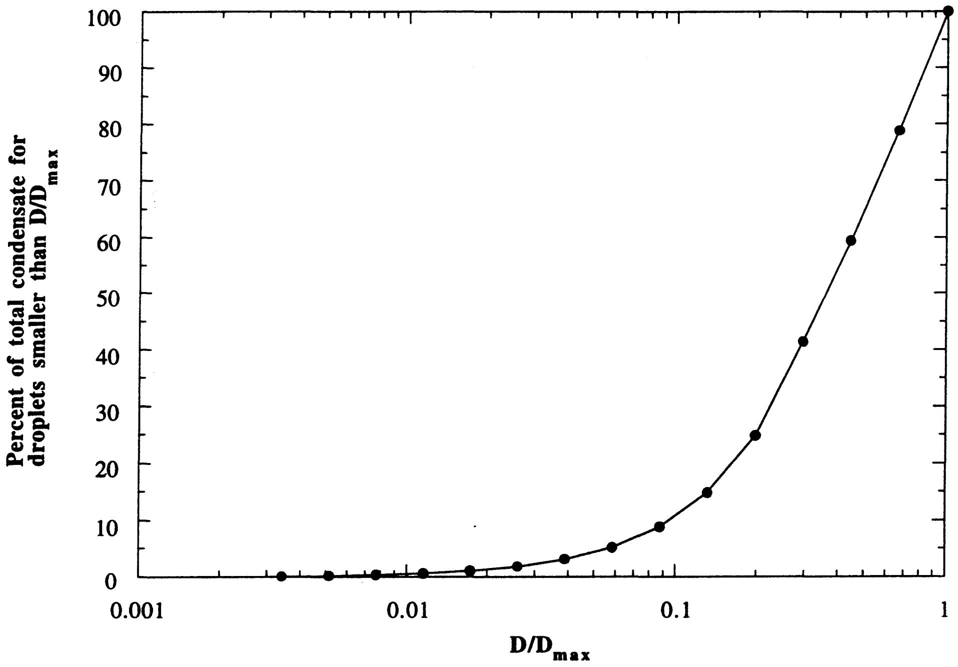

Figure 4.11 Percentage of total retained condensate for droplets smaller than D/D$_{max}$ predicted by model for wide fin spacing

# Chapter 5 - Conclusions and Recommendations

Condensate retention on plate-fin-tube heat exchangers has been investigated and several conclusions can be drawn from the real-time and steady-state experiments conducted during this study. In addition, the effects of condensation on air-side heat exchanger performance have been recorded and several conclusions may be inferred from these data. Modeling techniques for predicting the quantity of retained condensate based on the heat exchanger geometry, advancing and receding contact angles, and air-side Reynolds number have been presented. An initial model to predict condensate retention on plate-fin-tube heat exchangers with wide fin spacings has been developed. This model has been relatively successful in predicting condensate retention results for the heat exchanger of this study which met the assumptions of this model. Many questions regarding condensate retention effects on air-side heat exchanger behavior have yet to be answered and recommendations for future experimental work are presented in this chapter. In addition, refinements and extensions of the modeling techniques presented in Chapter 4 are discussed.

## 5.1 Condensate Retention Characteristics of Plate-Fin-Tube Heat Exchangers

- Condensate accumulates on a heat exchanger until reaching a steady state representing an equilibrium between condensate deposition and shedding.

  Real-time condensate retention measurements were recorded for heat exchangers with 4 and 8 fpi for air velocities between 2.1 and 5.6 m/s based on the minimum free flow area of the heat exchanger. The real-time measurements indicated that the quantity of retained condensate increased with time and asymptotically approached a steady value for which the rate of condensation on the heat transfer surface is balanced by condensate shedding.

- Heat exchangers with similar advancing and receding contact angles and having the same geometry retained the same quantity of condensate.

  Contact angle measurements indicated similar contact angles for the uncoated aluminum heat exchanger and the Mt. Holly Gold coated heat exchanger. Similar condensate retention results were observed for these heat exchangers.

- Surface wettability may increase during the first 100 hours of wet-dry cycling and surface wettability effects on condensate retention may depend on fin spacing.

  The surface wettability increased significantly during the first set of condensate retention experiments. This increase in surface wettability related to an increase in steady-state condensate retention for the heat exchanger with 8 fpi while relating to a decrease in retention for the heat exchanger with 4 fpi.

- The quantity of retained condensate divided by the total heat transfer area decreases with decreasing fin spacing for velocities between 1.5 and 8 m/s based on the heat exchanger minimum free flow area and for fin spacings from 4 to 12 fpi.

  A decrease in the steady-state value of condensate retention per heat transfer area was evident as the fin spacing decreased. This decrease is most likely a result of condensate on one fin surface interacting with condensate on the adjacent fin surface. For fin spacings less than 12 fpi, stable condensate bridges may form between adjacent fins leading to an increase in retained condensate per heat transfer area. Such bridging was not observed for the fin spacings and air velocities of this study.

- Air-flow forces did not significantly affect condensate retention for heat exchangers with 12 fpi or coated with hydrophilic coatings for velocities between 1.5 and 8 m/s based on the heat exchanger minimum free flow area.

  The steady-state values of retained condensate for heat exchangers with 12 fpi or coated with the hydrophilic coating were insensitive to the air-flow rate. At 12 fpi condensate may shed as bridges moving down adjacent fins. This shedding mechanism may be insensitive to air-flow forces. The hydrophilic coating will provide flatter droplets which may be less significantly influenced by air-flow forces.

- Differences were observed in the effects of air-flow rate on condensate retention which may be related to heat exchanger geometries, condensate removal mechanisms, or condensate retained as bridges in the wake regions at fin-tube junctions.

  The quantity of retained condensate decreased with increasing air-flow rates for the heat exchangers provided by Brazeway but increased with increasing air-flow rates for all of the heat exchangers provided by HeatCraft except those coated with the hydrophilic coating or having fin spacings of 12 fpi which were insensitive to air-flow rates.

## 5.2 Air-Side Performance Under Condensing Conditions

Experiments were conducted under dry conditions and repeated under condensing conditions to investigate the effects of condensation on air-side heat transfer and pressure drop. Several conclusions can be inferred from the data.

- Air-side sensible heat transfer performance under condensing conditions was dependent on the fin spacing.

  An enhanced sensible heat transfer performance was measured for an uncoated aluminum heat exchanger with 4 fpi under condensing conditions. A similar heat exchanger with 8 fpi did not show this enhancement. The results for the 8 fpi heat exchanger were inconclusive with air-side heat transfer coefficients under wet conditions sometimes higher and sometimes lower than the dry values.

- The effects of condensation on air-side heat exchanger pressure drop were dependent on the fin spacing and surface coatings.

  At 4 fpi, similar air-side friction factors were observed for wet and dry conditions. At 8 fpi the friction factor was observed to increase during the first set of experiments under wet conditions. This increase in friction factor decreased with increasing air-flow rates approaching the dry value. The quantity of retained condensate was also observed to decrease with increasing air-flow rates and may explain why similar friction factors for wet and dry conditions were observed at the highest air-flow rates. During the second set of experiments similar friction factors were observed at 8 fpi under wet and dry conditions. Increases in friction factors were observed at 10 and 12 fpi for wet conditions. The largest increases in friction factors were associated with the Mt. Holly Gold surface coating. Contact angle measurements indicated that the Mt. Holly Gold surface was the most hydrophobic and this may relate to the large friction factor increases.

## 5.3 Recommendations for Future Experimental Studies

In order to further validate and develop modeling techniques and identify the effects of condensation on the air-side performance of heat exchangers, additional condensate retention, heat transfer, and air-side pressure drop data should be acquired. Different heat exchanger geometries and orientations should be investigated. Fin spacings less than 12 fpi should be considered. Various hydrophobic and hydrophilic surface coatings should be included in future experiments covering a wider range of advancing and receding contact angles and contact angle hysteresis. For the present configuration with the air flow downward through the heat exchanger, the fin length and number of tube rows in the flow direction should be varied. Condensate retention varied along the length of the fin and this should be reflected in modeling techniques. In order to develop and validate a truly general model, condensate retention data for other flow configurations and fin geometries should be recorded. For the present heat exchanger orientation, air up-flow and air cross-flow should be considered. These air-flow configurations would generate air-flow forces in the opposite direction and perpendicular to gravitational forces respectively. Experiments conducted using different air-flow configurations may aid in identifying the contributions of the various forces acting on retained condensate. Many different fin geometries appear in air-conditioning and refrigeration applications (e.g. louver fin, wavy fin, spine fin) and the effects of the fin geometry on condensate retention and air-side performance under condensing conditions should be identified. New enhanced fin geometries such as fins with vortex generators should be considered in order to determine their effectiveness in condensing environments.

Measurements of advancing and receding contact angles for common coated and uncoated fin materials should continue and measurement techniques should be refined. Variations of these contact angles at different locations on the fin surface should be recorded to obtain accurate mean values. The contact angles of heat exchanger surfaces may vary over time with wet-dry cycling. These variations need to be identified so that changes in condensate retention and air-side performance of heat exchangers with time can be predicted. Differences in the measured advancing and receding contact angles existed when measuring these angles for hydrophilic surfaces using two different techniques. Future efforts should include developing techniques for accurately measuring the advancing and receding contact angles for hydrophilic surfaces.

### 5.4 Recommendations for Future Condensate Retention Modeling

The modeling techniques outlined in Chapter 4 and the initial model which has been developed may be used as a template for future modeling efforts. There are many refinements which can be made to these initial modeling techniques, and the techniques identify important information required for developing such models. Many higher order effects have not been included and are not well understood. Areas for future modeling efforts are presented below.

- Air-flow forces on retained condensate should be more accurately determined.

  Very crude assumptions have been made to include air-flow forces in initial condensate retention modeling efforts. In order to refine existing techniques, a more appropriate air velocity for calculating these forces should be determined. Air-flow forces have been calculated assuming a constant drag coefficient for droplets adhering to the heat transfer surfaces. This constant drag coefficient may not be appropriate and a more exact determination of the shear and pressure-drop forces acting on condensate droplets may be warranted. In addition, air-flow forces acting on other condensate geometries need to be determined.

- Several assumptions have been made regarding the shape of droplets adhering to the heat exchanger surfaces. These assumptions may be relaxed to more appropriately define the geometry.

  Contact lines for droplets adhering to a solid surface are not typically circular. Circular contact lines have been assumed in the initial analysis. An elliptical contact line may be more appropriate. Droplets have been approximated as truncated spheres meeting the solid surface at the average of the advancing and receding contact angles. The shapes of the droplet may be more accurately defined by solving the differential equation governing the shape of the liquid-vapor interface. In calculating the surface tension force, the contact angle was assumed to vary linearly around the circumference of the droplet. Different variations of the contact angle should be considered to identify the effects of this assumption on the calculated surface-tension force.

- Other condensate geometries which have been identified should be included in retention modeling.

  The initial model which has been developed considers droplets to be the only significant condensate geometry contributing to the total quantity of retained condensate for heat exchangers with wide fin spacings. The contributions of fillets retained at fin-tube junctions and pendant shape droplets retained at the fin tips have not been included. In developing modeling techniques for tighter fin spacings, bridges retained at fin tips and at fin-tube junctions should be considered.

- Variations in condensate retention along the length of the fin should be included in modeling.

  During retention experiments the amount of surface area covered by condensate decreased along the length of the fin. These variations should be included so that the model may be applied to heat exchangers with different fin lengths.

- Retention modeling should include different heat exchanger orientations and air-flow configurations.

  Modeling and experimental efforts have been for air down-flow and a heat exchanger oriented with fins in the vertical direction and horizontal tubes. Other heat exchanger orientations and air-flow configurations are required for a general model.

- Accurate size distributions of condensate geometries are required for accurate model development.

  Drop size distributions have been taken from studies of dropwise condensation on vertical surfaces. These studies were without air flow, and the presence of air flow may affect these distributions. In addition, higher order effects such as interactions between condensate on adjacent fin surfaces and between condensate on tubes and condensate on the fins may affect these distributions. Experimental measurements of these distributions are difficult to acquire and computer simulations may be warranted.

# Appendix A - Real-Time Condensate Retention Measurement

Real-time condensate retention measurements were acquired for heat exchangers 1 and 2. The measurement procedure requires further explanation and the details are provided. The experimental procedure involved zeroing and calibrating the load cell prior to each experiment. The load cell voltage was recorded over time as condensate accumulated on the heat transfer surfaces. This voltage included the weight of the retained condensate and the increase in air drag force due to the condensate. The increase in drag force was calculated based on differential pressures and subtracted from the measurement to determine the quantity of retained condensate.

## A.1 Zeroing the Load Cell

When performing real-time measurements of retained condensate, air was circulated in the closed-loop wind tunnel until the inlet air conditions reached the desired setpoints. The air-flow rate was set at the desired test condition. The load cell was zeroed at this air-flow rate and the air-flow rate was held fixed during the course of the experiment. The load cell was zeroed by adding or removing counterweight from the cable and pulley assembly (See Figure 2.2). The load cell was set so that it was loaded slightly when there was no condensate on the heat exchanger. This procedure ensured that there was always some load on the load cell and eliminated any play in the cable and pulley assembly. Care was taken to avoid overloading the load cell. The maximum load limit for the load cell was 400 grams while the entire inner assembly weighed several kilograms.

## A.2 Calibrating the Load Cell

The load cell was calibrated prior to each experiment. A calibration was required for each experiment because the frictional characteristics varied. For example, at higher air flow rates more counterweight was added to compensate for the increased drag force on the heat exchanger. The additional counterweight led to an increase in frictional forces in the weighing assembly. The load cell was calibrated by placing calibration weights on the leads to the heat exchanger which extended outside the test section. Two or three calibrations were performed prior to each experiment and agreement between calibrations was consistently within ±10% except at the loads less than 50 grams. The load cell calibration data were fit with a fifth order polynomial that was used to determined the load from the measured voltage. Typical calibration data are shown in Figure A.1.

Frictional forces prevented the load cell from returning to the original zero when loaded and unloaded. All calibrations and measurements were referenced to the starting voltage rather than a fixed zero to compensate for this offset. The voltages in Figure A.1 represent the change in voltage from the initial value.

### A.3 Measurement Hysteresis

Frictional forces in the weight measurement resulted in hysteresis as shown in Figure A.2. This hysteresis will result in different voltages for the same load depending on whether the heat exchanger is loaded or unloaded to reach the value. All calibrations were performed by adding calibration weights to the heat exchanger which reflects the loading direction as condensate accumulates on the heat exchanger. The load cell measurement is only valid as the load increases; therefore, all real-time retention plots in Chapter 2 extend only until the time at which the retained condensate began to decrease or reached a steady value.

### A.4 Drag Force Subtraction

The increased drag force across the heat exchanger due to the retained condensate was subtracted to determine the quantity of retained condensate. The differential pressure across the inner assembly which consisted of the heat exchanger and the contraction and diffusing sections was measured at approximately 40 second intervals as condensate accumulated on the heat exchanger. By performing a momentum balance on a control volume including the heat exchanger and the contraction and diffusion sections, the increase in drag force may be inferred from the differential pressure measurement. The momentum into and out of the control volume was assumed to be equal. The drag force increase on the control volume is then simply related to the increase in differential pressure multiplied by the area at the inlet and exit of the control volume. This area was assumed to be the test section cross sectional area at the location of the pressure taps. The increase in drag force corresponds to 6.31 grams for each Pascal increase in differential pressure.

The above derivation was validated by measuring the drag force increase as a function of the differential pressure increase. The load cell was zeroed and calibrated. The drag force was then increased by varying the air-flow rate. Figure A.3 shows the measured drag force increase versus the increase in differential pressure. The data were fit with a line and the slope of this line corresponds to 6.01 grams for each Pascal increase in differential pressure. This value is approximately 5% less than the calculated value based on the momentum balance and was used to determine the load associated with the drag force increase.

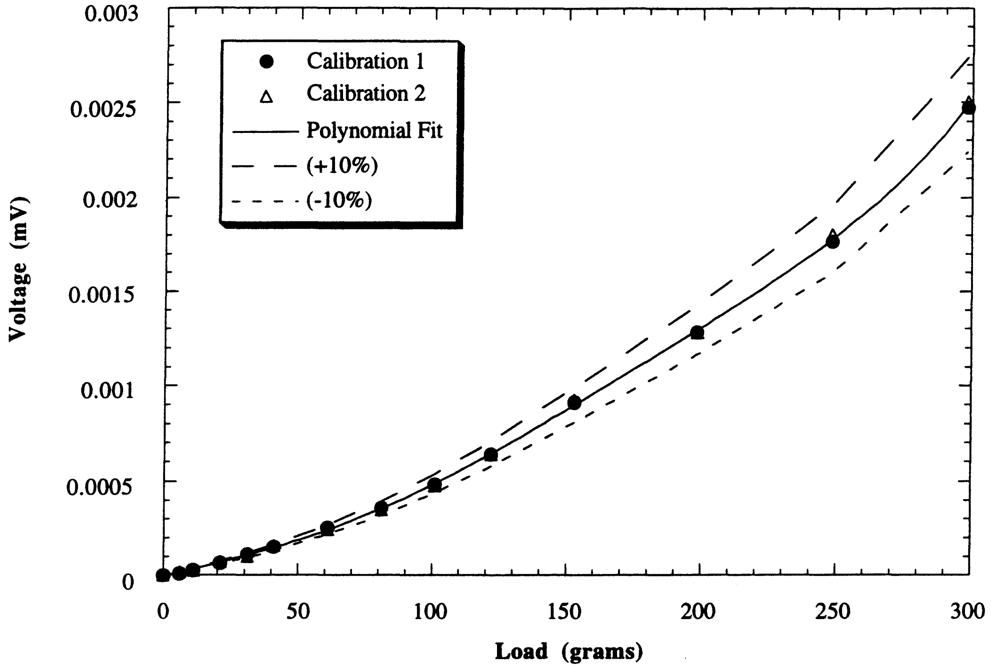

Figure A.1 Typical calibration data plotted with fifth order polynomial fit to data

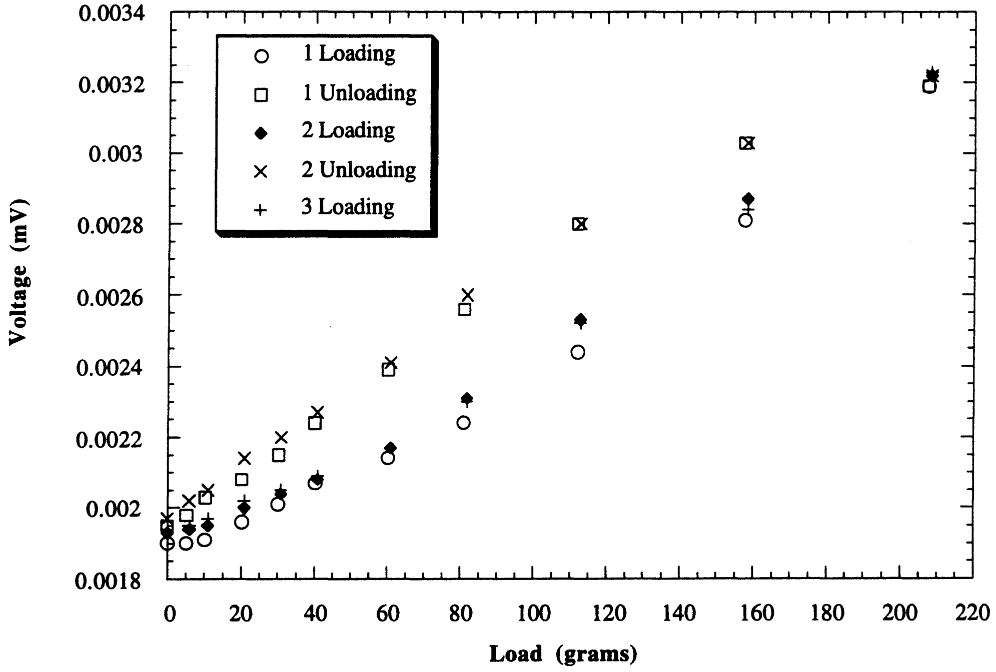

Figure A.2 Curves for loading and unloading showing measurement hysteresis

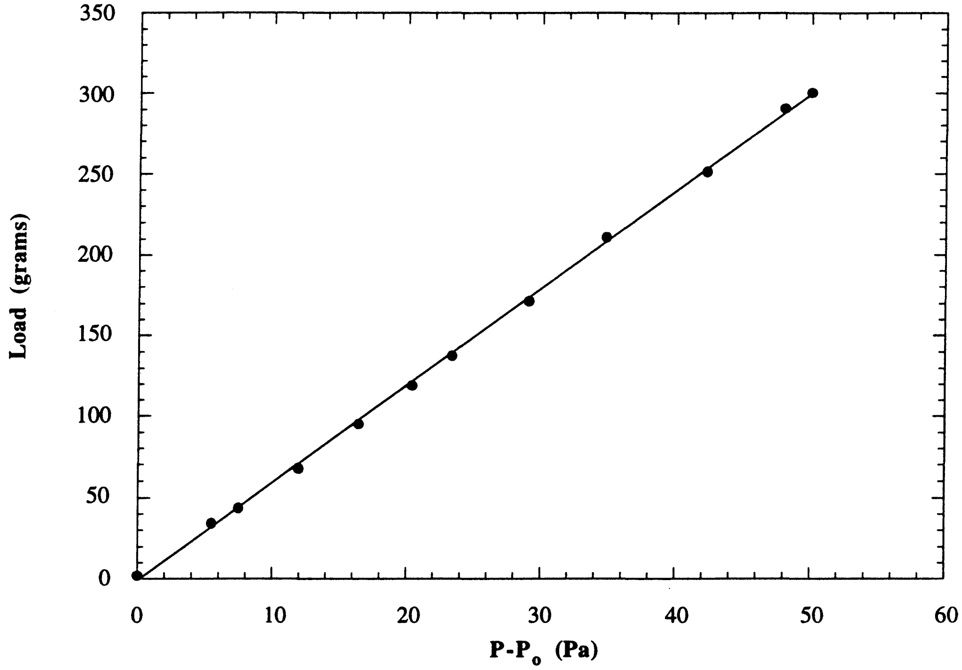

Figure A.3 Drag force increase corresponding to an increase in differential pressure across the inner assembly, determined by varying the air flow rate

# Appendix B - Data Reduction

## B.1 Derived Quantities

The basic calculated parameters are defined in Table B.1. Many of the calculations are straight forward. Further description of the calculations are provided as needed. Unless indicated otherwise, all air properties are evaluated assuming atmospheric pressure and using the average of the heat exchanger inlet and outlet temperatures and humidity ratios. Property evaluation functions are discussed in Sections B.5 and B.6.

## B.2 Air Mass Flow Rate Calculation

The air mass flow rate was calculated in accordance with ASME standard MFC-3M-1989 [26]. For a description of this calculation refer to the standard.

## B.3 Air Flow through Heat Exchanger

Only a fraction of the total mass flow rate of air passes through the heat exchanger. A fraction of the air bypasses the heat exchanger through the clearance between the inner assembly and the side walls of the test section as discussed in Section 2.2.1 D. This bypass was determined to be significant after conducting a portion of the experiments for heat exchangers 1 and 2. By varying the air-flow rate and comparing the velocity based on the total mass flow rate with the velocity measured at the inlet to the heat exchanger, Equations B.1 and B.2 were developed. These equations were used for heat exchangers 1 and 2 to determine the fraction of the total mass flow which passed through the heat exchanger. For heat exchangers 3 through 9, the velocity was measured directly.

<u>HX 1</u>

$$\chi = .9234 + \frac{9.059\text{x}10^{-2}}{V_{fr,calc}} - 1.126x10^{-2} \cdot V_{fr,calc} \tag{B.1}$$

<u>HX 2</u>

$$\chi = .8019 + \frac{0.1596}{V_{fr,calc}} + 1.313\text{x}10^{-3} \cdot V_{fr,calc} \tag{B.2}$$

## B.4 Coolant Mass Flow Rate

A volumetric flow meter was used to determine the coolant-side mass flow rate. The meter provided a 5 volt dc pulse with $3.092\text{x}10^5$ pulses per cubic meter of liquid. The meter was located in the return line; therefore, the outlet coolant temperature was used to calculate the coolant density used in the mass flow rate calculation (Equation B.3).

$$\dot{m}_c = 3.092\text{x}10^5 \rho_{c,2}\left(\frac{pulses}{s}\right) \tag{B.3}$$

## B.5 Coolant Property Evaluations

A mixture of ethylene glycol and water was used on the tube-side of the heat exchanger. The specific gravity of the mixture was 1.096. The specific gravity was measured using a hydrometer and used to determine the volume fraction of the glycol based on tables provided by the manufacturer. By interpolating on property tables provided by the manufacturer for the determined volume fraction of glycol, the property relations of Table B.2 were developed [43].

## B.6 Air Property Evaluations

Air property relations are presented in Table B.3. These property evaluations are for dry air. Moist air properties were determined using moist air relations from the ASHRAE Handbook of Fundamentals [44].

## B.7 Data Reduction Techniques for Wet Coils - Background

Two different approaches exist for determining wet coil air-side heat transfer coefficients. The first approach uses temperature and humidity ratio driving potentials for heat and mass transfer and makes no assumptions regarding the relationship between air-side heat and mass transfer coefficients. When applying this method, assumptions regarding the relationship between heat and mass transfer coefficients are made when the wet surface fin efficiency is determined. These assumptions are discussed in Appendix C. The second approach makes use of an enthalpy-based driving potential and the heat and mass transfer analogy.

### B.7.1 Temperature and Humidity Ratio Potential

The heat transfer rate for a differential area under condensing conditions is calculated using Equation B.4 for temperature and humidity ratio driving potentials. The latent heat transfer component is associated with the transfer of water vapor from the air and this vapor condensing on the surface. An error is introduced by using the humidity ratio as the driving potential because it expresses the mass fraction of water vapor per unit dry air rather than per unit moist air. This error is small for typical applications.

$$dq = dq_{sens} + dq_{lat} = h_{wet}dA(T_a - T_w) + h_D dA(W_a - W_{s,w})(i_{g,t} - i_{f,w}) \qquad \text{(B.4)}$$

where

$$i_{g,t} = \text{enthalpy of saturated water vapor at air dry-bulb temperature}$$

and

$$i_{f,w} = \text{enthalpy of saturated liquid water at temperature, } T_w$$

This approach was adopted by McQuiston [45], Wu and Bong [46], and Elmahdy and Biggs [47]. Additional assumptions are required in determining the fin efficiency as defined by Equation B.5. These assumptions are discussed in Appendix C.

$$\phi_{wet} = \frac{q_{fin}}{q_{\max}} = \frac{\int_{A_f}\left[h(T_a - T_w) + h_D(W_a - W_{s,w})(i_{g,t} - i_{f,w})\right]dA}{\left[h(T_a - T_b) + h_D(W_a - W_{s,b})(i_{g,t} - i_{f,b})\right]A} \qquad \text{(B.5)}$$

The surface effectiveness is defined by Equation B.6.

$$\eta_{wet} = \frac{\phi_{wet}A_f + A_p}{A_{tot}} \qquad \text{(B.6)}$$

Applying this surface effectiveness for a wet coil and assuming it applies to both heat and mass transfer, air-side heat and mass transfer coefficients may be determined from log mean temperature and humidity ratio differences [45].

$$q_{sens} = FUA_{tot}\Delta T_{lm} \qquad \text{(B.7)}$$

$$\frac{1}{UA_{tot}} = \frac{1}{\eta_{wet}h_{wet}A_{tot}} + \frac{\ln\left(D_{o,t}/D_{i,t}\right)}{2\pi k_t L_t} + \frac{1}{h_i A_i} \qquad \text{(B.8)}$$

$$q_{lat} = \eta_{wet}h_D A_{tot}F\Delta W_{lm}i_{fg} \qquad \text{(B.9)}$$

$$\Delta W_{lm} = \frac{\left(W_1 - W_{wall,1}\right) - \left(W_2 - W_{wall,2}\right)}{\ln\left[\frac{\left(W_1 - W_{wall,1}\right)}{\left(W_2 - W_{wall,2}\right)}\right]} \qquad \text{(B.10)}$$

A cross flow correction factor should be included is Equations B.7 and B.9. This correction factor is often taken to be unity without appropriate justification. Equation B.8 assumes that there is no fouling on the tube side or air-side of the heat exchanger. In addition, contact resistance between the fin and tube and conduction through the condensate is neglected. The log mean temperature difference is calculated assuming counter-flow conditions as described by Incropera and DeWitt [48]. The log mean humidity ratio difference is also calculated assuming counter-flow conditions. Mass transfer only occurs on the air-side heat transfer surfaces; therefore, the saturation condition at the tube wall is used in the log mean humidity ratio difference (Equation B.10). The superheat of the water vapor in the air is neglected in equation B.9.

### B.7.2 Enthalpy Potential

Simultaneous heat and mass transfer may be combined and defined in terms of an enthalpy driving potential. This technique was applied by Ware and Hacha [49] and presented by Threlkeld [50]. ARI Standard 410 [27] is based on the work of Ware and Hacha and also makes use of the enthalpy potential. In applying an enthalpy potential, the air-side mass transfer coefficient is assumed to be proportionally related to the air-side heat transfer coefficient. The heat and mass transfer coefficients may be assumed to be related by Equation B.11 based on the heat and mass transfer analogy.

$$h_{wet} = h_D Cp_{ma} Le^{2/3} \tag{B.11}$$

Equations B.11 and B.4 are combined as follows:

$$dq = \frac{h_{wet} dA}{Cp_{ma}} \left[ Cp_{ma}(T_a - T_w) + \frac{(W_a - W_{s,w})(i_{g,t} - i_{f,w})}{Le^{2/3}} \right] \tag{B.12}$$

Assuming ideal gas behavior for water vapor and air and taking 0°C as the reference temperature for air and water vapor enthalpies, the enthalpy of moist air may be expressed as follows:

$$i = Cp_{ma} T + i_{fg} W \tag{B.13}$$

Combining equations B.13 and B.12 provides the following:

$$dq = \frac{h_{wet} dA}{Cp_{ma}} \left[ (i_a - i_{s,w}) + \frac{\left(W_a - W_{s,w}\right)\left(i_{g,t} - i_{f,w} - i_{fg} Le^{2/3}\right)}{Le^{2/3}} \right] \tag{B.14}$$

The second term in the brackets is typically much smaller than the first term and is neglected providing an enthalpy based heat and mass transfer relation (Equation B.15). In addition to the error associated with neglecting this term, other errors arise from the assumed heat and mass transfer analogy and in assuming the air and water vapor to be an ideal gas. According to Kandlikar, [8] the total error is typically less than 3%.

$$dq = \frac{h_{wet} dA}{Cp_{ma}} \left(i_a - i_{s,w}\right) \tag{B.15}$$

Equation B.16 is used to determine the wet fin efficiency as defined by Ware and Hacha [49] and Threlkeld [50].

$$\phi_{wet} = \frac{q_{fin}}{q_{\max}} = \frac{i_a - i_{s,fin,mean}}{i_a - i_{s,fin,base}} \tag{B.16}$$

Threlkeld defines fictitious saturation enthalpies and uses a log mean enthalpy difference to determine the air-side heat transfer coefficient. Threlkeld's derivation includes the resistance associated with the water film; however, the water film thickness is typically unknown.

### B.7.3 Conclusion

The data reduction techniques applied to wet heat exchangers are rather straight forward, but several assumptions are made in the derivation. Many of these assumptions have not been outlined in this review and the derivations should be consulted when applying these techniques. The data reduction techniques applied to wet heat exchangers are complicated by the calculation of wet fin efficiencies. Wet fin efficiencies have been defined inappropriately and the application of different wet fin efficiencies makes comparisons between prior experimental results difficult. This topic is discussed in Appendix C. All of the data reduction techniques applied to wet coils assume the entire fin surface to be covered by a condensate film. While this simplifies the problem, this assumption may not be accurate. Visual observations made during this study indicated that condensate on typical heat transfer surfaces is not necessarily filmwise. Other complications arise from wet-dry partitioning for heat exchangers operating under partially dry conditions and the criteria used to determine whether the heat exchangers surfaces are wet or dry.

## B.8 Adopted Methods for the Calculation of Air-side Heat Transfer Coefficients (Wet and Dry)

Air-side heat transfer coefficients were determined based on ARI Standard 410 [27]. The data reduction procedures were modified slightly. These modifications included discretizing the heat exchanger in the air-flow direction. The discretization allowed data reduction techniques related to the particular heat exchanger geometries of this study to be evaluated. The approach applied to the analysis of the heat and mass transfer data was similar to the techniques applied by Mirth and Ramadhyani [11]. The data reduction techniques outlined in ARI Standard 410 [27] and applied in this study are similar to those developed by Ware and Hacha [49] and are based on an enthalpy potential for combined heat and mass transfer. The discretized approach which was applied may serve as a useful design tool especially for coils operating under partially-wet and partially-dry conditions. Wet-dry partitioning is determined by comparing the calculated surface temperature to the dewpoint of the air at each discretization. If local air-side heat transfer coefficients are known, the appropriate air-side heat transfer coefficient could be applied at each discretization to predict wet heat exchanger performance. For example, variations in air-side heat transfer coefficients with the tube row could be included. A detailed flow chart describing the data reduction procedure is illustrated in Figure B.1.

### B.8.1 Unique Data Reduction Issues

Several unique data reduction issues needed to be addressed because of the particular heat exchanger geometries of this study. The heat exchangers tested had tube side flow configurations that were half counter-flow and half parallel-flow. The circuiting is shown in Figure B.2. An appropriate $\varepsilon$ – NTU relation or cross-flow correction factor could not be found for this geometry. In order to determine the air-side heat transfer coefficients for this heat exchanger geometry, the heat exchanger was divided into two sections, an overall counter-flow section and an overall parallel-flow section. The heat exchangers should be divided along the adiabat between the two sections. The location of this adiabat was complicated by fin conduction between the tubes. On the air-side, the two portions of the heat exchanger are not isolated and mixing may occur between the two air streams. A discretized approach allowed these issues to be investigated.

### B.8.2 Data Reduction Procedure

The air-side heat transfer coefficient was determined by iteration. The coolant temperature out of the parallel-flow section is the coolant temperature into the counter-flow section. An air-side heat transfer coefficient was assumed and energy balances between the air-side and coolant side were used to determine the coolant temperatures out of the parallel-flow section and into the counter-flow section. The air-side heat transfer coefficient was updated and iteration continued until the midpoint coolant temperatures for the two sections were equal.

### B.8.3 Heat Transfer Rates

Air and coolant heat transfer rates were used to determine the air-side heat transfer coefficient and were compared as a redundant check. The heat transfer rates were calculated using Equations B.17 through B.19 based on measurements at the test section inlet and outlet.

$$q_{a,sens} = \dot{m}_{da} Cp_{ma} \left( T_{a,in} - T_{a,out} \right) \tag{B.17}$$

$$q_{a,tot} = \dot{m}_{da} \left( i_{a,in} - i_{a,out} \right) \tag{B.18}$$

$$q_c = \dot{m}_c Cp_c \left( T_{c,2} - T_{c,1} \right) \tag{B.19}$$

The air-side and coolant-side heat transfer rates were within 10.5% for the data used in determining air-side heat transfer coefficients except for the cases where small coolant-side temperature differentials lead to large uncertainties in the coolant-side heat transfer rates. High coolant-side flow rates were chosen to maximize the coolant-side heat transfer coefficient and minimize uncertainties in determining the air-side heat transfer coefficient. The data reduction techniques adopted assume the air-side and coolant-side heat transfer rates to be balanced. The coolant midpoint temperature out of the parallel-flow portion of the heat exchanger is matched with the coolant midpoint temperature into the counter-flow portion of the heat exchanger in order to determine the air-side heat transfer coefficient; therefore, the data reduction techniques rely on coolant-side heat transfer rates. Since coolant-side heat transfer rate uncertainties were large, especially at low heat transfer rates, the coolant temperatures used in the data reduction were adjusted, within the experimental uncertainty, to reflect the most appropriate value for the heat transfer rate. The air-side heat transfer rate was used at low heat transfer rates where coolant-side heat transfer uncertainties were large, and the average of the air-side and coolant-side heat transfer rates were used when the experimental uncertainties in these rates were similar.

### B.8.4 Heat Exchanger Partitioning

The heat exchanger was divided into two sections and discretized in the air-flow direction as shown in Figure B.3. One thousand discretizations were chosen based on convergence of the numerical scheme as shown in Figure B.4. The first discretization was divided into two segments based on the location of the adiabat between the first row of tubes. The temperature distribution along the fin between the first row of tubes was determined by solving the 1-D fin conduction equation (Equation B.20). The temperature of the fin at the boundaries was assumed to be the coolant temperature inside the tube. The effective air-side heat transfer coefficient is defined by Equation C.22. The effective air-side heat transfer coefficient was applied to account for the effects of the condensate on the location of the adiabat. By applying the effective air-side heat transfer coefficient, the temperature distribution along the fin was assumed to be linearly related to the saturation enthalpy at the surface temperature of the condensate layer.

$$\frac{d^2\theta}{d\zeta^2} - M^2\theta = 0 \qquad \text{(B.20)}$$

where

$$\theta = T_f - T_a \quad \zeta = \frac{\mathrm{x}}{\mathrm{S_t}} \quad \mathrm{M}^2 = \frac{S_t^{\,2} h_{eff}}{k_f y_f}$$

$$\theta_1 = T_{c,in,parallel} - T_{a,in} \quad \theta_2 = T_{c,out,counter} - T_{a,in}$$

The solution to this equation is as follows:

$$\theta(\zeta) = \frac{\theta_1 \sinh(M\zeta) - \theta_2 \sinh[M(1-\zeta)]}{\sinh(M)} \qquad \text{(B.21)}$$

By setting the derivative of the temperature distribution to zero, the location of the adiabat was determined.

$$0=\frac{d\theta}{d\zeta}=\frac{\theta_1 M\cosh(M\zeta^*)-\theta_2 M\cosh[M(1-\zeta^*)]}{\sinh(M)} \tag{B.22}$$

The last discretization was divided midway between the tubes. This adiabat is assumed because coolant temperatures are equal at this location and conduction effects between the tubes should be negligible. Between the first and last discretizations, the location of the adiabat was assumed to vary linearly and the sections were divided accordingly.

The effects of conduction were considered by running the data acquisition code applying the techniques outlined above and then setting $\zeta^* = 0.5$. Fin conduction resulted in changes in the determined air-side heat transfer coefficient of less than 0.6% even for the largest coolant-side temperature differentials, approximately 7 °C.

### B.8.5 Air-side Mixing and Air Flow Rate Division

The airstreams between the two parts of the heat exchanger are not isolated and mixing of the airstreams may occur between the parallel-flow and counter-flow portions of the heat exchanger. In addition, the mass flow rate of air in contact with the fin for both parts of the discretization must be determined at each step. Two cases were considered, (1) perfect air-side mixing and (2) no air-side mixing. By considering these two extremes, the effect of mixing on the calculated air-side heat transfer coefficient was determined.

The perfect mixing case was considered by calculating the inlet air properties for each discretization based on adiabatic mixing of the two air streams from the previous discretization. The air mass flow rate at each discretization was divided based on the area of the parallel and counter-flow portions of the discretization (Equations B.23 and B.24).

$$\dot{m}_{da,parallel}=\dot{m}_{da}\chi\frac{A_{parallel,step}}{A_{step}} \tag{B.23}$$

$$\dot{m}_{da,counter}=\dot{m}_{da}\chi\frac{A_{counter,step}}{A_{step}} \tag{B.24}$$

where

$$A_{step}=\frac{A_{tot}}{N_{steps}} \tag{B.25}$$

For the case with no mixing between the air streams, the inlet air conditions for the parallel-flow portion of each discretization were the outlet air properties for the parallel-flow portion of the previous discretization. Similarly, the inlet air conditions for each counter-flow portion of the discretization were the outlet air properties for the counter-flow portion of the previous discretization. For the no mixing condition, there is no way to appropriately divide the airstream. The airstream was assumed to be divided into two parts based on Equations B.26 and B.27. When not considering conduction between the tubes, $\zeta^*$ equals 0.5 and the airstream is divided equally between the two sections.

$$\dot{m}_{da,parallel} = \dot{m}_{da}\chi \frac{\frac{H_f}{2} + \left(\zeta^* - 0.5\right)\frac{S_t}{2}}{H_f} \tag{B.26}$$

$$\dot{m}_{da,counter} = \dot{m}_{da}\chi \frac{\frac{H_f}{2} - \left(\zeta^* - 0.5\right)\frac{S_t}{2}}{H_f} \tag{B.27}$$

Similar air-side heat transfer coefficients were determined by considering the two extremes, mixed and unmixed. The air-side heat transfer coefficients for these two cases differed by less than 0.8%.

### B.8.6 Data Reduction Equations

The data reduction equations are essentially the same as those provided in ARI Standard 410 with minor modifications.

The tube side heat transfer coefficient was determined by applying the correlation developed by Gnielinski [51] for turbulent flow. This correlation was chosen because it is applicable to the transitional Reynolds numbers of this study.

$$h_i = \frac{\left(\frac{f_c}{8}\right)\left(\mathrm{Re}_{D_c} - 1000\right)\mathrm{Pr}_c}{1 + 12.7\left(\frac{f_c}{8}\right)^{\frac{1}{2}}\left(\mathrm{Pr}_c^{\frac{2}{3}} - 1\right)} \cdot \frac{k_c}{D_{i,t}} \tag{B.28}$$

The friction factor is given by

$$f_c = \left(0.79 \ln \mathrm{Re}_{D_c} - 1.64\right)^{-2} \tag{B.29}$$

where

$$\mathrm{Re}_{D_c} = \frac{V_c D_{i,t} \rho_c}{\mu_c} \tag{B.30}$$

and

$$V_c = \frac{\dot{m}_c}{\rho_c A_i} \tag{B.31}$$

this yields the following internal resistance

$$R_{i,step} = \frac{1}{h_i A_{i,step}} \tag{B.32}$$

At each step, the surface is assumed to be wet. The total metal thermal resistance for a wet heat exchanger surface is the sum of the fin metal resistance and the tube wall resistance.

$$R_{m,step} = R_{t,step} + R_{f,step} \tag{B.33}$$

where

$$R_{t,step} = \frac{\ln\left(\frac{D_{o,t}}{D_{i,t}}\right)}{2\pi k_t L_{t,step}} \tag{B.34}$$

and applying the effective air-side heat transfer coefficient (Equation C.22)

$$R_{f,step} = \left(\frac{1-\eta_{step}}{\eta_{step}}\right)\left(\frac{1}{h_{eff}A_{step}}\right) \tag{B.35}$$

where, using the fin efficiency defined in Section C.3, the surface effectiveness is

$$\eta_{step} = \frac{\phi A_{f,step} + A_{p,step}}{A_{step}} \tag{B.36}$$

The mean surface temperature of the condensate layer must be determined iteratively at each discretization. This temperature was determined from the total heat transfer rate for the step and a resistance network between the air and coolant. This procedure is represented graphically as follows:

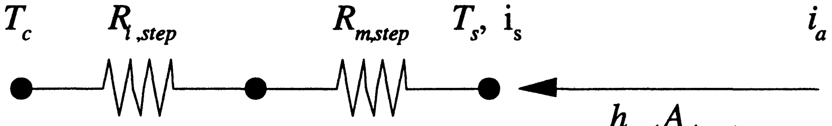

$$q_{step} = \frac{h_{wet}A_{step}}{Cp_{ma}}(i_a - i_s)$$

Based on the above network, the following ratio is defined

$$C_{step} = \frac{R_{m,step} + R_{i,step}}{Cp_{ma}\left(\frac{1}{h_{wet}A_{step}}\right)} \tag{B.37}$$

The coil surface temperature and enthalpy are related by Equation B.38. The surface enthalpy is the saturation enthalpy at the surface temperature. Applying Equation B.38 and the psychometric relationship between the surface enthalpy and the surface temperature, the surface temperature may be determined iteratively.

$$C_{step} = \frac{T_{s,new} - T_{c,old}}{i_{a,old} - i_{s,new}} \tag{B.38}$$

If the calculated surface temperature at the step is below the dewpoint of the air, the following equations are applied at the discretization assuming condensation to occur over the entire heat transfer surface.

$$q_{step} = \frac{h_{wet} A_{step}}{Cp_{ma}} \left( i_{a,old} - i_{s,new} \right) \tag{B.39}$$

The new air enthalpy is determined as follows

$$i_{a,new} = i_{a,old} - \frac{q_{step}}{\dot{m}_{da,step}} \tag{B.40}$$

The new coolant temperature is determined by applying an energy balance between the air-side and coolant side. The following equations are applied to the different sections of the heat exchanger.

For parallel flow:

$$T_{c,new} = \frac{q_{step}}{\dot{m}_c Cp_c} + T_{c,old} \tag{B.41}$$

For counter flow:

$$T_{c,new} = T_{c,old} - \frac{q_{step}}{\dot{m}_c Cp_c} \tag{B.42}$$

The new air temperature is calculated based on the log mean temperature difference between the air and surface temperatures.

$$T_{a,new} = T_{s,new} + (T_{a,old} - T_{s,new}) \exp\left( \frac{A_{step} h_{wet}}{\dot{m}_{da,step} Cp_{ma}} \right) \tag{B.43}$$

If the surface temperature calculated by Equation B.38 is above the dewpoint of the air, the following equations are applied at the discretization assuming the heat transfer surface to be dry.

$$q_{step} = \frac{T_{a,old} - T_{c,old}}{R_{i,step} + R_{a,step} + R_{t,step}} \tag{B.44}$$

where

$$R_{a,step} = \frac{1}{\eta_{step} h_{dry} A_{step}} \tag{B.45}$$

The new water temperature is calculated using Equation B.41 or B.42. The new air temperature is calculated as follows:

$$T_{a,new} = T_{a,old} - \frac{q_{step}}{\dot{m}_{da,step} Cp_{ma}} \tag{B.46}$$

Table B.1 Definitions of basic calculated parameters

| Parameter | Definition |
|---|---|
| $G$<br>(HX's 1 and 2) | $\frac{\dot{m}_{da}}{A_{\min}}\chi$ |
| $V_{max}$<br>(HX's 1 and 2) | $\frac{G}{\rho_a}$ |
| $G$<br>(HX's 3 thru 9) | $V_{\max}\rho_a$ |
| $V_{max}$<br>(HX's 3 thru 9) | $V_{meas}\left(\frac{A_{fr}}{A_{\min}}\right)\left(\frac{\rho_1}{\rho_a}\right)$ |
| $\chi$ | $\frac{V_{fr,meas}}{V_{fr,calc}}$ (Equations B.1 and B.2) |
| $V_{fr,calc}$ | $\frac{\dot{m}_{da}}{\rho_{a,1}A_{fr}}$ |
| $\mathrm{Re}_{D_{o,t}}$ | $\frac{GD_{o,t}}{\mu_a}$ |
| $\mathrm{Re}_{D_{coll}}$ | $\frac{GD_{coll}}{\mu_a}$ |
| $Nu_{D_{o,t}}$ | $\frac{hD_{o,t}}{k_a}$ |
| $j$ | $St\,\mathrm{Pr}^{2/3}$ |
| $St$ | $\frac{Nu}{\mathrm{Re}\,\mathrm{Pr}}=\frac{h}{GCp_{ma}}$ |
| $Pr_a$ | $\frac{Cp_{ma}\mu_a}{k_a}$ |
| $Pr_c$ | $\frac{Cp_c\mu_c}{k_c}$ |
| $Le$ | $\frac{Sc}{\mathrm{Pr}}=\frac{k_a}{\rho_a Cp_{ma}D_{AB}}$ |
| $f$ | $\frac{2\Delta P_{HX}\rho_a}{G^2}\left(\frac{A_{\min}}{A_{tot}}\right)-(1+\sigma^2)\left(\frac{\rho_{a,1}}{\rho_{a,2}}-1\right)\left(\frac{A_{\min}}{A_{tot}}\right)\left(\frac{\rho_a}{\rho_{a,1}}\right)$ |

Table B.2 Coolant property evaluations

| Property | Relation |
|---|---|
| $k_c\left(\frac{W}{m\cdot K}\right)$ | $\frac{0.1904+3.237\text{x}10^{-4}(T_c(°F))-1.829\text{x}10^{-6}(T_c(°F))^2+1.033x10^{-8}(T_c(°F))^3}{0.5778}$ |
| $\rho_c\left(\frac{kg}{m^3}\right)$ | $\frac{(69.271-1.732\text{x}10^{-2}T_c(°F))}{6.243\text{x}10^{-2}}$ |
| $\mu_c\left(\frac{N\cdot s}{m^2}\right)$ | $2.705\text{x}10^{-2}-8.048\text{x}10^{-4}(T_c(°F))+1.09\text{x}10^{-5}(T_c(°F))^2-5.593\text{x}10^{-8}(T_c(°F))^3$ |
| $Cp_c\left(\frac{kJ}{kg\cdot K}\right)$ | $\frac{0.7174+1.046\text{x}10^{-3}(T_c(°C))}{0.2389}$ |

Table B.3 Air property evaluations

| Property | Relation |
|---|---|
| $k_a\left(\frac{W}{m\cdot K}\right)$ | $2.406\text{x}10^{-2}+7.588\text{x}10^{-5}(T_a(°C))-4.997\text{x}10^{-8}(T_a(°C))^2$<br>$+2.10\text{x}10^{-10}(T_a(°C))^3-3.896\text{x}10^{-12}(T_a(°C))^4+3.384\text{x}10^{-14}(T_a(°C))^5$ |
| $\rho_a\left(\frac{kg}{m^3}\right)$ | $\frac{P(kPa)}{R_a\cdot T(K)}$ $\quad \mathrm{R_a}=0.287\left(\frac{kJ}{kg\cdot K}\right)$ |
| $\mu_a\left(\frac{N\cdot s}{m^2}\right)$ | $1.723\text{x}10^{-5}+4.910\text{x}10^{-8}(T_a(°C))-3.79\text{x}10^{-11}(T_a(°C))^2+1.86\text{x}10^{-13}(T_a(°C))^3$<br>$-4.025\text{x}10^{-15}(T_a(°C))^4+3.017\text{x}10^{-17}(T_a(°C))^5$ |

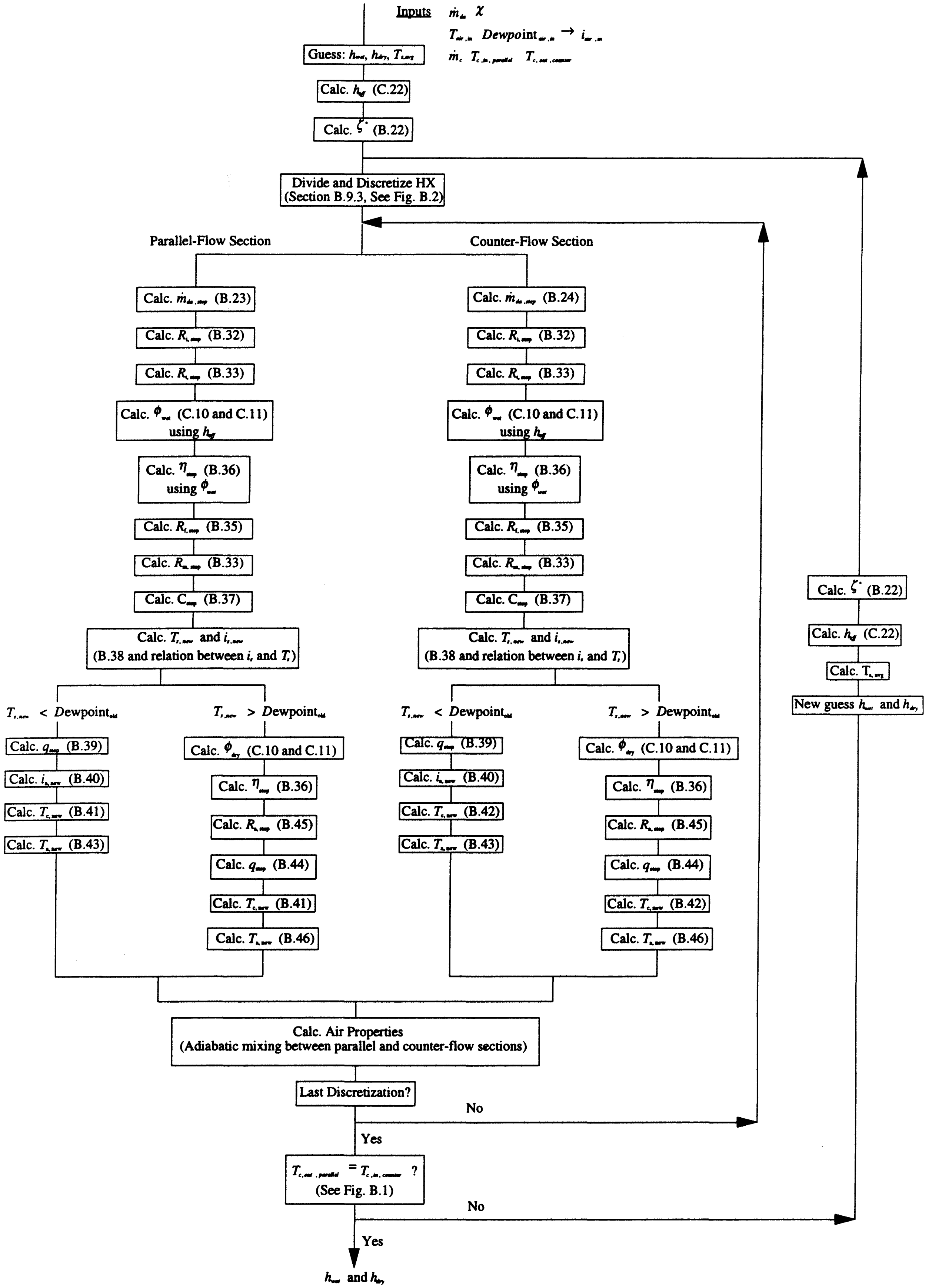

Figure B.1 Data reduction procedure flow chart

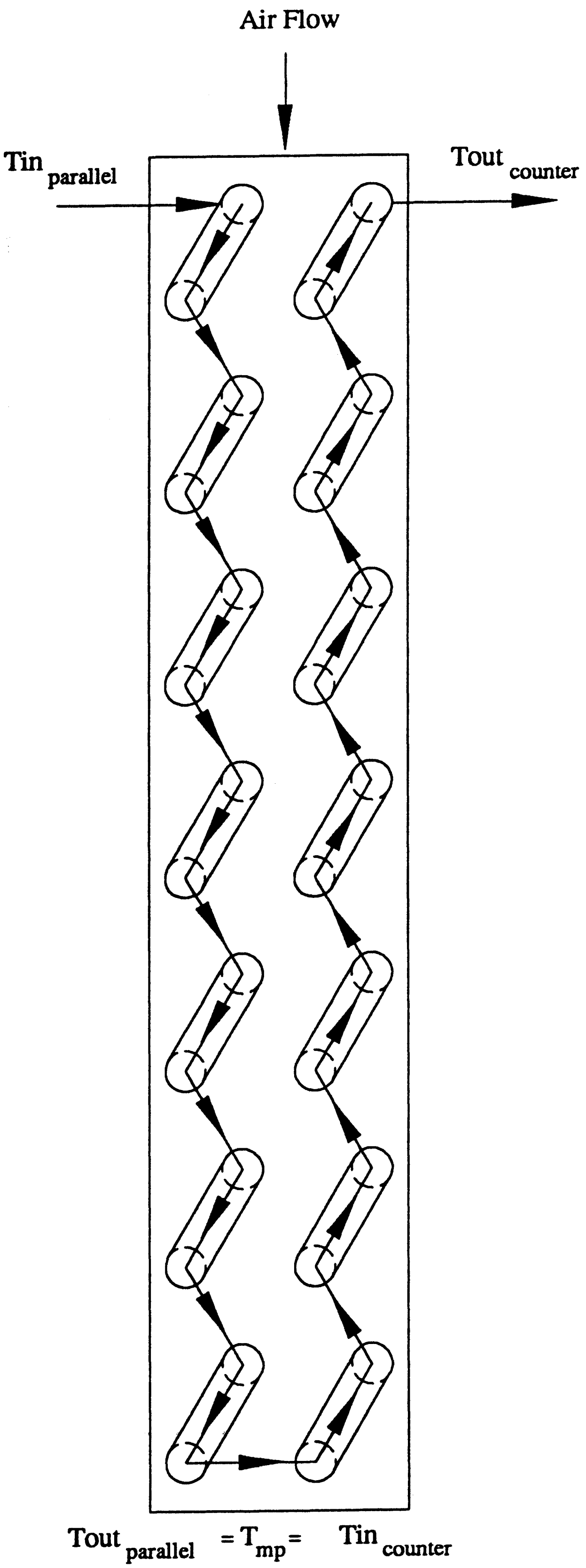

Figure B.2 Heat exchanger fluid circuiting schematic

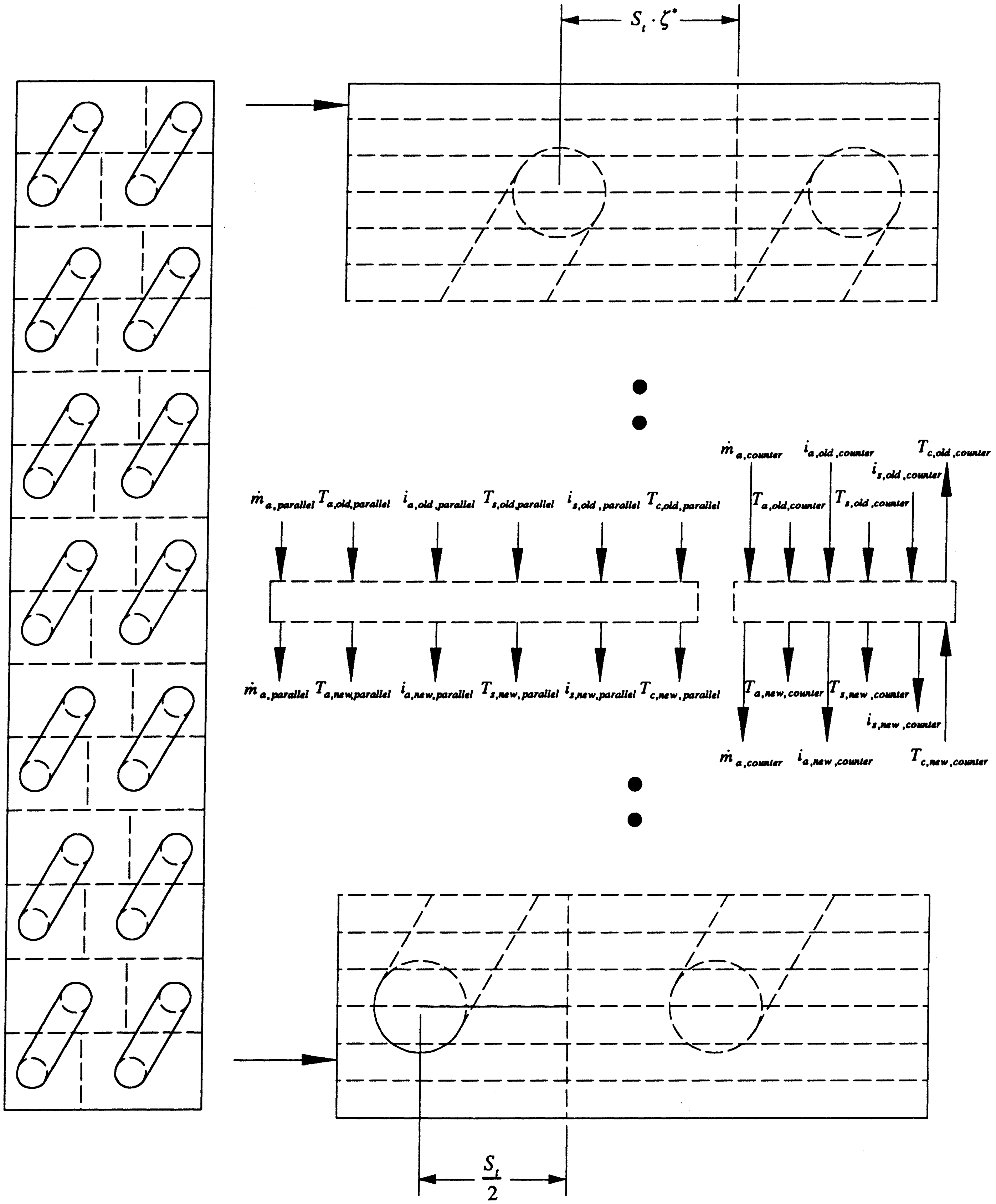

Figure B.3 Heat exchanger discretization schematic

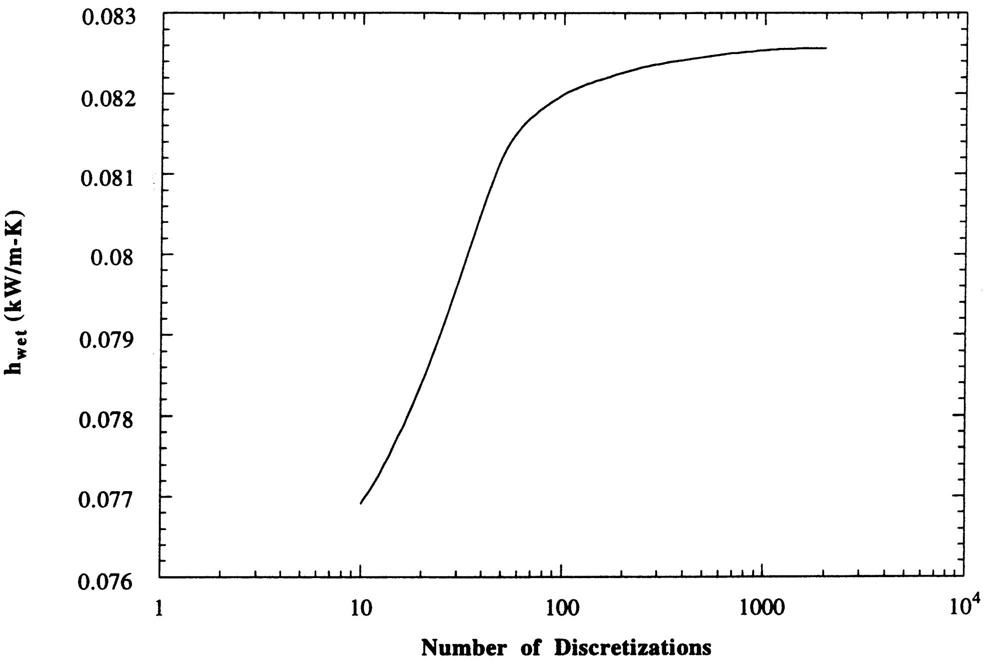

Figure B.4 Convergence of numerical scheme

# Appendix C - Fin Efficiency Calculation

## C.1 Dry Fin Efficiency Techniques

Various techniques for determining dry fin efficiencies for plate-fin-tube heat exchangers are presented in the literature. For plate-fin-tube heat exchangers the fin efficiency cannot be calculated directly, because the shape of the tube cross section is not the same as the shape of the fin. This difference makes it impossible to express the fin conduction equation in an orthogonal coordinate system which is necessary for an exact solution.

### C.1.1 ARI Equivalent Circular Area

ARI Standard 410 [27] recommends the use of an equivalent circular area for calculating the fin efficiency of plate fins. The standard fin solution for a circular fin is applied as presented by Gardner [52]. The equivalent inner and outer radii are defined as follows. The inner radius depends on the fin-tube connection.

Equivalent outer radius:

$$r_{o,equiv} = \left( \frac{H_f L_f}{\pi N_t} \right)^{\frac{1}{2}} \tag{C.1}$$

Equivalent inner radius:

- fins with collars touching adjacent fin

$$r_{i,equiv} = \frac{D_{o,t} + 2\delta}{2} \tag{C.2}$$

- fins with collars not touching adjacent fin

$$r_{i,equiv} = \frac{D_{o,t} + \delta}{2} \tag{C.3}$$

- fins without collars

$$r_{i,equiv} = \frac{D_{o,t}}{2} \tag{C.4}$$

### C.1.2 Schmidt Fin Efficiency Techniques

Schmidt [53] developed an approximate technique for determining the fin efficiency of a circular fin with a round tube by modifying the solution for the fin efficiency of a plane fin (Equation C.5).

$$\phi = \frac{\tanh(mH)}{mH} \tag{C.5}$$

where

$$m = \left( \frac{h_{dry}}{k_f y_f} \right)^{\frac{1}{2}} \tag{C.6}$$

Schmidt modified Equation C.5 as follows:

$$\phi = \frac{\tanh(mH')}{mH'} \tag{C.7}$$

where

$$H' = r_i \left( \frac{r_o}{r_i} - 1 \right) \left[ 1 + 0.35 \ln\left( \frac{r_o}{r_i} \right) \right] \tag{C.8}$$

Equation C.7 simplifies the exact solution for a circular fin with a round tube which involves Bessell functions. The exact solution can be easily implemented using a digital computer.

Schmidt [53] extended this derivation to include plate fins with tubes arranged in either an in-line or staggered arrangement. These two configurations are depicted in Figure C.1. The ratio of the inner and outer radii for plate fins was approximated as follows:

$$\left( \frac{r_o}{r_i} \right)_{equiv} = 1.28\Psi(\beta - 0.2)^{\frac{1}{2}} \tag{C.9}$$

where

$$\Psi = \frac{M}{r_i} \text{ and } \beta = \frac{L}{M}$$

note: L is chosen such that $L \geq M$

### C.1.3 Hong and Webb Equation

Hong and Webb [54] presented a modification to Equation C.7 developed by Schmidt. Equation C.7 was deemed unacceptable for $m(r_o\text{-}r_i) > 2.0$ and $r_o/r_i > 3$ where it over predicts the exact solution significantly. Equation C.7 can be extended over a wider range of $m(r_o\text{-}r_i)$ by applying the following modified equation presented by Hong and Webb.

$$\phi = \frac{\tanh(mH')\cos(0.1mH')}{mH'} \tag{C.10}$$

### C.1.4 Sector Method

The fin efficiency of rectangular or hexagonal fins of constant thickness attached to round tubes can be determined by applying the sector method which is depicted in Figure C.2.

The fin is approximated by circular segments constructed by dividing each fin edge into the same number of equal segments. The fin efficiency and area of each sector is calculated. The fin efficiency for each sector may be determined by the exact solution for a circular fin or by the approximate equations, Equation C.7 and Equation C.10. The fin efficiency is then determined by applying Equation C.11.

$$\phi = \frac{\sum_{j=1}^{N_s} \phi_j A_j}{\sum_{j=1}^{N_s} A_j} \tag{C.11}$$

## C.2 Wet Fin Efficiency Techniques

Various techniques exist for determining fin efficiencies for a wet fin. Most of these techniques assume that the entire fin in covered by a liquid film. As mentioned in Appendix B, the fin efficiency can be defined in terms of an enthalpy potential or by treating the heat and mass transfer potentials separately (Equations B.5 and B.16). The fin efficiency should be independent of the potentials used in the definition. In all cases, the fin efficiency is the rate of heat transfer to the fin divided by the maximum possible heat transfer rate to the fin. Most of the wet fin efficiency calculations appearing in the literature result in simple modifications of the dry fin efficiency equation. The largest discrepancy in the various techniques is that some are dependent on the humidity ratio of the air while others are independent of this parameter. Kandlikar [8] determined the fin efficiency of a wet fin to be independent of the humidity ratio of the air based on a mathematical analysis.

### C.2.1 McQuiston Wet Fin Efficiency

McQuiston defined a wet fin efficiency based on separate driving potentials for heat and mass transfer [45]. McQuiston assumed the heat and mass transfer coefficients to be related by the heat and mass transfer analogy and applied equation B.14 assuming the Lewis number to be equal to one. The fin conduction equation becomes:

$$\frac{d^2T}{dx^2} = \frac{hP_f}{k_f A_{c,f}} \left[ (T - T_a) + \frac{i_{fg}}{Cp_{ma}} (W - W_a) \right] \tag{C.12}$$

This equation can be solved if $(W - W_a)$ is simply related to $(T - T_a)$. McQuiston assumed the following relationship.

$$C_1 = \frac{W_{s,wall,1} - W_{a,1}}{T_{wall,1} - T_{a,1}} \qquad C_2 = \frac{W_{s,wall,2} - W_{a,2}}{T_{wall,2} - T_{a,2}} \tag{C.13}$$

and

$$C_{avg} = \frac{C_1 + C_2}{2} \tag{C.14}$$

The wet fin efficiency solution has the same form as the fin efficiency solution for a dry fin and the techniques of Section C.1 may be applied by replacing $m$ with $m_{eff}$ where $m_{eff}$ is defined as follows:

$$m_{eff} = m\left(1 + \frac{C_{avg} i_{fg}}{Cp_{ma}}\right)^{1/2} \tag{C.15}$$

### C.2.2 Elmahdy and Biggs Wet Fin Efficiency

Elmahdy and Biggs presented a numerical solution for the wet fin efficiency of a circular fin [47]. The heat and mass transfer coefficients were assumed to be related as follows:

$$h = h_D Cp_{ma} Le \tag{C.16}$$

In addition, a linear relationship was assumed between the fin surface temperature and the saturated air humidity ratio at the fin surface.

$$W_{s,r} = a + b_s T_r \tag{C.17}$$

The numerical results of Elmahdy and Biggs indicate that the wet fin efficiency decreases as the air relative humidity increases.

### C.2.3 Wu and Bong Wet Fin Efficiency

Wu and Bong also assumed a linear relationship between the fin surface temperature and the saturated air humidity ratio at the fin surface [46]. Heat and mass transfer coefficients were related by the Chilton-Colburn analogy.

$$h = h_D Cp_{ma} Le^{2/3} \tag{C.18}$$

Again, the fin efficiency solution has the same form as the fin efficiency solution for a dry fin. The techniques of Section C.1 may be applied by replacing $m$ with $m_{eff}$ where $m_{eff}$ is defined as follows:

$$m_{eff} = m(1 + b\xi)^{1/2} \tag{C.19}$$

where

$$\xi = \frac{i_{fg}}{Cp_{ma} Le^{2/3}}$$

and

$$b = \frac{W_{s,tip,f} - W_{s,b,f}}{T_{tip,f} - T_{b,f}}$$

Kandlikar [8] claimed that there was an error in Elmahdy and Biggs' numerical solution. The analytical results of Wu and Bong indicate that the wet fin efficiency is relatively independent of the air relative humidity. Except for the different forms of the heat and mass transfer analogy, Wu and Bong's and Elmahdy and Biggs' derivations are similar. The different effects of the air relative humidity on the wet fin efficiency support Kandlikar's claim that there is an error in Elmahdy and Bigg's solution.

### C.2.4 Threlkeld Wet Fin Efficiency

Threlkeld's analysis was based on an enthalpy driving potential as discussed in Section B.8.2. Threlkeld [50] showed the fin efficiency solution for a wet fin to be identical to the dry fin solution if an effective air-side heat transfer coefficient is applied. Threlkeld assumed that over a small temperature range the enthalpy of saturated air may be expressed as follows:

$$i_s = a_i + b_i T \tag{C.20}$$

Threlkeld defined the effective air-side heat transfer coefficient as follows:

$$h_{eff} = \frac{1}{Cp_{ma}/\left(b_{i,w,m} h_{wet}\right) + y_w/k_w} \tag{C.21}$$

where

$b_{i,w,m}$ = slope of saturated air temperature-enthalpy curve at mean water film temperature

The wet fin efficiency is then calculated by applying the techniques of section C.1 for dry fin efficiencies by replacing $h_{dry}$ with $h_{eff}$ in Equation C.6. The fin efficiency as defined by Threlkeld is relatively independent of the air relative humidity similar to the results of Wu and Bong. An advantage of Threlkeld's derivation is that it includes the effects of conduction through the water film if the average film thickness is known.

### C.2.5 ARI Standard 410 Wet Fin Efficiency

The wet fin efficiency and the data reduction techniques for combined heat and mass transfer as presented in ARI Standard 410 [27] are based on the work of Ware and Hacha [49]. An effective air-side heat transfer coefficient for wet conditions is used to determine the wet fin efficiency and the fin thermal resistance (Equation B.35). The effective air-side heat transfer coefficient is defined as follows:

$$h_{eff} = \frac{h_{wet} m''}{Cp_{ma}} \qquad \text{(C.22)}$$

where

$m''$ = slope of saturated air temperature-enthalpy curve at the coil surface temperature $\left.\frac{di_s}{dT}\right|_{T_s}$

The fin efficiency techniques of Section C.1 may be applied by replacing $h_{dry}$ with $h_{eff}$ in Equation C.6. The effective air-side heat transfer coefficient for wet conditions as defined by ARI Standard 410 is similar to the effective air-side heat transfer coefficient based on Threlkeld's analysis when the water film resistance is neglected. Once again, the wet fin efficiency is relatively independent of the relative humidity of the air.

## C.3 Data Reduction Procedure

At each discretization the fin efficiency was determined. The dry air-side heat transfer coefficient was used in Equation C.6 if the surface temperature at the discretization was determined by Equation B.38 to be greater than the dewpoint of the air. If the calculated surface temperature was less than the dewpoint of the air, the effective air-side heat transfer coefficient as defined by Equation C.22 was applied to determine the wet fin efficiency. The average surface temperature for the entire coil was used to calculate $m''$.

Fin efficiencies were calculated using various techniques to evaluate the effects of the fin efficiency calculation on the determined air-side heat transfer coefficient for both wet and dry fins. Wet fin efficiencies were determined by applying the effective air-side heat transfer coefficient as defined by ARI Standard 410 [27]. Figure C.3 illustrates the three different techniques which were compared. Wet air-side heat transfer coefficients determined by the three different fin efficiency techniques are shown in Figure C.4. The maximum variation in the calculated air-side heat transfer coefficient was approximately 10% for these three fin efficiency techniques.

In the final analysis, the sector method was adopted since this was considered to be the best technique for the calculation of the fin efficiency. Thirty-two sectors were used which was sufficient for convergence of the fin efficiency. The fin efficiencies of the sectors were calculated using Equation C.10. The fin was divided into 14 segments in the air flow direction with these divisions located midway between the tubes in this direction. The fin efficiency at each discretization was determined based on the segment of the fin associated with the discretization. The fin efficiency for this segment of the fin was applied at the discretization.

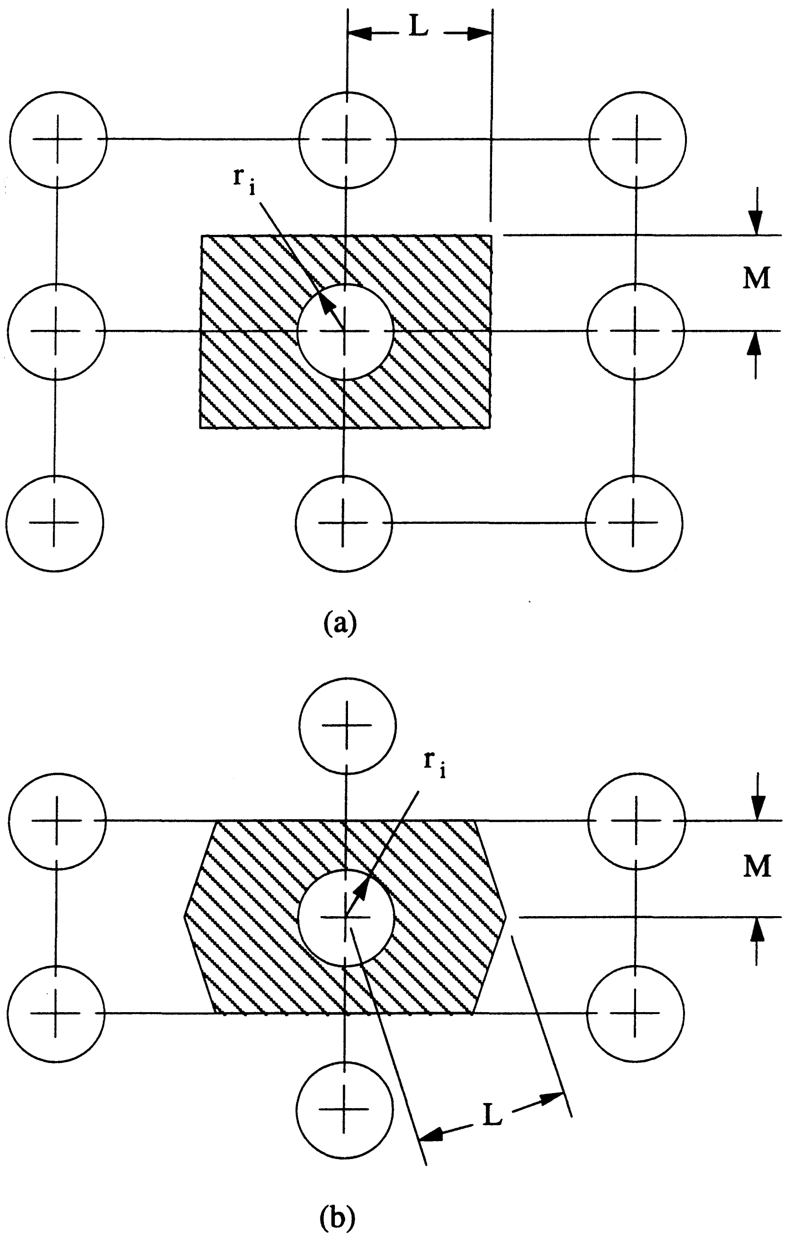

Figure C.1 Unit cells for Schmidt fin efficiency calculation
(a) in-line tubes (b) staggered tubes

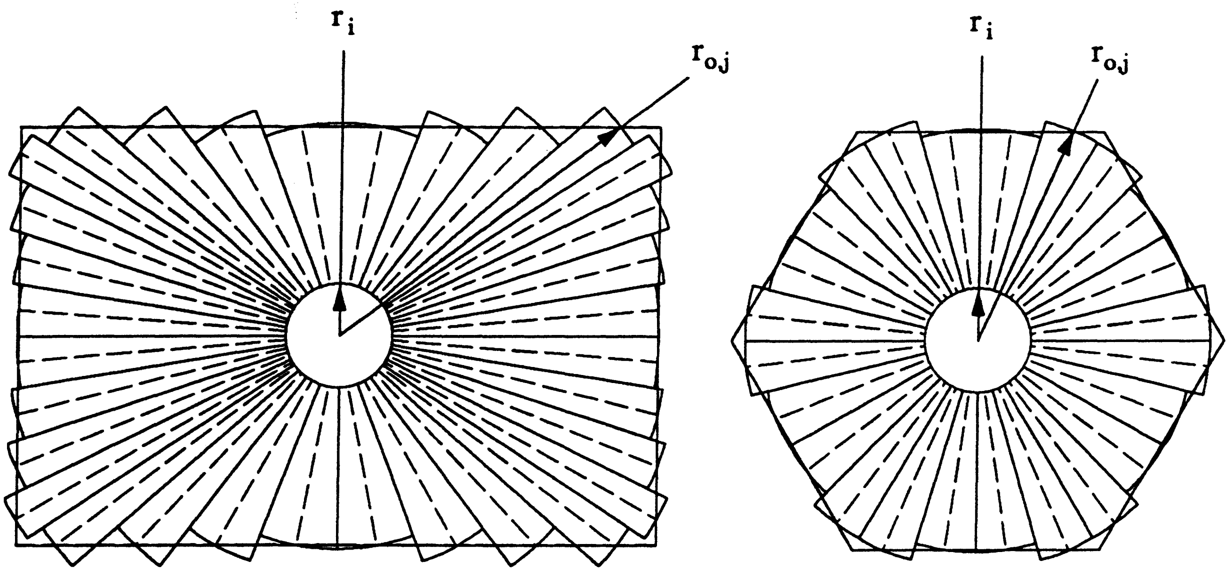

Figure C.2 Sector method for determining fin efficiencies for constant thickness fins (a) rectangular fin (b) hexagonal fin

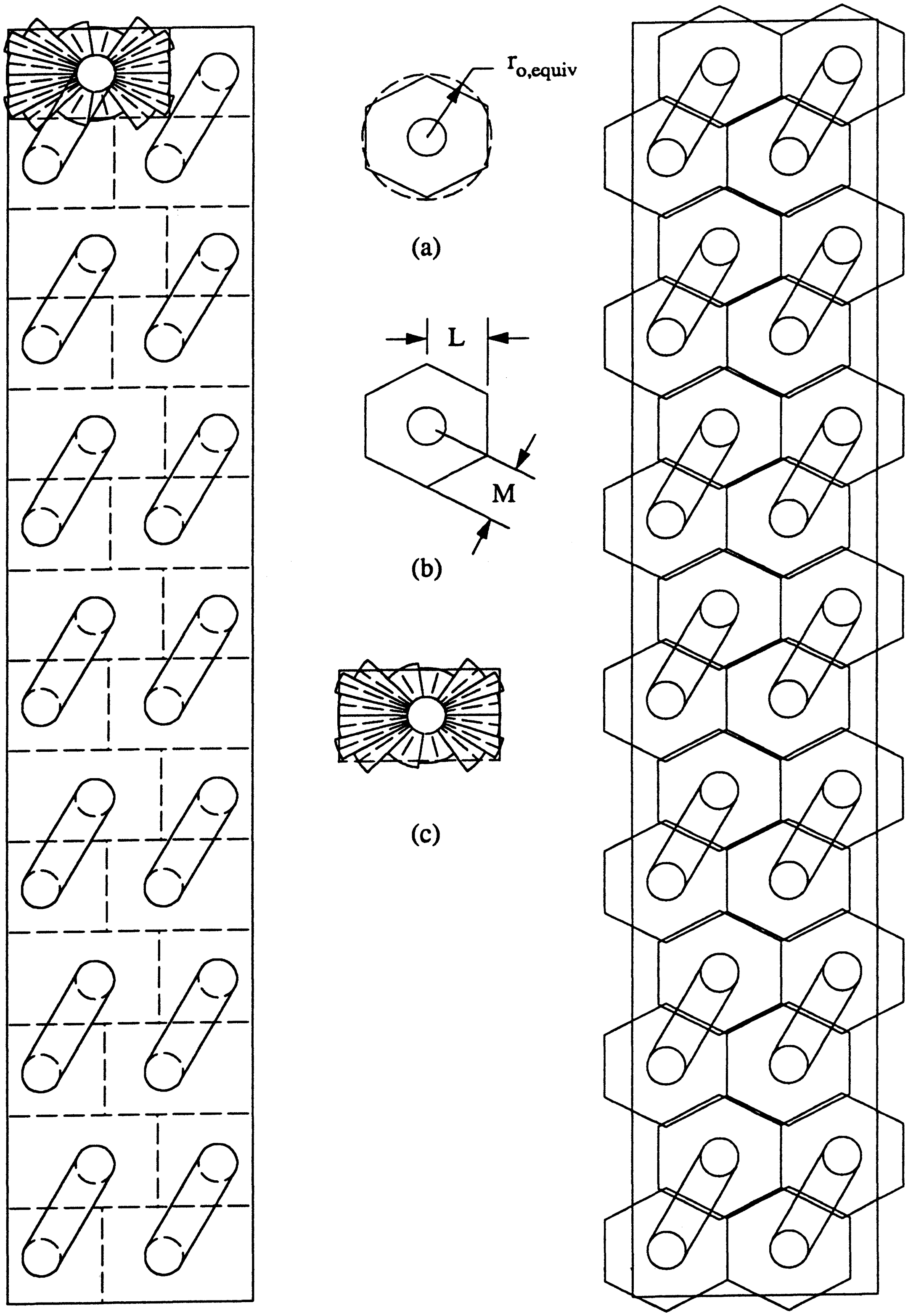

Figure C.3 Fin efficiency techniques applied to heat exchanger geometry of this study (a) ARI equivalent area (b) Schmidt hexagonal fin (c) Sector method with rectangular fin

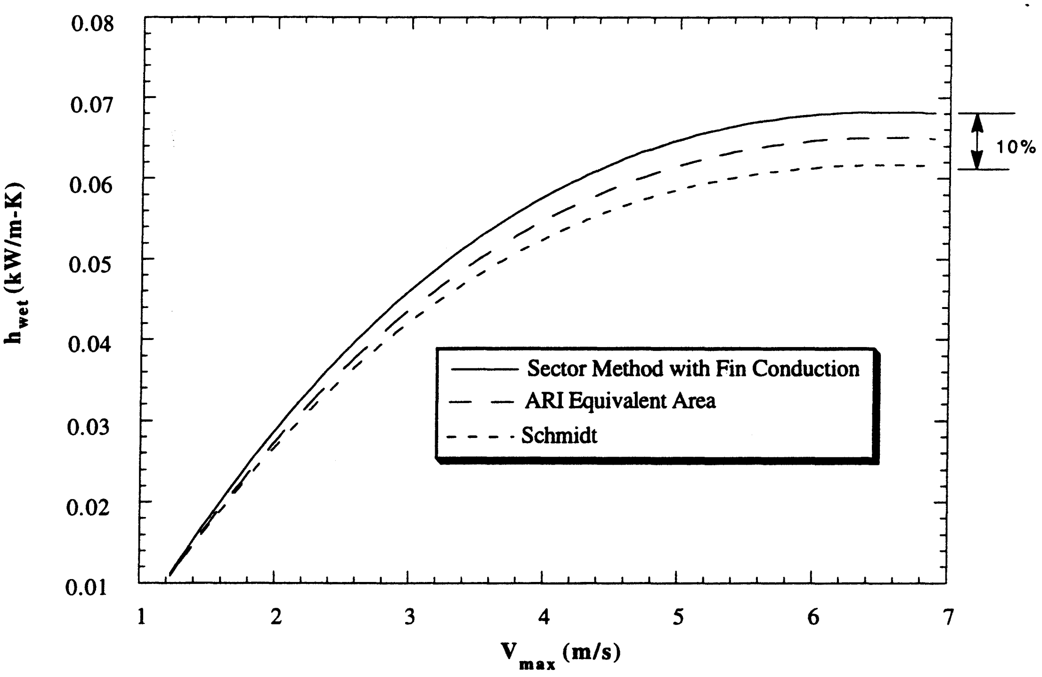

Figure C.4 Effects of fin efficiency techniques on wet air-side heat transfer coefficients, air assumed unmixed between counter-flow and parallel-flow halves of heat exchanger

# Appendix D - Uncertainty Analysis

Uncertainties in the reduced data are provided in this appendix. During the first set of experiments, including HX's 1 and 2, the mass flow rate measurement provided by the orifice was used to determine the velocity and mass velocity based on the minimum free flow area, $V_{max}$ and $G$. During the second set of experiments these values were calculated from the frontal velocity which was measured directly using an anemometer. Due to these differences, separate uncertainty analyses are provided for the two sets of experiments. Uncertainties were calculated applying the techniques outlined by Kline and McClintock [55] for single sample experiments. The uncertainties in the primary measurements were propagated to determine the uncertainties in the derived values using Equation D.1.

$$w_R = \left[ \left( \frac{\partial R}{\partial v_1} w_1 \right)^2 + \left( \frac{\partial R}{\partial v_2} w_2 \right)^2 + \dots + \left( \frac{\partial R}{\partial v_n} w_n \right)^2 \right]^{1/2} \qquad \text{(D.1)}$$

where

$w_n$ = uncertainty in variable $n$

$w_R$ = propagated uncertainty in result

$\frac{\partial R}{\partial v_n}$ = partial derivative of result with respect to variable $n$

## D.1 Uncertainties in Experimental Measurements

The uncertainties in the experimental measurements were discussed in Chapter 2 and are summarized in Table D.1. These uncertainties were propagated to provide the uncertainties in the experimental values calculated in the following sections.

## D.2 Uncertainty in Experimental Values for Heat Exchangers 1 and 2

### D.2.1 Air Mass Flow Rates

Air mass flow rates were determined by the following equation from ASME standard MFC-3M-1989 [26]

$$\dot{m}_{ma} = \frac{\pi}{4} d_{orif}{}^2 C \varepsilon \sqrt{\frac{2 \Delta P_{orif} \rho_a}{1-\beta^4}} \qquad \text{(D.2)}$$

where

$D_p$ = pipe diameter, $d_{orif}$ = orifice throat diameter

$C$ = discharge coefficient, $\varepsilon$ = Expansion factor, $\beta = \dfrac{D_p}{d_{orif}}$

The uncertainty in the discharge coefficient is 0.88% at the lowest mass flow rates with $\beta$ = 0.28 and 0.62% as the highest mass flow rates with $\beta$ = 0.62. The uncertainty in $d_{orif}$ and $\beta$ were approximately 0.5%. The uncertainty in $\rho_a$ was approximately 1%. Propagating these uncertainties and the uncertainty in differential pressure using Equation D.3 yields an uncertainty in mass flow rate of 1.3% for all air-flow rates.

$$\frac{w_{\dot{m}_{ma}}}{\dot{m}_{ma}} = \left[ \left( 2\frac{w_{d_{orif}}}{d_{orif}} \right)^2 + \left( \frac{1}{2}\frac{w_{\Delta P_{orif}}}{\Delta P_{orif}} \right)^2 + \left( \frac{w_C}{C} \right)^2 + \left( \frac{2\beta^3}{1-\beta^4} w_\beta \right)^2 + \left( \frac{w_{\rho_a}}{\rho_a} \right)^2 \right]^{1/2} \quad \text{(D.3)}$$

## D.2.2 Uncertainty in $\chi$

The fraction of air passing through the heat exchanger was calculated by comparing the frontal velocity based on the orifice plate mass flow rate calculation and the frontal velocity measured using a thermal anemometer as discussed in Section 2.2.1 D. The uncertainty in this fraction is given by Equation D.4. The uncertainty in the frontal area was calculated to be 3.5%, the uncertainty in the mass flow rate was 1.3% from the previous section. Applying Equation D.4 provides and uncertainty of 4% in $\chi$. Equations B.1 and B.2 were used to calculate $\chi$ and introduce an additional uncertainty of approximately 3% giving a total uncertainty of 5%.

$$\frac{w_\chi}{\chi} = \left[ \left( \frac{w_{V_{fr,meas}}}{V_{fr,meas}} \right)^2 + \left( \frac{w_{\rho_1}}{\rho_1} \right)^2 + \left( \frac{w_{A_{fr}}}{A_{fr}} \right)^2 + \left( \frac{w_{\dot{m}_{ma}}}{\dot{m}_{ma}} \right)^2 \right]^{1/2} \quad \text{(D.4)}$$

## D.2.3 Uncertainty in Mass Velocity

The mass velocity based on the minimum free flow area was calculated using the equation provided in Table B.1. The uncertainty in the mass velocity is calculated using equation D.5 to be 8%.

$$\frac{w_G}{G} = \left[ \left( \frac{w_{\dot{m}_{da}}}{\dot{m}_{da}} \right)^2 + \left( \frac{w_{A_{\min}}}{A_{\min}} \right)^2 + \left( \frac{w_\chi}{\chi} \right)^2 \right]^{1/2} \quad \text{(D.5)}$$

### D.2.4 Uncertainty in $V_{max}$

The velocity based on the minimum free flow area is determined by dividing the mass velocity by the mean air density. The uncertainty in the density is small compared to the uncertainty in the mass velocity; therefore, the uncertainty in $V_{max}$ is also 8%.

### D.2.5 Uncertainty in Air-Side Friction Factor

The friction factor is calculated using Equation 3.3. The second part of this equation accounts for momentum effects and is small compared to the first part. Neglecting the uncertainty in this correction, the uncertainty in the friction factor is calculated using Equation D.6. Applying uncertainties in $A_{min}$ of 6% and $A_{tot}$ of 1%, the uncertainty in the friction factor is determined to be approximately 17%.

$$\frac{w_f}{f}=\left[\left(\frac{w_{\Delta P_{HX}}}{\Delta P_{HX}}\right)^2+\left(2\frac{w_G}{G}\right)^2+\left(\frac{w_{\rho_a}}{\rho_a}\right)^2+\left(\frac{w_{A_{\min}}}{A_{\min}}\right)^2+\left(\frac{w_{A_{tot}}}{A_{tot}}\right)^2\right]^{1/2} \quad \text{(D.6)}$$

### D.2.6 Uncertainty in Air-Side Reynolds Number

Air-side Reynolds numbers were calculated based on the tube outer diameter (Equation 3.4). The uncertainty is determined applying Equation D.7. The uncertainty in the viscosity is approximately 1.2% and the uncertainty in the tube diameter is approximately 0.6%. These uncertainties are small compared to the uncertainty in the mass velocity giving and uncertainty in Reynolds number of approximately 8%.

$$\frac{w_{\mathrm{Re}_{D_{o,t}}}}{\mathrm{Re}_{D_{o,t}}}=\left[\left(\frac{w_G}{G}\right)^2+\left(\frac{w_{D_{o,t}}}{D_{o,t}}\right)^2+\left(\frac{w_{\mu_a}}{\mu_a}\right)^2\right]^{1/2} \quad \text{(D.7)}$$

### D.2.7 Uncertainty in Coolant Mass Flow Rate

The coolant mass flow rate is calculated using Equation B.3. The uncertainty in the volumetric mass flow rate of the meter is 0.5% as provided by the manufacturer. This uncertainty is coupled with the uncertainty in the number of pulses to determine the total uncertainty in mass flow rate. The uncertainty in the density of the coolant in negligible in comparison to the other uncertainties. The uncertainty as calculated by Equation D.8 is 0.7%.

$$\frac{w_{\dot{m}_c}}{\dot{m}_c}=\left[\left(\frac{w_{pulses}}{pulses}\right)^2+\left(\frac{w_{\rho_{c,2}}}{\rho_{c,2}}\right)^2+(.5\%)^2\right] \quad \text{(D.8)}$$

### D.2.8 Uncertainty in Air-Side Sensible Nusselt Numbers

Due to complex data reduction techniques, the uncertainty in the air-side heat transfer coefficient could not be determined analytically. The uncertainty was computed by numerically determining the derivatives in Equation D.9 by perturbing each of the variables by the uncertainty of the variable holding all others fixed. The effects of these uncertainties were then combined using Equation D.9. In some cases the effect of the perturbation of a particular variable depended on whether the value was increased or decreased. In these cases, the larger deviation in the air-side heat transfer coefficient was used in calculating the uncertainty. An uncertainty is introduced when applying Gnielinski's correlation to determine the coolant-side heat transfer coefficient. An uncertainty in $h_i$ of 10% was used based on the Handbook of Single-Phase Convective Heat Transfer [56]. The uncertainty in the air-side sensible heat transfer coefficients for dry conditions were 8.5% at the lowest Reynolds number and 15% at the highest Reynolds number. For wet conditions, the uncertainties were 6.5% at the lowest Reynolds number and 15% at the highest Reynolds number. The uncertainty in the air-side heat transfer coefficient is much larger than any other uncertainty in calculating the air-side Nusselt number based on the tube diameter (Table B.1) and these uncertainties are applicable to the Nusselt numbers.

$$\frac{w_h}{h}=\frac{1}{h}\left[\begin{array}{l}\left(\frac{\partial h}{\partial T_{a,in}}w_{T_{a,in}}\right)^2+\left(\frac{\partial h}{\partial T_{a,out}}w_{T_{a,out}}\right)^2+\left(\frac{\partial h}{\partial \dot{m}_{ma}}w_{\dot{m}_{ma}}\right)^2+\left(\frac{\partial h}{\partial \chi}w_{\chi}\right)^2+\\ \left(\frac{\partial h}{\partial Dpt_{in}}w_{Dpt_{in}}\right)^2+\left(\frac{\partial h}{\partial Dpt_{out}}w_{Dpt_{out}}\right)^2+\left(\frac{\partial h}{\partial A_f}w_{A_f}\right)^2+\left(\frac{\partial h}{\partial A_p}w_{A_p}\right)^2+\\ \left(\frac{\partial h}{\partial \dot{m}_c}w_{\dot{m}_c}\right)^2+\left(\frac{\partial h}{\partial T_{in,c}}w_{T_{in,c}}\right)^2+\left(\frac{\partial h}{\partial T_{out,c}}w_{T_{out,c}}\right)^2+\left(\frac{\partial h}{\partial h_i}w_{h_i}\right)^2\end{array}\right]^{1/2} \qquad \text{(D.9)}$$

### D.2.9 Uncertainty in Sensible j Factors

Sensible j factors were determined using Equation 3.1. The only significant contributions to the uncertainty are due to the calculation of the mass velocity based on the minimum free flow area, $G$, and the air-side heat transfer coefficient $h$. Combining these uncertainties using Equation D.10 yields an uncertainty in j for dry conditions of 11.5% at the lowest Reynolds number and 17% at the highest Reynolds number. For wet conditions the calculated uncertainty is 10% at the lowest Reynolds number and 17% at the highest

Reynolds number.

$$\frac{w_j}{j} = \left[ \left( \frac{w_h}{h} \right)^2 + \left( \frac{w_G}{G} \right)^2 + \left( \frac{w_{Cp_a}}{Cp_a} \right)^2 + \left( \frac{w_{\mathrm{Pr}}}{\mathrm{Pr}} \right)^2 \right]^{1/2} \tag{D.10}$$

## D.3 Uncertainty in Experimental Values for Heat Exchangers 3 through 9

### D.3.1 Uncertainty in $V_{max}$ and Air-Side Reynolds Number

The velocity based on the minimum free flow area of the heat exchanger was calculated using the equation in Table 3.1. The uncertainty in $V_{max}$ is approximately 10% when calculated using Equation D.11 with an uncertainty in $A_{fr}$ of 3.8% and $A_{min}$ of 9%.

$$\frac{w_{V_{\max}}}{V_{\max}} = \left[ \left( \frac{w_{V_{fr,meas}}}{V_{fr,meas}} \right)^2 + \left( \frac{w_{A_{fr}}}{A_{fr}} \right)^2 + \left( \frac{w_{A_{\min}}}{A_{\min}} \right)^2 + \left( \frac{w_{\rho_{a,1}}}{\rho_{a,1}} \right)^2 + \left( \frac{w_{\rho_a}}{\rho_a} \right)^2 \right]^{1/2} \tag{D.11}$$

The air-side Reynolds numbers for heat exchangers 3 through 9 were based on the tube collar diameter (Equation 3.5). The uncertainty in the collar diameter and the property evaluations are small compared to the uncertainty in $V_{max}$; therefore, the uncertainty in the air-side Reynolds number is also approximately 10%.

### D.3.2 Air-Side Friction Factor Uncertainty

Air-side friction factors were calculated using Equation 3.3. Equation D.6 is applied to determine the propagated uncertainty. The mass velocity based on the heat exchanger minimum free flow area is calculated according to Table B.1. Since the uncertainty in the air density is small compared to the uncertainty in $V_{max}$, the uncertainty in $G$ in also approximately 10%. Applying an uncertainty in $A_{min}$ of 9% and $A_{tot}$ of 0.75% provides and uncertainty in friction factor of approximately 21.5%.

## D.4 Uncertainty in Measured Condensate Retention

It is difficult to quantify the uncertainty in the condensate retention measurements. The uncertainties in the load cell and the electronic balance are negligible compared to other possible errors. The steady-state values from the real-time measurement and heat exchanger removal after prolonged exposure to condensing conditions typically agreed to within 15%. When removing the heat exchanger from the test section small amounts of condensate remain of the side walls of the test section. In addition a slight amount of evaporation occurs during the weighing process. These errors should be less than 5%. In all but one of the cases presented in Chapter 3, the steady-state value for the in test section measurement exceeds the value determined by removing the heat exchanger which may be indicative of these errors. When performing multiple calibrations of the load cell the voltages typically agreed to within 10% for loads above 50 grams. Subtracting the increase in drag force due to the retained condensate will introduce additional uncertainty. The force corresponding to an increase in differential pressure of 1 Pascal across the inner assembly was determined to be 6.01 grams. This value was determined using the load cell. Assuming the real-time measurement to have an uncertainty of 10% and combining this with an uncertainty of 10% in the increase in drag force and taking typical values of 220 grams of condensate and 300 grams of condensate plus the increase in drag force, the uncertainty may be calculated using Equation D.12 and is approximately 15%.

$$\frac{w_{F_{cond}}}{F_{cond}} = \left[ \left( \frac{w_{F_{tot}}}{F_{cond}} \right)^2 + \left( \frac{w_{F_{drag}}}{F_{cond}} \right)^2 \right]^{1/2} \qquad \text{(D.12)}$$

Table D.1 Uncertainty in Experimental Measurements

| Experimental Measurement | Uncertainty |
|---|---|
| $\Delta P_{HX}$ | ±0.0005 in water |
| $\Delta P_{orif}$ | ±0.0005 in water |
| $Dwpt_{in}$ | ±0.2°C |
| $Dwpt_{out}$ | ±0.2°C |
| $T_{a,in}$ | ±0.3°C |
| $T_{a,out}$ | ±0.5°C |
| **pulses** | ±2 |
| $T_{c,in}$ | ±0.3°C |
| $T_{c,out}$ | ±0.3°C |
| $V_{fr,meas}$ | ±1% |

# References

[1] Bettanini, E., 1970, "Simultaneous Heat and Mass Transfer on a Vertical Surface," *International Institute of Refrigeration Bulletin*, Vol. 70, pp. 309-317.

[2] Guillory, J. L., and McQuiston, F. C., 1973, "An Experimental Investigation of Air Dehumidification in a Parallel Plate Heat Exchanger," *ASHRAE Transactions*, Vol. 79, pp. 146-151.

[3] McQuiston, F. C., 1976, "Heat, Mass, and Momentum Transfer in a Parallel Plate Dehumidifying Exchanger," *ASHRAE Transactions*, Vol. 84, pp. 266-293.

[4] Tree, D., and Helmer, W., 1976, "Experimental Heat and Mass Transfer Data for Condensing Flow in a Parallel Plate Heat Exchanger," *ASHRAE Transactions*, Vol. 82, pp. 289-299.

[5] McQuiston, F. C., 1978a, "Heat, Mass, and Momentum Transfer Data for Five Plate-Fin-Tube Heat Transfer Surfaces," *ASHRAE Transactions*, Vol. 84, pp. 266-293.

[6] McQuiston, F. C., 1978b, "Correlation of Heat, Mass, and Momentum Transport Coefficients for Plate-Fin-Tube Heat Transfer Surfaces with Staggered Tubes," *ASHRAE Transactions*, Vol. 84, pp. 294-308.

[7] Eckels, P. W., and Rabas, T. J., 1987, "Dehumidification: On the Correlation of Wet and Dry Transport Processes in Plate Finned-Tube Heat Exchangers," *Journal of Heat Transfer*, Vol. 109, pp. 575-582.

[8] Kandlikar, S. G., 1990, "Thermal Design Theory for Compact Evaporators," in *Compact Heat Exchangers*, edited by Kraus, *et al.*, Hemisphere Publishing Corp., New York, NY, pp. 245-286.

[9] Hartnett, J. P. and Eckert, E. R. G., 1957, "Mass-Transfer Cooling in a Laminar Boundary Layer with Constant Fluid Properties," *Trans ASME*, Vol. 79, pp. 247-254.

[10] Wang, C. C., Hsieh, Y. C., and Lin, Y. T., 1997, "Performance of Plate Finned Tube Heat Exchangers Under Dehumidifying Conditions," *Journal of Heat Transfer*, Vol. 119, pp. 109-117.

[11] Mirth, D. R. and Ramadhyani, S., 1993, "Prediction of Cooling-Coil Performance under Condensing Conditions," *International Journal of Heat and Fluid Flow*, Vol. 14, pp. 391-400.

[12] Mirth, D. R. and Ramadhyani, S., 1994, "Correlations for Predicting the Air-Side Nusselt Numbers and Friction Factors in Chilled-Water Cooling Coils," *Experimental Heat Transfer*, Vol. 7, pp. 143-162.

[13] Fu, W. L., Wang, C. C., Chang, W. R., and Chang, C. T., 1995, "Effect of Anti-Corrosion Coating on the Thermal Characteristics of Louvered Finned Tube Heat Exchangers under Dehumidifying Conditions," *Advances in Enhanced Heat/Mass Transfer and Energy Efficiency*, HTD-Vol. 320/PID-Vol. 1, pp. 75-81.

[14] Hong, K., 1996, "Fundamental Characteristics of Dehumidifying Heat Exchangers with and without Wetting Coatings, " PhD thesis, Pennsylvania State University, PA.

[15] Bryan, W. L., 1961, "Heat and Mass Transfer in Dehumidifying Surface Coils," *ASHRAE Transactions*, Vol. 67, pp. 393-405.

[16] Bryan, W. L., 1962, "Heat and Mass Transfer in Dehumidifying Extended Surface Coils," *ASHRAE Transactions*, Vol. 68, pp. 237-247.

[17] Jacobi, A. M. and Goldschmidt, V. W., 1990, "Low Reynolds Number Heat and Mass Transfer Measurements of an Overall Counterflow, Baffled, Finned-Tube, Condensing Heat Exchanger," *Int. J. Heat Mass Transfer*, Vol. 33, pp. 755-765.

[18] Uv, E. H., and Sonju, O. K., 1992, "Heat Transfer Measurements of Circular Finned Tubes with and without Partial Condensation," *Institution of Chemical Engineers Symposium Series No. 129*, Vol. 1, pp. 295-302.

[19] Rudy, T. M. and Webb, R. L., 1981, "Condensate Retention on Horizontal Integral-Fin Tubing," *ASME Advances in Enhanced Heat Transfer*, Vol. HTD-18, pp. 35-41.

[20] Beatty, K. O. Jr. and Katz, D. L., 1948, "Condensation of Vapors on Outside of Finned Tubes," *Chemical Engineering Progress*, Vol. 44, pp. 55-70.

[21] Rudy, T. M. and Webb, R. L., 1985, "An Analytical Model to Predict Condensate Retention on Horizontal Integral-Fin Tubes," *Journal of Heat Transfer*, Vol. 107, pp. 361-368.

[22] Webb, R. L., Rudy, T. M., and Kedzierski, M. A., 1985, "Prediction of the Condensation Coefficient on Horizontal Integral-Fin Tubes," *Journal of Heat Transfer*, Vol. 107, pp. 369-376.

[23] Hu, X., Zhang, L., and Jacobi, A. M., 1994, "Surface Irregularity Effects of Droplets and Retained Condensate on Local Heat Transfer to Finned Tubes in Cross-Flow," *ASHRAE Transactions*, Vol. 100, pp. 375-381.

[24] Itoh, M., Kimura, H., Tanaka, T., and Musoh, M., 1982, "Development of Air-Cooling Heat Exchangers with Rough-Surface Louvered Fins," *ASHRAE Trans.*, Vol. 88, pp. 218-227.

[25] Morel, T., 1975, "Comprehensive Design of Axisymmetric Wind Tunnel Contractions," *Journal of Fluids Engineering*, Vol. pp. 225-233.

[26] ASME, 1989, *Measurement of Fluid Flow in Pipes using Orifice, Nozzle, and Venturi*, MFC-3M-1989.

[27] ARI, 1981, *Standard for Forced-Circulation Air-Cooling and Air-Heating Coils*, ARI-410.

[28] Rich, D. G., 1973, "The Effect of Fin Spacing on the Heat Transfer and Friction Performance of Multi-Row, Smooth Plate Fin-and-Tube Heat Exchangers," *ASHRAE Trans.*, Vol. 79, pp. 137-145.

[29] Chappuis, J., 1982, "Contact Angles," in *Multiphase Science and Technology*, edited by Hewitt, *et al.*, Vol. 1, Hemisphere Publishing Corporation, Washington, D.C., pp. 387-505.

[30] Carey, V. P., 1992, *Liquid-Vapor Phase-Change Phenomena*, Series in Chemical and Mechanical Engineering, edited by Hewitt, *et al.*, Hemisphere Publishing Corporation, Washington, D.C..

[31] Johnson, R. E. Jr. and Dettre, R. H., 1969, "Wettability and Contact Angles," in *Surface and Colloid Science*, edited by Matijevic, Vol. 2, Wiley-Interscience, New York, NY, pp. 85-153.

[32] Jasper, J. J., 1972, "The Surface Tension of Pure Liquid Compounds," *J. Phys. Chem. Ref. Data*, Vol. 1, pp. 841-1010.

[33] Furmidge, C. G. L., 1962, "Studies at Phase Interfaces 1. The Sliding of Liquid Drops on Solid Surfaces and a Theory for Spray Retention," *Journal of Colloid Science*, Vol. 17, pp. 309-324.

[34] Dussan V., E. B. and Chow, R. T-P., 1983, "On the Ability of Drops or Bubbles to Stick to Non-Horizontal Surfaces of Solids," *J. Fluid Mech.*, Vol. 137, pp. 1-29.

[35] Dussan V., E. B., 1985, "On the Ability of Drops or Bubbles to Stick to Non-Horizontal Surfaces of Solids. Part 2. Small Drops or Bubbles Having Contact Angles of Arbitrary Size," *J. Fluid Mech.*, Vol. 151, pp. 1-20.

[36] Milinazzo, F. and Shinbrot, M., 1988, "A Numerical Study of a Drop on a Vertical Wall," *Journal of Colloid and Interface Science*, Vol. 121, pp. 254-264.

[37] Dussan V., E. B., 1987, "On the Ability of Drops to Stick to Surfaces of Solids. Part 3. The Influences of the Motion of the Surrounding Fluid on Dislodging Drops," *J. Fluid Mech.*, Vol. 174, pp. 381-397.

[38] Durbin, P. A., 1988a, "Free-Streamline Analysis of Deformation and Dislodging by Wind Force of Drops on a Surface," *Phys. Fluids*, Vol. 31, pp. 43-48.

[39] Durbin, P. A., 1988b, "On the Wind Force Needed to Dislodge a Drop Adhered to a Surface," *J. Fluid Mech.*, Vol. 196, pp. 205-222.

[40] Al-Hayes, R. A. M. and Winterton, R. H. S., 1981, "Bubble Diameter on Detachment in Flowing Liquids," *Int. J. Heat Mass Transfer*, Vol. 24, pp. 223-230.

[41] Sugawara, S. and Michiyoshi, I., 1965, "Dropwise Condensation," *Mem. Fac. Engng, Kyoto Univ.*, Vol. 18, pp. 84-111.

[42] Graham, Clark, 1969, "The Limiting Heat Transfer Mechanisms of Dropwise Condensation, " PhD thesis, Massachusetts Institute of Technology, MA.

[43] Davis, M., 1996, "Evaporator Calorimeter: The Study of Overall Heat Transfer Performance, " M.S. thesis, University of Illinois at Urbana - Champaign, IL.

[44] ASHRAE, 1985, *ASHRAE Handbook 1985 Fundamentals*, Atlanta, GA.

[45] McQuiston, F. C., 1975, "Fin Efficiency with Combined Heat and Mass Transfer," *ASHRAE Transactions*, Vol. 81, pp. 350-355.

[46] Wu, G., and Bong, T. Y., 1994, "Overall Efficiency of a Straight Fin With Combined Heat and Mass Transfer," *ASHRAE Transactions*, Vol. 100, pp. 367-374.

[47] Elmahdy, A. H. and Biggs, R. C., 1983, "Efficiency of Extended Surfaces with Simultaneous Heat and Mass Transfer," *ASHRAE Transactions*, Vol. 89, pp. 135-143.

[48] Incropera, F. P. and DeWitt, D. P., 1990, *Fundamentals of Heat and Mass Transfer*, 3rd ed., John Wiley & Sons, New York, NY.

[49] Ware, C. D. and Hacha, T. H., 1960, "Heat Transfer From Humid Air to Fin and Tube Extended Surface Cooling Coils," *ASME Paper No. 60-HT-17.*

[50] Threlkeld, J. L., 1970, *Thermal Environmental Engineering*, Prentice-Hall, New York, NY.

[51] Gnielinski, V., 1976, "New Equations for Heat and Mass Transfer in Turbulent Pipe and Channel Flow," *Int. Chem. Eng.*, Vol. 16, pp. 359-368.

[52] Gardner, Karl A., 1945, "Efficiency of Extended Surface," *ASME Transactions*, Vol. 67, pp. 621-631.

[53] Schmidt, T. E., 1949, "Heat Transfer Calculations for Extended Surfaces," *Refrigerating Engineering*, Vol. 57, pp. 351-357.

[54] Hong, T. K., and Webb, R. L., 1996, "Calculation of Fin Efficiency for Wet and Dry Fins," *International Journal of HVAC & R Research*, Vol. 2, pp. 27-41.

[55] Kline, S. J. and McClintock, F. A., 1953, "Describing Experimental Uncertainties in Single Sample Experiments," *Mechanical Engineering*, Vol. 75, pp. 3-8.

[56] Kakaç, S., Shaw, R. K., and Aung, W., 1987, *Handbook of Single-Phase Convective Heat Transfer*, John Wiley & Sons, New York, NY.